

**Grain boundary characterization of electroceramics:
Acceptor-doped BaZrO₃, an intermediate temperature
proton conductor**

Von der Fakultät Chemie der Universität Stuttgart
zur Erlangung der Würde eines Doktors der
Naturwissenschaften (Dr. rer. nat.) genehmigte Abhandlung

Vorgelegt von
Mona Shirpour
aus Teheran, Iran

Hauptberichter:	Prof. Dr. J. Maier
Mitberichter:	Prof. Dr. J. Bill
Prüfungsvorsitzender:	Prof. Dr. E. J. Mittemeijer
Tag der Einreichung:	14.01.2011
Tag der mündlichen Prüfung:	04.03.2011

Max-Planck-Institut für Festkörperforschung

Stuttgart

2011

Contents

Contents.....	3
Zusammenfassung.....	5
Abstract.....	9
Introduction and Motivation.....	13
1.1 Solid Oxide Fuel Cells and proton conducting oxides.....	13
1.2 Protonic defects and proton mobility.....	15
1.3 Acceptor doped BaZrO ₃ , its potentials and limitations.....	18
1.4 Blocking character of grain boundaries.....	20
1.4.1 Secondary phase.....	21
1.4.2 Grain boundary structure.....	21
1.4.3 Space charge layers.....	21
1.4.4 Segregation.....	23
1.4.5 Specific features for BaZrO ₃	24
Experimental.....	25
1.5 Sample preparation.....	25
1.5.1 Single phase powders.....	25
1.5.2 Polycrystalline samples.....	26
1.5.3 Large grained sample.....	26
1.5.4 Thin films.....	27
1.6 Sample characterization.....	27
1.6.1 X-ray diffraction.....	27
1.6.2 Scanning electron microscopy.....	28
1.6.3 ICP-OES.....	28
1.6.4 TG-hydration isobars.....	28
1.6.5 XPS.....	29
1.6.6 BET.....	29
1.6.7 Density by geometry method.....	30

1.6.8	Raman spectroscopy	30
1.6.9	Transmission electron microscopy	30
1.6.10	AC-impedance spectroscopy	31
Results and discussion.....		37
1.7	Structure and chemical composition of GB and its effect on σ_{GB}	37
1.7.1	Sample characterization (polycrystalline)	37
1.7.2	Grain boundary hydration behavior	44
1.7.3	Secondary/amorphous phase at GB.....	46
1.7.4	Annealing effect	47
1.7.5	Dopant segregation.....	50
1.7.6	Effect of Cesium.....	63
1.7.7	Effect of cooling rate	69
1.8	Effect of reducing conditions on grain boundary conductivity	72
1.9	Nonlinear electrical properties of grain boundary.....	77
1.9.1	Electrical properties of individual GBs in large grained sample.....	82
1.10	PLD thin films and grain boundary properties	91
Conclusions		101
Abbreviations and Symbols.....		103
References		105
Acknowledgements		111
Curriculum Vitae		113

Zusammenfassung

Akzeptordotiertes BaZrO₃ zeigt im Temperaturbereich von 500°C bis 100°C eine hohe Protonenleitfähigkeit von $2 \cdot 10^{-2}$ S/cm bis $5 \cdot 10^{-5}$ S/cm. Elektrisch stark blockierende Korngrenzen behindern jedoch den Einsatz dieses Materials als Elektrolyt in Mitteltemperatur-Brennstoffzellen ernstlich. Bis jetzt konnte keine der üblichen Methoden (wie Pulverherstellung über chemische Methoden, Reaktivsintern oder Sinterhilfsmittel) die spezifische Korngrenzleitfähigkeit signifikant erhöhen. Untersuchungen des Sinterverhaltens zeigten, dass akzeptordotiertes BaZrO₃ nur ein sehr begrenztes Kornwachstum aufweist, was zu zehnfach kleineren Korngrößen als in undotiertem BaZrO₃ führt. Durch die Verringerung der Anzahldichte der Korngrenzen könnten größere Körner die Gesamtleitfähigkeit des BaZrO₃ erhöhen. Da jedoch die Steigerungsmöglichkeiten der Korngröße recht begrenzt sind, erscheint eine Verbesserung der spezifischen Korngrenzleitfähigkeit aussichtsreicher.

Diese Arbeit konzentriert sich auf die Charakterisierung der Korngrenzen, um ihren blockierenden Effekt in diesem Protonenleiter mit Perowskitstruktur besser zu verstehen. Die am häufigsten diskutierten Ursachen für blockierende Korngrenzen in Ionenleitern sollten überprüft werden:

- (i) eine zusammenhängende kristalline oder amorphe Zweitphase in der Korngrenze
- (ii) eine Verzerrung der Kristallstruktur im Bereich der Korngrenze, die zu verringerter Wasseraufnahme und/oder Protonenbeweglichkeit im Korngrenzbereich führen kann
- (iii) eine inhomogene Dotierkationenverteilung im Korngrenzbereich
- (iv) eine Verringerung der Protonen Konzentration in Raumladungszonen, die sich zur Kompensation einer Überschussladung im Korngrenz-Kern bilden.

Zweitphasen an den Korngrenzen als Ursache des blockierenden Charakters können aufgrund von TEM-Bildern, die saubere Korngrenzen zeigen, ausgeschlossen werden. Die analoge Veränderung von Volumen- und Korngrenzleitfähigkeit beim Wechsel von trockener zu angefeuchteter Gasatmosphäre weist darauf hin, dass sich Hydratisierung und Protonenbeweglichkeit im Korngrenzbereich nicht wesentlich vom Korninnern unterscheiden. Wegen des hohen Dampfdrucks von Bariumoxid erleiden konventionell gesinterte Proben durch langes Sintern bei hoher Temperatur typischerweise einen gewissen Bariumverlust. Dies beeinflusst die Korngrenzleitfähigkeit stärker als die Volumenleitfähigkeit. Obwohl zum Ausgleich ein Bariumüberschuss in der Ausgangszusammensetzung eingesetzt werden kann, ist eine genaue Kontrolle der Zusammensetzung bei konventionellem Sintern schwierig. Dies konnte durch Einsatz der "Spark Plasma Sintering"-Methode verbessert werden, die eine Minimierung der Bariumverluste durch sehr viel kürzere Sinterzeiten erlaubt. Damit gesinterte Keramiken erreichen eine höhere Dichte, und es ist möglich, die Proben unterschiedlich thermisch nachzubehandeln.

EDXS-TEM-Untersuchungen an Korngrenzen mit verschiedenen zusätzlichen Temperaturbehandlungen (die stark unterschiedliche Leitfähigkeiten ergeben) zeigten, dass sowohl Y- wie auch Sc-Dotierkationen in den Bereich der Korngrenzen segregieren, und dass Korngrenzen mit stärkerer Segregation einen niedrigeren Gesamtwiderstand aufweisen. Y^{3+} und Sc^{3+} wurden wegen ihrer unterschiedlichen Ionenradien als Dotierung gewählt; das größere Y^{3+} weist im Gegensatz zum kleineren Sc^{3+} eine große Fehlpassung zu Zr^{4+} auf. Der Vergleich zeigt, dass die Segregation dieser beiden Dotierionen hauptsächlich durch die elektrostatische Anziehung des positiv geladenen Korngrenz-Kerns getrieben ist. Dieser geladene Korngrenz-Kern verursacht auch die Verarmung von Protonen, Elektron-Löchern und Sauerstoffleerstellen in den angrenzenden Raumladungszonen. Durch Messung der elektrischen Eigenschaften der Korngrenzen unter angelegter Gleichspannung wurde das für Raumladungszonen erwartete nichtlineare Strom-Spannungs-Verhalten bestätigt. Dazu wurde mittels eines Infrarot-Spiegelofens eine Probe hergestellt, deren sehr große Körner es erlauben, ausreichend hohe Spannungen pro Korngrenze anzulegen. Die beobachteten spannungsabhängigen Korngrenzwiderstände und -kapazitäten stehen in Einklang mit der Annahme von Schottky-Barrieren an den Grenzflächen. Zur Interpretation der spannungsabhängigen Korngrenzkapazitäten werden zwei Modelle, mit und ohne zusätzliche elektronische Zustände im Bereich des Korngrenz-Kerns, diskutiert.

Auf der Grundlage dieser Beobachtungen wurde der Ba-Platz mit Cs^+ dotiert, um einen weiteren Mechanismus zur Kompensation der Überschussladung des Korngrenz-Kerns zu ermöglichen. Durch seine Größen-Fehlpassung ($r_{\text{Cs}^+} = 1.88 \text{ \AA}$, $r_{\text{Ba}^{2+}} = 1.61 \text{ \AA}$) und die elektrostatische Anziehung des positiv geladenen Korngrenz-Kerns hat Cs'_{Ba} eine große Triebkraft für eine Segregation in den Bereich der Korngrenze. Leitfähigkeitsmessungen zeigten, dass bereits 1 at.% Cs die Korngrenzleitfähigkeit von Y-dotiertem BaZrO_3 um mehr als 2-3 Größenordnungen erhöhen kann.

Zusammenfassend kann aufgrund der systematischen strukturellen, chemischen und elektrischen Untersuchungen festgestellt werden, dass eine positive Überschussladung des Korngrenz-Kerns die Hauptursache für den blockierenden Charakter der Korngrenzen in akzeptordotiertem BaZrO_3 darstellt, da sie zur Protonen-Verarmung in angrenzenden Raumladungszonen führt. Diese Untersuchungsergebnisse konnten erfolgreich dazu verwendet werden, die Korngrenzleitfähigkeit durch entsprechende Temperaturbehandlung oder gezieltes Einbringen von Dotierionen im Bereich der Korngrenzen zu verbessern. Eine Übertragung dieser Ergebnisse auf andere elektrokeramische Materialien, für die die Korngrenzeigenschaften ebenfalls wichtig sind, ist denkbar.

Abstract

Acceptor doped BaZrO₃ exhibit a high bulk proton conductivity of $2 \cdot 10^{-2}$ S/cm to $5 \cdot 10^{-5}$ S/cm in the temperature range of 500°C to 100°C. Nevertheless, highly resistive grain boundaries and notoriously small grain sizes seriously hamper the application of this material as an electrolyte in intermediate-temperature solid oxide fuel cells. Up to now, none of the usual methods (such as powder synthesis via chemical methods, reactive sintering, and sintering aids) could considerably improve the specific GB conductivity of this material. Investigation on sintering properties showed that acceptor-doped BaZrO₃ exhibits a limited grain growth resulting in grain sizes 10 times smaller than undoped BaZrO₃. Larger grains, by decreasing the GB number density, can improve the total conductivity of BaZrO₃. Nevertheless, due to the limited range for the expected grain size increase, a modification of specific GB conductivity seems much more effective.

This work is focused on characterization of grain boundaries to get a better understanding of the blocking effect in this perovskite structure proton conductor. It was attempted to check the most frequently reported origins for the blocking character of GBs in ion conductors:

- (i) Presence of continuous secondary/amorphous phase at GB
- (ii) Distorted crystallographic structure of grain boundary region which can result in a low water solubility and/or lower proton mobility in GB region
- (iii) Inhomogeneous distribution of dopant cations in GB region
- (iv) Depletion of protonic charge carriers in space charge layers which form to compensate an excess charge in the GB core

Based on TEM images showing clean GB, secondary phases at the GB could be ruled out as origin for the blocking character. The similar change of bulk and GB conductivity upon

switching from dry to wet atmosphere indicated that hydration behaviors and proton mobility in the GB region do not significantly differ from bulk.

Due to high vapor pressure of barium oxide, the conventionally sintered samples typically suffer a certain barium loss due to the long-term high-temperature sintering step. The effect of barium loss is more pronounced for the GB conductivity than for the bulk. Although some extra barium can be added in the starting composition to compensate the loss, composition control is not easy using the conventional sintering method. This situation could be improved by “Spark Plasma Sintering” which allows one to minimize Ba deficiency due to much shorter sintering times. The sintered ceramic achieves a higher density and offers the possibility of applying an additional post-heat treatment.

EDXS-TEM studies on GBs with different heat treatments (resulting in strongly different conductivities) showed that Y as well as Sc dopants segregate to the GB region, and that GBs with a higher amount of segregation exhibit a lower resistivity. Y^{+3} and Sc^{+3} cations were chosen due to their different ionic radius; the large Y^{+3} cation exhibits a large size mismatch in Zr^{+4} site in contrast to Sc^{+3} with a negligible size mismatch. The comparison revealed that for those two dopants segregation is mainly driven by electrostatic forces due to a positively charged core, which is responsible for depletion of protons, holes and oxygen vacancies in the adjacent space charge zones. The segregated dopants increase the GB conductivity partly by directly compensating the positive charge in the core, and partly by accumulation in the space charge zone decreasing the thickness of the depletion layer.

Further evidence for a positive core charge comes from measurements on strongly reduced n-conducting Y-doped $BaZrO_3$, where the blocking GB character disappears. This finding is a clear evidence for a positively charged core and consequently related depletion/accumulation layers in adjacent space charge zones.

The expected non-linear current-voltage character of the proposed space charge zones was confirmed studying the electrical behavior of GBs under DC-bias. For this purpose, a large grain sample, allowing to apply a reasonable DC bias over each GB, was prepared in an Infrared Image Furnace. The observed voltage-dependent GB resistances and capacitances are consistent with a Schottky-type barrier at the interface. Two models, with and without interface states, are discussed to explain voltage dependence of the GB capacitance.

Based on these findings, as an alternative core charge compensation, the Ba-site was doped with Cs^+ cations. Cs'_{Ba} has a high tendency to segregate to the GB region due to its size

mismatch ($r_{\text{Cs}^+} = 1.88 \text{ \AA}$, $r_{\text{Ba}^{+2}} = 1.61 \text{ \AA}$) and electrostatic interaction with positive core. The conductivity measurements showed that only 1 at.% of Cs can increase GB conductivity of Y-doped BaZrO_3 by more than 2-3 orders of magnitude.

In summary, from the systematic structural, chemical and electrical characterization a positive GB core charge resulting in space charge depletion of protons could be identified as the major causes for the blocking effect of GBs in acceptor-doped BaZrO_3 . This investigation has been successfully used to increase conductivity of GB by adjusting heat treatment or by applying adequate GB decoration. These results may be extended to other electroceramic materials for which GB properties are important.

Chapter 1

Introduction and Motivation

1.1 Solid Oxide Fuel Cells and proton conducting oxides

Solid oxide fuel cells (SOFCs) are clean power sources which convert chemical energy to electricity at elevated temperatures. Their efficiency is not restricted by Carnot's limit, and they have the advantage of easily scalable power output^[1]. Usually, oxygen ion-conducting oxides such as Y-stabilized zirconia are used as electrolyte material. Most of these electrolyte oxides exhibiting enough conductivities (≈ 0.01 to 1 Scm^{-1}) only at high temperatures (800-1000°C) while their conductivities decreasing significantly with temperature (typical $E_a = 0.7$ to 1 eV). Therefore, SOFCs typically require high working temperatures if oxide ion conductors are used as electrolyte. The high operating temperature leads a reduced service life of the cell, limits materials selection and increases costs. At lower temperatures, material selection for different parts is less limited, sealing becomes easier, fabrication of small modules more feasible and theoretical energy efficiency increases. Therefore, better electrolytes are necessary to establish intermediate-temperature SOFCs.

Oxide proton conductors with the potential of high conductivities at temperatures below 700°C could allow a significant decrease in the operating temperature. The first application of proton conducting perovskite oxide^[2] electrolytes in fuel cells (with different kinds of fuels) as well as for humidity and hydrogen sensors was reported in 1980s^[3-5].

In the last four decades, proton conductivity has been observed in many perovskite and non perovskite structures. **Table 1** summarizes the most important oxides which exhibit proton conductivity in wet atmosphere. Up to now perovskite structured oxides, exhibit the highest proton conductivities when compared to sesquioxides (e.g. Y_2O_3 , Al_2O_3 , ...), pyrochlore (e.g.

$\text{Ln}_2\text{Zr}_{1.8}\text{Y}_{0.2}\text{O}_{7-\delta}$) and fluorite type structures (e.g. $\text{Ce}_{0.8}\text{M}_{0.2}\text{O}_{2-\delta}$). Solid acids^[6] such as CsHSO_4 have good proton transport properties, but their proton conductivity is limited by the phase transition at 141 °C and decomposition/melting at approximately 200–230 °C.

Among the perovskite proton conductors, acceptor doped cerates (ACeO_3 , $A = \text{Ba, Sr}$)^[7, 8] and zirconates (AZrO_3 , $A = \text{Ba, Sr, Ca}$)^[2, 9, 10] have been widely investigated. The conductivity of cerates is higher than zirconates, however, zirconates exhibit a better chemical stability in CO_2 , water and H_2 containing atmospheres.

It should be mentioned that there are some oxides with relatively high proton conductivities which exhibit a high electronic contribution and therefore cannot be used as electrolyte material (e.g. BaPrO_3). Also, some proton conducting compounds have a poor chemical or mechanical stability upon hydration and in reducing atmospheres (e.g. $\text{Ba}_2\text{YSnO}_{5.5}$ and $\text{Ba}_2\text{In}_2\text{O}_5$).

Table 1 Proton conducting oxides and their conductivity at 600°C and 300°C (total conductivity unless mentioned otherwise), the compounds with * are predominantly electronic conductors

Formula	Composition (Examples)	$\sigma_{600^\circ\text{C}}$ (Scm^{-1})	$\sigma_{300^\circ\text{C}}$ (Scm^{-1})
$\text{A}(\text{M}_x\text{B}_{1-x})\text{O}_3$	ACeO_3 ($A = \text{Ba, Sr}$)...	10^{-3} - 10^{-2} [7, 8, 11]	
II-IV Perovskite			
$M=\text{Y, Sc, Yb, In, Nd, Gd, Ga, ...}$	AZrO_3 ($A = \text{Ba, Sr, Ca}$)	10^{-4} - 10^{-3} [10, 11] 10^{-2} [12] (large grain)	$\sim 10^{-3}$ [12, 13]
	BaBO_3 ($B = \text{Pr, Tb, Th}$)*	0.1 [14, 15]	5×10^{-3} [15]
$(\text{Ln}_x\text{A}_{1-x})\text{BO}_3$	$A = \text{Ba, Ca, Mg}$ LnBO_3 ($B = \text{Y, Er, Al, Sc}$)	1 - 5×10^{-5} [16, 17]	
III-III Perovskite			
$\text{A}_2\text{B}'_{1+x}\text{B}''_{1-x}\text{O}_{6-\delta}$	$\text{Sr}_2(\text{Ga}_{1+x}\text{Nb}_{1-x})\text{O}_{6-\delta}$, $x = 0.1$ - 0.2		5×10^{-6} [18]
layered perovskite	$\text{Sr}_2(\text{Sc}_{1+x}\text{Nb}_{1-x})\text{O}_{6-\delta}$, $x = 0.05$ - 0.1		1×10^{-5} [19]
$\text{A}_3\text{B}'_{1+x}\text{B}''_{1-x}\text{O}_{9-\delta}$	$\text{Sr}_3(\text{Ca}_{1.18}\text{Nb}_{1.82})\text{O}_{9-\delta}$		5×10^{-5} [20]
layered perovskite	$\text{Ba}_3(\text{Ca}_{1.18}\text{Nb}_{1.82})\text{O}_{9-\delta}$	10^{-3} [21]	3×10^{-7} [21]
K_2NiF_4 type	$\text{La}_{1-x}\text{Ba}_{1+x}\text{GaO}_{4-\delta}$	3×10^{-4} [22]	2×10^{-5} [22]
layered perovskite related	$\text{La}_{1-x}\text{Sr}_{1+x}\text{AlO}_{4-\delta}$	1 - 2×10^{-5} [23]	
Niobate and Tantalate	$\text{Sr}_6\text{M}_2\text{O}_{11}$	$\sim 10^{-4}$ - 10^{-3} [24]	$\sim 10^{-6}$ [24]
Perovskite related	$M = \text{Nb, Ta}$		

Table 1 continued

Formula	Composition (Examples)	$\sigma_{600^\circ\text{C}}$ (Scm ⁻¹)	$\sigma_{300^\circ\text{C}}$ (Scm ⁻¹)
A ₂ B ₂ O ₅ (stannate)	Ba ₂ YSnO _{5,5}	$\sim 10^{-3}$ [25]	$2-5 \times 10^{-4}$ [25, 27]
Brownmillerite (O deficient Perovskite superstructure)	Ba ₂ InSnO _{5,5}		
	Ba ₂ In ₂ O ₅	$\sim 10^{-4}$ [26]	$\sim 10^{-6}$ [26]
Pyrochlore	Y-doped Ln ₂ Zr ₂ O ₇ (In,Mg) doped Y ₂ Ti ₂ O ₇	$1-4 \times 10^{-4}$ [28]	
Fluorite	La _{3-x} Sr _x NbO _{7-δ}	2×10^{-4} [23] (x = 0)	
	La _{5,8} WO _{11,7}	2×10^{-3} [29]	
Aragonite	3% Sr-doped LaBO ₃	2×10^{-6} [29]	
	1% Sr-LaBO ₃	4×10^{-5} [30]	
<i>RE</i> _{1-x} <i>M</i> PO ₄ and <i>RE</i> _{1-x} <i>M</i> (PO ₃) ₃	<i>M</i> = Ca, Sr, Ba	$10^{-5} - 10^{-4}$ [31-34]	1×10^{-6} [33, 34]
Monazite	<i>RE</i> = La, Y		
Phosphate	3-20% In-SnP ₂ O ₇		0.1-0.2 [35]
<i>RE</i> _{1-x} <i>M</i> NbO ₄ and <i>RE</i> _{1-x} <i>M</i> TaO ₄	<i>RE</i> = La, Nd, Tb, Gd	10^{-4} [36, 37]	very low below 500°C
Fergusonite	<i>M</i> = Ca		
(<i>M</i> _x , <i>RE</i> _{2-x})O ₃	<i>RE</i> = Y, Gd, Sm, La, Nd, Er	$10^{-5} - 10^{-4}$ [38, 39]	
Rare Earth sesquioxides	<i>M</i> = Mg, Ca		
Ln _{10-x} (Si/GeO ₄) ₆ O _{3-1.5x}	La _{10-x} (GeO ₄) ₆ O _{3-1.5x}	$\sim 10^{-6}$ [40]	
Apatite	0.25 ≤ x ≤ 0.45		
Others	La ₂ Si ₂ O ₇ (undoped and Sr doped)	$1-2 \times 10^{-6}$ [41]	
	Sr ₂ (Ti _{1-y} , Zr _y)O ₄	10^{-3} [42]	

1.2 Protonic defects and proton mobility

Substitution of acceptor dopants (M^{+3}) at the B site in $A^{+2}B^{+4}O_{3-\delta}$ perovskites introduces effective negative charges which (for B cations that do not change oxidation state) are predominantly compensated by positively charged oxygen vacancies ($V_O^{\bullet\bullet}$) according to Kröger-Vink notation^[43]:



A water molecule dissociates into a hydroxide (OH^{\bullet}) which fills an oxygen vacancy and a proton which binds to a lattice oxygen, thus two positively charged protonic defects are generated.



The proton incorporation reaction is governed by the equilibrium constant K_w , assuming ideally dilute defects, i.e. getting activities equal to concentrations.

$$K_w = \frac{[\text{OH}_\text{O}^{\bullet}]^2}{[\text{V}_\text{O}^{\bullet\bullet}][\text{O}_\text{O}^{\text{X}}]p\text{H}_2\text{O}} \quad (3)$$

The negative entropy ($\Delta S_{\text{hyd.}}^\circ < 0$) of the hydration reaction (**eq.(2)**) is compensated by the negative enthalpy ($\Delta H_{\text{hyd.}}^\circ < 0$) of reaction at low temperatures. With increasing temperature, the entropy term ($-T\Delta S_{\text{hyd.}}^\circ > 0$) is more effective and formation of water molecules in the gas phase becomes thermodynamically more favorable. The hydration behavior (**Fig. 1**) of acceptor-doped BaZrO_3 and BaCeO_3 , obtained by thermogravimetric analysis, shows that full hydration of the structure is achieved below 450°C for Y-doped BaZrO_3 .

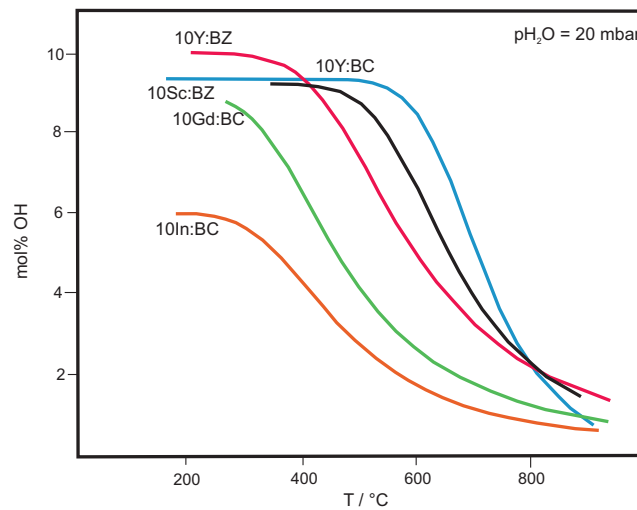


Figure 1 Hydration isobars for 10% acceptor doped BaZrO_3 (BZ) and BaCeO_3 (BC) obtained by thermogravimetric analysis^[44]

Oxidation occurs via the following reaction with equilibrium constant of K_{OX} :



$$K_{\text{OX}} = \frac{[\text{O}_\text{O}^{\text{X}}][\text{h}^{\bullet}]^2}{[\text{V}_\text{O}^{\bullet\bullet}]p\text{O}_2} \quad (5)$$

The excess electron concentration is calculated using the internal electronic equilibrium:

$$K_1 = [e'][\text{h}^{\bullet}] \quad (6)$$

In addition, cation vacancy at A-site (V_A''), and cation vacancy at B-site (V_B'''') can appear as point defects in $ABO_{3-\delta}$ perovskites. The complete electroneutrality condition reads:

$$2[V_A''] + [M_B'] + 4[V_B'''] + [e'] = 2[V_O''] + [OH_O'] + [h'] \quad (7)$$

The concentrations of holes, oxygen vacancies and protons are controlled by dopant concentration, pO_2 , pH_2O and T . Assuming a negligible concentration of cation vacancies, concentration of defects as a function of oxygen and water partial pressures is shown in **Fig. 2** [45-48].

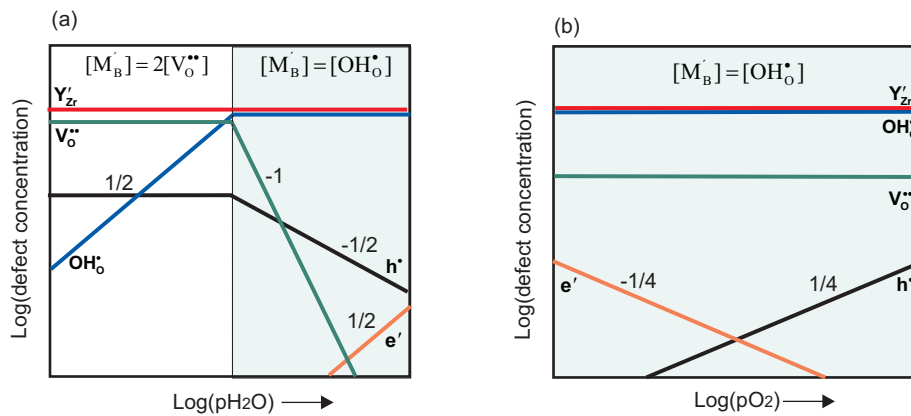
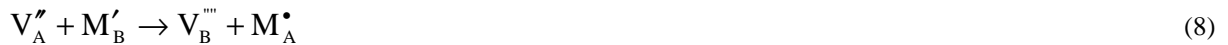


Figure 2 Brouwer defect diagram; (a) pH_2O dependence and, (b) pO_2 dependence at high water vapor pressure

Furthermore, A-site deficiency due to AO loss can affect the proton conductivity of the material. In highly doped perovskites, the dopant cation can become a donor dopant by site exchange to the partially empty A-site (eq. (8)) with subsequent consumption of oxygen vacancies by the backward Schottky reaction (eq. (9)).



In slightly doped and undoped ABO_3 , loss of AO leads to decomposition of the perovskite structure and formation of BO_2 . The actual composition depends on the type of dopant and sintering conditions^[49-52].

In a perovskite oxide, protons exhibit rotational motion and stretching vibrations (**Fig. 3**). The rotation of O-H bond around the oxygen ions is easy (low activation barrier) and does not lead to long-range migration. On the other hand, elongation of the O-H bond leads to proton transfer between neighboring oxygen ions and consequently a long range proton diffusion. The actual proton jump along the edge of the BO_6 octahedron preferentially occurs when the two oxygen ions exhibit a decreased distance owing to a transient distortion of the

octahedron^[53-55]. It is suggested that proton mobility in acceptor doped perovskite oxides is sensitive to the concentration^[56] and type of dopant cations^[55, 56] and decreases for noncubic (low symmetry) perovskites^[55].

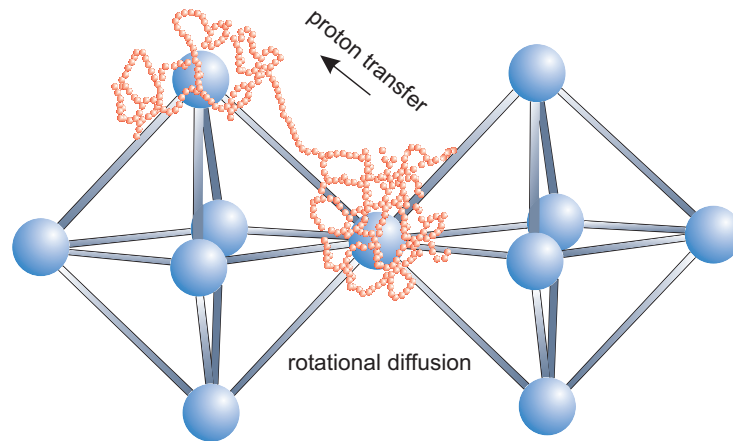


Figure 3 Proton transport; rotational diffusion and proton transfer obtained by quantum-MD simulation of a proton in cubic BaCeO₃ ^[55]

1.3 Acceptor doped BaZrO₃, its potentials and limitations

Using proton conductors as electrolyte eliminates the problem of water formation at the anode side, which dilutes the fuel in case of using oxide ion conductors. However, they can be used as an electrolyte only when they exhibit good chemical stability and a total conductivity comparable to the oxide ion conductors. Among the oxide proton conductors, Y-doped BaZrO₃ with excellent chemical stability and relatively high total conductivity is a good candidate. **Fig. 4** compares the bulk conductivity of Y-doped BaZrO₃ to the best oxide ion conductors. The bulk conductivity of this material is, particularly at low temperatures, higher than that of the other electrolytes. However, the total conductivity of polycrystalline acceptor-doped BaZrO₃ is limited by the high resistivity of its grain boundaries^[55, 57, 58]. In addition, its poor sintering properties introduce a high density of blocking grain boundaries even after long time at high temperatures (1700°C/20h)^[59-63].

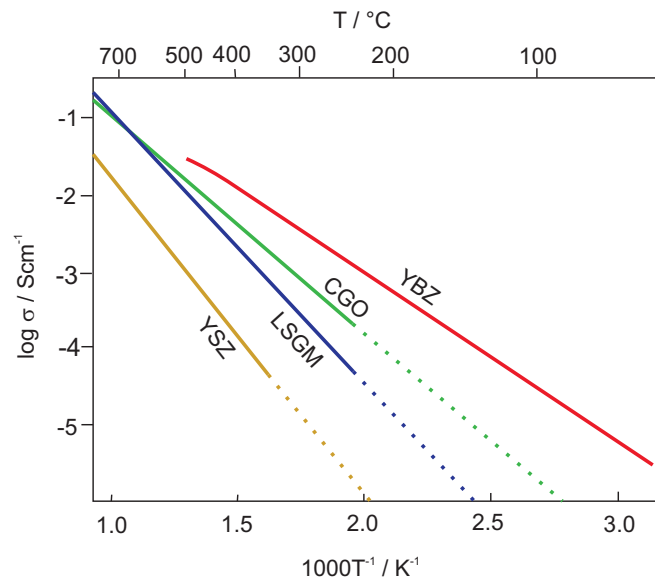


Figure 4 Conductivity values of electrolyte oxide ion conductors, $\text{Ce}_{0.9}\text{Gd}_{0.1}\text{O}_{1.95}$ ^[64], $\text{La}_{0.9}\text{Sr}_{0.1}\text{Ga}_{0.8}\text{Mg}_{0.2}\text{O}_{2.85}$ ^[64], $(\text{ZrO}_2)_{0.9}(\text{Y}_2\text{O}_3)_{0.1}$ ^[64] and proton conducting $\text{Ba}(\text{Zr}_{0.8}\text{Y}_{0.2})\text{O}_{3-\delta}$ -bulk^[55].

Fig. 5 shows a collection of bulk and total conductivities reported for Y-doped BaZrO_3 . The bulk conductivity increases systematically (but non-linearly) with dopant concentration, and reported conductivities from different groups are in good agreement. On the other hand, the total conductivities, dominated by the grain boundary contribution, are much lower and remarkably scattered. The total conductivity does not even show a systematic increase with dopant concentration. Obviously the grain boundary conductivity is more sensitive to experimental conditions, such as for powder preparation and sintering.

Up to now, there has been a lot of research to understand^[59, 60, 65, 66] and improve the GB conductivity of acceptor doped BaZrO_3 either by increasing the specific GB conductivity or by decreasing the number of GBs via grain growth^[12, 61, 62, 67-71]. Powder synthesis via chemical methods^[12, 67], adding sintering aids like ZnO ^[61, 70], NiO ^[71], CuO ^[72], MgO ^[68], co-doping of Zr site^[73, 74] are a few examples of such attempts to improve the overall conductivity of this material.

The chemical methods^[67, 69] did not lead to a meaningful improvement of GB electrical properties. Some modified sintering methods such as reactive sintering^[12] offered a certain grain growth but did not lead to a significant conductivity enhancement (< 0.5 orders of magnitude). Despite achieving a larger grain size, most of the sintering aids^[61, 68, 70] (MgO ,

Al_2O_3 , Bi_2O_3 , Mo and TiO_2) increased the specific resistivity of the grain boundaries and lead to decreased overall conductivities.

Besides many experimental efforts to improve the GB conductivity, theoretical calculations (Reactive Force Field)^[75] tried to explain the blocking character of the GB and suggest possible solutions.

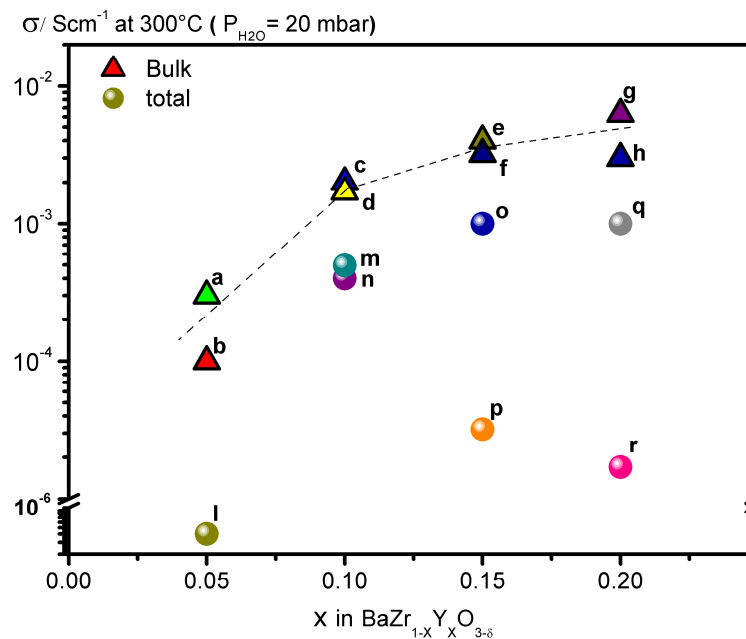


Figure 5 Bulk conductivity (triangle) and total conductivity (spheres) of x at.% Y-doped BaZrO₃ at 300°C and wet atmosphere from literature as (a,g)^[44], (b,c,e,n,o,l)^[60], (d,m)^[13], (f,p)^[55], (h)^[12], (q)^[67], (r)^[63].

Based on this situation, the motivation for this work is twofold. First, to identify and understand the reason(s) for blocking GBs in acceptor-doped BaZrO₃. Second, to find means to improve the conductivity of GB.

1.4 Blocking character of grain boundaries

In this section, the potential origins for the blocking character of GBs in oxides in general and also some points specific to acceptor-doped BaZrO₃ will briefly be discussed.

1.4.1 Secondary phase

Impurities like SiO_2 can usually form a continuous insulating layer at the grain boundaries of ceramics. It has been frequently shown that this intergranular phase significantly affects the GB electrical properties of oxides such as acceptor doped ZrO_2 ^[76]. Since location and composition of the secondary phase is influenced by the impurity content of the starting powder as well as the sintering conditions, discrepancies in reported GB conductivities for the same polycrystalline material are expected. It is worth to mention that the blocking effect caused by a secondary phase (“current constriction”) usually does not show a significant change in the activation energy of GBs compared to the bulk of material^[77, 78]. Only in case of completely covering secondary phase change in activation energy is expected^[78].

1.4.2 Grain boundary structure

The blocking effect can also be influenced by formation of high angle and/or asymmetrical grain boundaries^[79]. The crystallographic character of grain boundaries can change by type or amount of dopant/impurity^[80], however, up to now no reliable correlation between the conductivity of Y-doped BaZrO_3 and orientation of the grain boundary could be recognised^[60].

1.4.3 Space charge layers

Grain boundary blocking effects in many polycrystalline oxides (typically with large band gaps, e.g. SrTiO_3 , ZrO_2 , TiO_2 and CeO_2)^[81-87] have been explained by the presence of space charge layers. According to the space charge theory in solids^[88], interfaces such as grain boundaries are electrically not neutral for ionic compounds. The charge at the grain boundary core is compensated by charge of opposite sign in adjacent layers. Therefore, the electrical properties of grain boundary are mainly defined by the defect structure of the so-called space charge zones^[89]. In the case of low-angle GBs in SrTiO_3 , the positive charge of the core has been explained by formation of oxygen vacancies in the GB core^[87, 90-92], which are assumed to be immobile^[90]. In most studies the existence of charged GB core has been confirmed

indirectly using electrical measurements^[86, 93-100]. Moreover, TEM-electron holography has also been used to directly measure the electrical potential of grain boundary. There have been some dispute about the sign obtained using this method^[101], but a very recent^[102] electron holography study on SrTiO₃ has observed a positively charged core.

The existence of space charge layers and proton depletion due to a positive core charge has been discussed for Y-doped BaZrO₃ based on a modified pO₂ dependence of the GB conductivity^[66]. In addition to the GB electrical properties, the composition of the grain boundary region can strongly be influenced by the charged GB core which acts as driving force for dopant segregation to the GB.

A more detailed picture of GB defect structure can be obtained by using Mott-Schottky and Gouy-Chapman models.

- **Gouy-Chapman:** In this model (**Fig. 6-a**), dopant cations are sufficiently mobile to contribute to the compensation of the core charge and therefore dopant cations (with charge of z_d) follow the equilibrium concentration according to

$$\frac{c_d(x)}{c_{d,bulk}} = \exp\left(\frac{-z_d e \Phi(x)}{kT}\right) \quad (10)$$

and width of the depletion zone, the so-called Debye length, is expressed as

$$\lambda = \sqrt{\frac{\epsilon \epsilon_0 kT}{2z_d^2 e^2 c_{d,bulk}}} \quad (11)$$

- **Mott-Schottky:** In this model (**Fig. 6-b**), the dopant cations are immobile and their concentration is constant within the system, in the GB region as well as in the bulk ($c_d(x) = c_{d,bulk}$) and the space charge zone is extended to λ^* as

$$\lambda^* = \sqrt{\frac{2\epsilon_0 \epsilon_r \Phi_0}{e z_d c_{d,bulk}}} = \lambda \sqrt{\frac{4e\Phi_0}{kT}}, \quad \Phi(x=0) = \Phi_0 \quad (12)$$

The depletion profile of majority mobile charge carriers is

$$\frac{c_i(x)}{c_i(bulk)} = \exp\left[-\frac{z_i}{z_d} \left(\frac{x - \lambda^*}{2\lambda}\right)^2\right] \quad (13)$$

where z_i is the charge of mobile carriers. The space charge potential Φ_0 is related to the bulk and GB conductivities as

$$\frac{(RC)_{GB}}{(RC)_{bulk}} = \frac{\exp(z_i e \Phi_0 / kT)}{2z_i e \Phi_0 / kT} \quad (14)$$

R and C denote the resistivity and capacitance, respectively; z is the charge (z_d is 1 for Y dopant, z_i is 1 for protons and 2 for oxygen vacancies). Φ is the GB potential barrier, T is temperature, c_d is dopant concentration in unit volume and e , ε , ε_0 and k have their usual meanings. $\delta_{GB} = 2\lambda$ (Gouy-Chapman) or $2\lambda^*$ (Mott-Schottky) is the effective (electrical) GB thickness (measured in impedance spectroscopy), i.e. total width of the depletion zone.

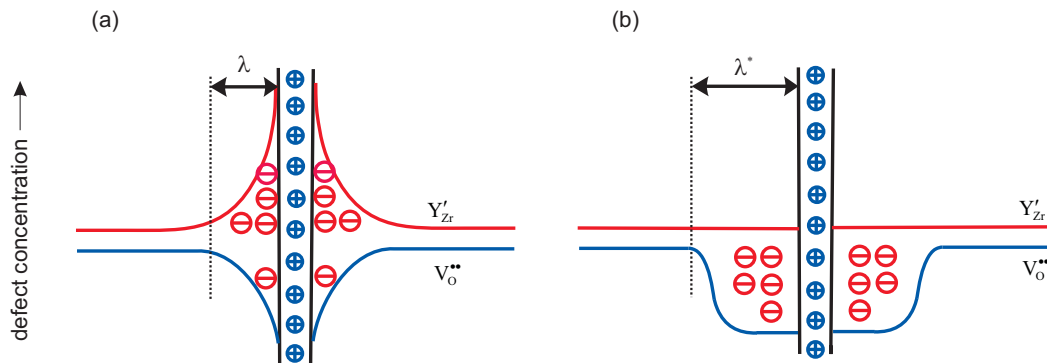


Figure 6 Space charge model (a) Gouy-Chapman and (b) Mott-Schottky situations

1.4.4 Segregation

In general, segregation refers to the enrichment of a cation (dopant or impurity) in the grain boundary region (core and adjacent space charge zone). Owing to the ionic bonds, segregation in ceramics^[103-107] is more complicated than in metals since it can additionally give rise to a change in charge density corresponding to a redistribution of defects in GB region. Defect profile and dopant segregation in the GB region are coupled to each other and the resulting defect profile determines the electrical properties of grain boundary. Most frequently, elastic and electrostatic driving forces are regarded as dominating driving forces for cation segregation in ionic materials^[103, 105, 108-110]. Different defect formation energies, effects of ambient atmosphere, surface energy and interaction between defects, have been discussed as other possible driving forces for segregation. However, since the space charge region is caused by different defect formation energies and is not independent of surface energy, it is difficult to separate these effects^[110].

An oversized dopant cation introduces an extra strain energy into the system. The typically more disordered and more open grain boundary core structure can be a favorable place to release this excess energy and reduce the energy of system. Therefore, once the cation

movement becomes kinetically possible (typically close to sintering temperature), oversized dopant cations move to some extent to the grain boundary core; the larger the cation, the larger the mismatch and consequently the higher the tendency for segregation. It is noteworthy that the effective elastic interaction is limited to a small distance, typically in the range of two lattice constants^[103, 108].

Segregation to the grain boundary region of ceramic oxides can be also driven by the coulombic interaction between the effectively charged dopant cation and charged GB core^[103, 104, 106-109, 111, 112]. Indeed, the core charge and dopant profile in GB region are coupled to each other and dopant segregation modifies the charge density and results in a new electrostatic potential. The experimental data has shown that electrostatic interactions are the major driving forces for dopant segregation in acceptor-doped ceria and zirconia^[107, 108, 112-119].

The time for the dopant to reach the actual equilibrium concentration profile depends on the diffusivity of the dopants in the crystal. Additionally, segregated dopants decrease the mobility of grain boundaries in the sintering process by applying a drag force on the GB plane, depending also on the amount of segregant in the GB region^[107, 112, 114-119].

1.4.5 Specific features for BaZrO₃

Some other reasons that are specific for BaZrO₃ might contribute to the blocking GB effect in this material. For instance, the high vapour pressure of barium oxide at the required sintering temperature causes BaO loss and lowers the conductivity of Y doped BaZrO₃ (even stronger at the GB than in the bulk)^[67, 120]. Since pores are typically connected to GBs, a larger amount of barium loss in the GB region might be a reason for lower conductivity of GBs. Furthermore, keeping in mind that a symmetry decrease in acceptor doped BaZrO₃ lowers the bulk conductivity^[55], the distorted crystallographic structure of grain boundary region with a lower degree of symmetry could result in lower water incorporation and/or lower proton mobility and consequently a lower proton conductivity.

Chapter 2

Experimental

1.5 Sample preparation

1.5.1 Single phase powders

Single phase powders of acceptor doped BaZrO₃ were prepared by solid state reaction. BaCO₃ (Merck, 99%), Y-stabilized ZrO₂ (TOSOH, TZ-0Y, TZ-3Y, TZ-8Y), Sc-doped ZrO₂ (FCM Sc10SZ-TC) and Cs₂CO₃ (Merck-99.5%) were used as starting materials. In the first step, the starting materials were mixed in an agate mortar in the required quantities and calcined at 1100°C in air for 1.5 hours. The calcined powder was ground for 2 hours in a ball mill (1 big zirconia ball of 5 cm diameter) and the single phase powder was obtained after another 2 cycles of calcination at 1300°C followed by 2 hours grinding.

CsNO₃ (Alfa Aesar 99.99%) and calcined Y-doped BaZrO₃ were used to prepare cesium decorated samples. The 6 at.% Y-doped BaZrO₃ powder was added to a solution of cesium nitrate in distilled water. The suspension was stirred till water was evaporated. The calcined Y-doped BaZrO₃ powder had a BET surface area of ~ 6 m²/g. To cover 20% of the available surface sites by Cs ions (if each Cs ion needs an area of 0.1 nm²), 2×10⁻⁵ mol of Cs for 1 g YBZ powder was used, corresponding to an overall concentration of 0.006 at.% Cs. This amount of Cs introduces a high cesium concentration at the grain boundary of the decorated sample. To avoid formation of Cs₂CO₃, the cesium doped and decorated samples were calcined under N₂ atmosphere (800 °C for 10 hours) before sintering by the SPS method.

1.5.2 Polycrystalline samples

1.5.2.1 Conventional sintering

The calcined powder was isostatically pressed (250 MPa). The pressed pellet was sintered in a zirconia crucible at 1700°C for 20 hours (heating rate = 200°C/h, cooling rate = 50°C/h). The sample was covered with sacrificial powder of the same composition to decrease barium loss during sintering. The outer part of sintered pellets (dark green) was removed and only the inner part used for investigation. Despite long sintering, the typical density was only ~ 90% of theoretical density.

1.5.2.2 Spark plasma sintering (SPS)

“Spark Plasma Sintering” was used to produce dense polycrystalline samples. SPS is a hot-pressing technique with the help of which the sample in a graphite die is heated directly by a pulsed DC current through the die under uniaxial pressure. The calcined single phase powder was sintered under a pressure of 50 MPa at 1600°C for 5 minutes (HP D 5, FCT Systems GmbH). In SPS, high heating (100°C/min) and cooling (200 to 400°C/min) rates are used. The slightly lower sintering temperature and in particular the shorter holding time are major advantages of the SPS method in order to lower the amount of Ba loss.

The sintered pellets were heated up to 800°C for 10 hours to get rid of remaining graphite at the surface. To avoid any possible inhomogeneity in the as-prepared SPS samples, a relatively thick layer was always removed from the outer parts.

1.5.3 Large grained sample

For the feed rod for the image furnace, 6 at.-%-doped BaZrO₃ was prepared by the standard solid-state reaction route. To compensate at least a part of barium loss at high temperature, 5wt% extra BaCO₃ was added to the starting mixture. The calcined powder was pressed to a rod (diameter = 5 mm, length = 100 mm) under isostatic pressure of 500 MPa. The pressed rod, cut into a seed rod and a feed rod, was heated in an optical floating zone furnace (Crystal System Incorporation, Japan) with 4 xenon lamps installed as arc radiation sources to reach temperatures higher than 2600°C. The crystal growth chamber (quartz tube) was firstly

evacuated to 10^{-4} Tor and flushed with high purity Ar (5.0). This cleaning procedure was cycled at least three times. Ar (95%) mixed with oxygen (5%) was then allowed to flow through the chamber. The seed and feed rods were rotated at 25 rpm in opposite directions and heated to form a stable molten zone of uniform temperature and homogeneous composition. A growth rate of ~ 5 -8 mm/h was applied throughout the growing procedure. Then the grown crystal was cooled in the chamber during 36 hours to avoid cracks in the as-grown crystal. A substantial evaporation of BaO was observed from the floating-zone. The resulting rod was cut into different pieces for further investigations. This work was done by the “Crystal Growth Group” of the Max Planck Institute for Solid State Research.

1.5.4 Thin films

YBZ films were deposited by pulsed laser deposition (PLD), using a KrF excimer laser ($\lambda = 248$ nm) at a repetition frequency of 10 Hz (LPX200, Lambda Physik, Germany).

The substrate temperature (600-700°C), oxygen partial pressure (10^{-4} - 10^{-2} atm), film thickness (100-1000 nm) and energy density (1.6-3 J/cm²) have been changed as control parameters to achieve epitaxial layers of Y-doped BaZrO₃. MgO single crystal (CrysTec, Germany) with (100) orientation and MgO bi-crystals (CrysTec, Germany) have been used as substrate. One bicrystal had 24° misorientation angle around $\langle 100 \rangle$ close to $\Sigma 13$ and the other one had 36.8° misorientation angle around $\langle 100 \rangle$ close to $\Sigma 5$. An SPS pellet was used as target. The film deposition was done in the “Technology Service Group” of the Max Planck Institute for Solid State Research.

1.6 Sample characterization

1.6.1 X-ray diffraction

X-ray diffraction (XRD) was used for phase identification and crystal structure refinement of polycrystalline and large grain samples. Data were collected at room temperature in Bragg-Brentano reflection geometry with a Philips PW 3710 diffractometer using CuK α radiation ($\lambda = 1.5418$ Å, 40 kV and 30 mA). Each measurement covered $2\theta = 10^\circ$ - 90° , with step size of

0.02° and detection time of 15 seconds per step. Lattice parameters were refined with whole powder pattern decomposition (Le Bail fitting method) in TOPAS 2.1 provided by BRUKER. The X-ray diffraction analysis of the thin films was carried out with a Bruker AXS D8 Discover Superspeed diffractometer equipped with a SolX energy dispersive detector operating with Cu-K α radiation source ($\lambda = 1.5406 \text{ \AA}$), 50kV and 20 mA.

1.6.2 Scanning electron microscopy

Scanning electron microscopy (SEM) was used to determine grain size and fracture mode of polycrystalline samples. A TESCAN 5130 MM scanning electron microscope and a ZEISS 1540 EsB Cross Beam were used to take SEM images from broken sections and thermally etched surfaces (polished surface was etched at 1350°C for 30 min (+600°C/h and -300°C/h). The mean grain size value and grain size distribution was estimated from the SEM images by the linear intercept method.

An orientation imaging (OIM) software program (TexSEM Lab.) interfaced to the SEM (LEO 438VP) was used to define the grain size and phase of the samples. The work was done in the Max Planck Institute for Metals Research.

1.6.3 ICP-OES

The cation concentration in polycrystalline and large grain samples was measured by ICP-OES (Spectro Ciros CCD, Spectro Analytical Instruments, Germany) in “Analytical Chemistry Lab” of the Max Planck Institute for Metals Research. The measurements were carried out on the solutions obtained by high pressure microwave assisted decomposition in HCl (37%) at 220°C for 1.5 h.

1.6.4 TG-hydration isobars

The concentration of protonic defects was determined from thermogravimetric analysis. Thermogravimetric data were recorded with a thermostated Sartorius 7014 balance using N $_2$ as a carrier gas. Samples were dried at 900°C under vacuum and then water uptake was measured in wet N $_2$ (pH $_2$ O = 20 mbar) during cooling from 800 to 50°C with an average rate of 10°C/h. Reversibility of water uptake was checked with heating the sample in wet gas up to

200 °C. Each TG curve was corrected by using a base line, which was obtained by running a similar measurement with a piece of quartz instead of the sample.

The TG data were fitted using **eq. (15)** to obtain the degree of hydration and the thermodynamic parameters of hydration^[121].

$$[\text{OH}_\text{O}^\bullet] = \frac{3Kp_{\text{H}_2\text{O}} - \sqrt{Kp_{\text{H}_2\text{O}}(9Kp_{\text{H}_2\text{O}} - 6Kp_{\text{H}_2\text{O}}S + Kp_{\text{H}_2\text{O}}S^2 + 24S - 4S^2)}}{Kp_{\text{H}_2\text{O}} - 4} \quad (15)$$

S is the effective dopant concentration which has been assumed as the nominal dopant concentration for each sample. $p_{\text{H}_2\text{O}}$ and K are water partial pressure and equilibrium constant of the hydration reaction ($\text{H}_2\text{O}_{(\text{g})} + \text{V}_\text{O}^{\bullet\bullet} + \text{O}_\text{O}^{\text{X}} \rightleftharpoons 2\text{OH}_\text{O}^\bullet$). Thermodynamic parameters were calculated using $RT\ln K = T\Delta S^\circ - \Delta H^\circ$.

1.6.5 XPS

The chemical composition of the PLD films was examined by X-ray Photoelectron Spectroscopy (XPS) on a Kratos, AXIS Ultra instrument equipped with a monochromatized Al K_α x-ray source. The X-ray source power was 150 W, and the pass energy of the detector was 20 eV. Data were acquired with an increment of 0.1 eV and averaged over 3 sweeps. The analysis area was 0.3 mm by 0.7 mm and the depth resolution (escape depth of photoelectrons) amounts to about 1-4 nm. The measurement was performed on the as-received as well as sputtered surface (Ar^+ , 4 kV, 2 min). Evaluation of spectrum was done using “VISION” processing software. The C 1s peak at 284.6 eV was used to calibrate the peak positions. Ba 3d, Zr 3d, Y 3d, C1s, O 1s, F 1s regions were taken for quantification. The measurements were performed in the “Interface Analysis Group” of the Max Planck Institute for Solid State Research.

1.6.6 BET

The surface area of calcined powders was measured by nitrogen adsorption-desorption using an AUTOSORB 1 (Quantachrome). The multipoint Brunauer, Emmett and Teller (BET) equation was used to calculate the specific surface area.

1.6.7 Density by geometry method

The bulk density of samples with regular shape was determined by measuring their weight and geometry. The theoretical density was calculated based on the nominal composition and the lattice parameters as obtained from XRD.

1.6.8 Raman spectroscopy

Raman spectra are taken with a Jobin Yvon LabRam V 010 single grating spectrometer, equipped with a double super Razor Edge filter and a Peltier cooled CCD camera. Spectra are taken in quasi-backscattering geometry using the linearly polarized 632.817 nm line of a He/Ne gas laser, with power less than 2 mW and filter D 0.3 focused to a 10 μm spot through a 50x microscope objective on the top surface of the sample. The resolution of the spectrometer (grating 1800 L/mm) is 1 wave number (cm^{-1}). The work was done in the “Spectroscopy Group” of the Max Planck Institute for Solid State Research.

1.6.9 Transmission electron microscopy

The structure as well as the local grain boundary composition of polycrystalline ceramics was studied by transmission electron microscopy (TEM) with spatially resolved energy dispersive analysis (EDXS) and electron energy loss spectroscopy (EELS).

TEM specimens were prepared in an automatic tripod polisher (Allied MultiPrep). A final ion polishing with low energy Ar ions (0.5 keV) was performed using a LINDA ion mill (TECHNOORG). The specimens were analyzed in a dedicated scanning TEM (STEM - VG HB_501UX, Vacuum Generator) by EDXS (Thermo Fischer Scientific, Noran SIX) and EELS (Gatan UHV Enfina). The STEM is equipped with a cold field emission gun and is operated at 100 kV. The composition of edge-on grain boundaries (i.e. GB plane parallel to the electron beam) and neighboring bulk area were measured by EDXS analysis on area of 2 nm by 3 nm. The width of the image contrast was assigned as the GB thickness. It was below 2 nm for the edge-on GBs. The bulk composition was collected from the center of the grains. To obtain a realistic picture of the grain boundary composition, EDXS analysis was performed on 15-20 grain boundaries. The wedge-shaped specimen (prepared by the tripod

method) offers a relatively long thin edge to find a sufficient number of grain boundaries parallel to the electron beam. It was always tried to choose a similar distance from the edge of the TEM specimen to avoid thickness variations. The thickness was measured using EELS. If I_0 is the integrated zero-loss intensity and I is the total integrated intensity in the energy loss spectrum, then the specimen thickness t is given in terms of the total inelastic mean free path λ by $t/\lambda = \ln(I/I_0)^{[122]}$. The measured t/λ was always below 0.5, which corresponds to specimen thickness of 80-100 nm in BaZrO_3 .

The EDXS spectra were quantified using Zr K line ($K\alpha$ -15.775 keV), Y L line ($L\alpha$ - 1.923 keV), Sc K line ($K\alpha$ - 4.090 keV) and Ba L line ($L\alpha$ - 32.194 keV). The cation ratios $[\text{Dopant}]/([\text{Dopant}]+[\text{Zr}])$ (for dopant segregation) and $[\text{Ba}]/([\text{Dopant}]+[\text{Zr}])$ (for barium deficiency) were calculated from the experimental X-ray intensity ratios using Cliff-Lorimer k-factors ($k_Y = 2.997$, $k_{\text{Sc}} = 0.994$, $k_{\text{Zr}} = 3.263$, $k_{\text{Ba}} = 1.978$) and the Cliff-Lormier equation^[123]:

$$\frac{C_A}{C_B} = k_{A/B} \frac{I_A}{I_B} \quad (16)$$

where C_i is the concentration of element i , I_i is the x-ray intensity from element i and k is the Cliff-Lorimer sensitivity factor.

In this work all the quantifications were done with the standardless method. Since the spatial resolution of the EDXS measurement is only slightly sensitive to the sample thickness in the range below 100 nm, the thickness of the sample was not taken into account in our quantifications.

For thin films, TEM specimens were prepared by the focused ion beam (FIB) method. TEM images and selected area electron diffraction (SAED) patterns were taken using a ZEISS 912 microscope at 120 kV (LaB_6 gun). The EDXS-line scan across the films was performed on a SESAM microscope at 200 kV (Field Emission gun). High resolution TEM images were obtained from a JEOL 4000 FX at 400 kV. The measurements were performed in the Stuttgart Center for Electron Microscopy (StEM).

1.6.10 AC-impedance spectroscopy

AC impedance spectroscopy allows one to resolve contributions from bulk, GB and electrode. It was used to study the electrical properties of polycrystalline samples as well as thin films.

Impedance spectra were usually obtained at frequencies between 10^{-1} and 10^6 Hz by applying an AC voltage of 0.1 V using a Novocontrol Alpha-A analyzer. The DC bias dependence of AC impedance spectra was investigated by applying a DC voltage in the range of 0.1-10 V superimposed to the applied AC voltage. The impedance spectra were fitted by equivalent circuits using the Z-View software (Scribner, Inc.).

The empirical equivalent electrical circuit developed by Bauerle^[124] consisting of RC elements for grain interior, grain boundary and electrode interface was used. The semicircles, in particular the GB contribution, in the measured complex plane plots are typically depressed. This non-ideal behavior originates from a distribution in the current density due to materials inhomogeneity^[125]. Therefore, the capacitors (C) in the equivalent circuit were replaced by so-called constant phase elements (Q). The capacitance was then calculated from $C = (R^{1-n}Q)^{1/n}$ ^[125], where n is the depression parameter.

In reality, depending on the samples electrical properties and measurement conditions, some of the mentioned elements were not visible in the measured frequency range. Typical impedance spectra are shown in **Fig. 7**. At 600°C, the bulk semicircle is not visible at frequencies lower than 10^6 Hz and the intercept on the real axis has been used to estimate the bulk resistivity. At lower temperatures, the bulk resistance as well as capacitance can be obtained, but the electrode semicircle usually appears at very low frequencies and a long term measurement would be necessary to extract the electrode data.

The so-called “Brick layer model”^[126, 127] (**Fig. 8**) was used to describe grain interior (bulk), grain boundary and electrode contributions. According to this model the highly resistive grain boundaries parallel to the current are negligible and grains, grain boundaries perpendicular to current and electrode interface result in three RQ circuits in series.

The resistances (R) and capacitances (C) obtained by fitting the impedance spectra can be analyzed using **eq. (17-19)**. With the assumption that $\epsilon_b = \epsilon_{GB}$, the capacitance ratio (C_b/C_{GB}) can be used instead of (δ_{GB}/d_g) to estimate the specific grain boundary conductivity ($\sigma_{GB,spec.}$) of polycrystalline samples.

$$R_1 = \frac{1}{\sigma_b} \times \frac{L}{A} \quad (17)$$

$$R_2 = n \left(\frac{1}{\sigma_{GB,spec.}} \right) \left(\frac{\delta_{GB}}{A} \right) = \left(\frac{L}{d_g + \delta_{GB}} \right) \left(\frac{1}{\sigma_{GB,spec.}} \right) \left(\frac{\delta_{GB}}{A} \right) = \left(\frac{1}{\sigma_{GB,spec.}} \right) \left(\frac{\delta_{GB}}{d_g} \right) \left(\frac{L}{A} \right) = \left(\frac{1}{\sigma_{GB}} \right) \left(\frac{L}{A} \right) \quad (18)$$

$$\epsilon_b = C_b \left(\frac{1}{\epsilon_0} \right) \left(\frac{L}{A} \right) \quad (19)$$

where δ_{GB} is the effective (electrical) grain boundary thickness, d_g is grain size, n is number of grain boundaries perpendicular to current and A is the area.

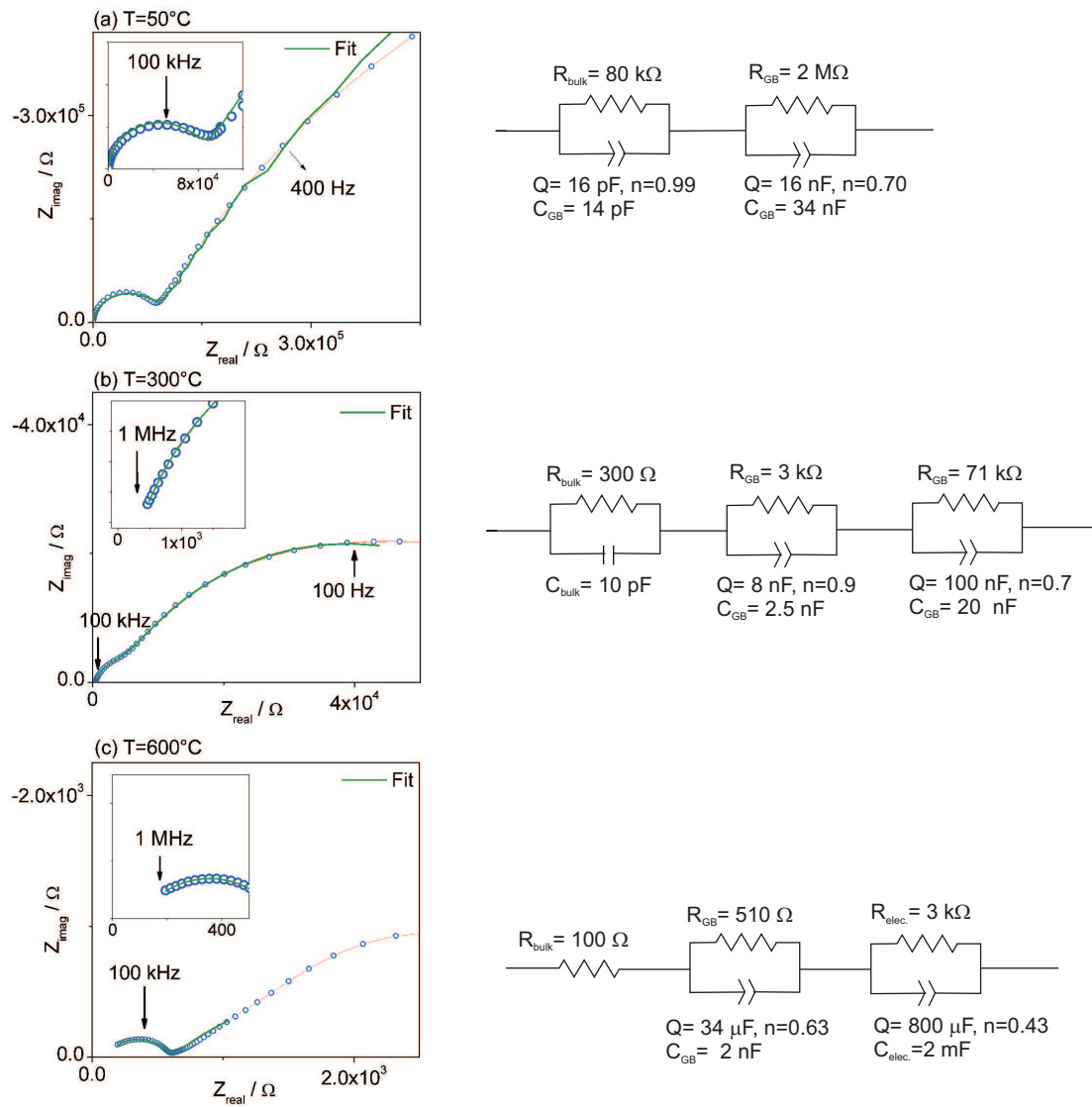


Figure 7 Typical impedance spectra (complex plane plot) and equivalent circuits of Y-doped BaZrO₃ at (a) 50°C, (b) 300°C and, (c) 600°C

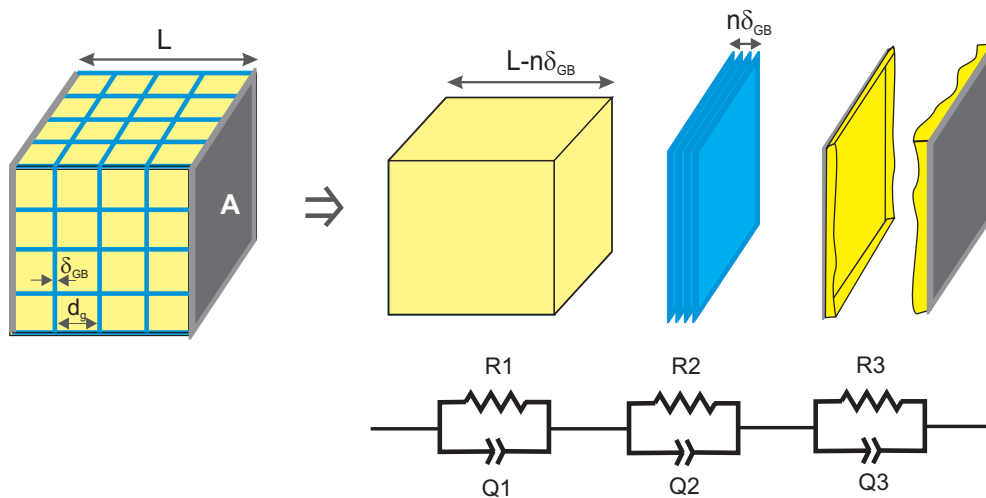


Figure 8 Brick layer model and typical equivalent circuit for polycrystalline materials

1.6.10.1 Conductivity of polycrystalline samples using macroscopic electrodes

A platinum layer (thickness ~ 400 nm) was sputtered (Edwards Auto 306) on both sides of the sample (area ~ 50 mm² and thickness ~ 1 mm) for macroscopic (conventional) conductivity measurements. The sample holder was a gas tight quartz cell in a tube furnace, electromagnetically shielded by a high-temperature resistant Cr-alloy foil. This cell was used in the temperature range of 50-800°C under dry and wet atmosphere (gas flow rate ~ 50 SCCM).

1.6.10.2 Conductivity of individual grain boundaries using microelectrodes

For applying microelectrodes on the large grained sample, a 200 nm Pt layer was sputtered on the polished surface and photolithography was used to pattern circular microelectrodes of 20 μ m diameter. The distance between two microelectrodes was 70 μ m. Electrical contact was established by needles of a Pt/Ir with a nominal tip radius of 2.5 μ m, which could be positioned accurately by micromanipulators (Karl Süss, Germany) under an optical microscope (Mitutoyo, Japan). The samples were placed in a heating stage (Linkam, UK) to control the sample temperature. Since purging wet gas during microcontact measurement is limited by the set-up, the sample was hydrated in advance and the measurement was performed under dry nitrogen.

1.6.10.3 Conductivity of thin films

The Pt electrode (~ 400 nm) was sputtered (Edwards Auto 306) on the thin films using a shadow mask which patterns two strips separated by a distance of 1 mm (**Fig. 9**). The conductivity measurement was done in the same cell as the polycrystalline samples. The conductivity was calculated using **eq. (17)** where $A = wt$.

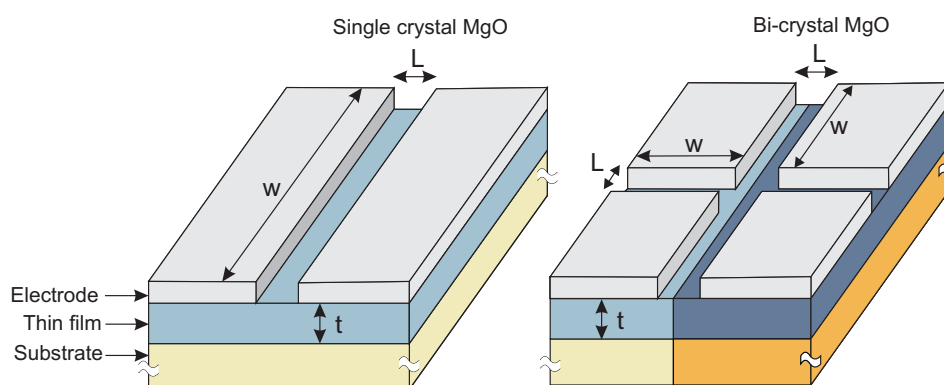


Figure 9 Electrode pattern on the thin films deposited on single- and bi- crystal MgO substrates

1.6.10.4 $p\text{H}_2\text{O}$ control

The humidified gas was produced by passing the gas flow through a water bubbler. The water partial pressure was controlled by the temperature of water (e.g. 20°C for 23 mbar).

For the dry atmospheres, the traces of water potentially present in nominally dry gases were condensed by passing the gas into a cold trap (dry ice).

1.6.10.5 $p\text{O}_2$ control

Pure oxygen, 1% O_2 in N_2 , and 100 ppm O_2 in N_2 were used for adjusting oxygen partial pressures of 1, 10^{-2} and 10^{-4} atm. A mixture of 1% CO in N_2 and pure CO_2 was used for lower oxygen partial pressures. Since this mixture needs equilibration, the temperature range is limited. Oxygen partial pressures of 10^{-18} atm down to 10^{-24} atm in the temperature range of 500 - 600°C were accessible. In the gas tight cells, pure N_2 yields a $p\text{O}_2$ of 10^{-4} - 10^{-5} atm, as recorded by a lambda sensor (Cambridge sensotec, Rapidox 2100).

In order to bring samples into the n-conducting regime, a zirconium metal layer (300-500 nm) was deposited on both sides of the samples (~ 0.7 mm thick) by evaporation. The sample sealed in a quartz tube under vacuum was heated up to 800°C for 48 hours leading to oxidation of the Zr metal and reduction of the sample. Considering the oxygen vacancy diffusion coefficient from conductivity of Y-BaZrO₃ at 800°C under dry atmosphere, the annealing time is sufficient to achieve a homogeneous defect distribution in the sample with a thickness of 0.7 mm. After annealing, the oxide layer was removed from the surface. According to the equilibrium of zirconium oxidation ($\text{Zr} + \text{O}_2 \rightleftharpoons \text{ZrO}_2$; $\Delta G^\circ_{800^\circ\text{C}} = - 875$ kJ/mol), the oxygen partial pressure at the annealing temperature is about 10^{-42} atm. Therefore, reducing Y-doped BaZrO₃ using the metallic layer of Zr can be regarded to be equivalent to exposing the sample to extremely low oxygen partial pressures ($\geq 10^{-42}$ atm). While the last Zr particle is in equilibrium with ZrO₂, the oxygen partial pressure is 10^{-42} atm and when all the Zr is used up the partial pressure will be higher than this value. In addition, using Zr layers of different thickness allowed producing different electron concentrations assumed as different oxygen partial pressures.

Chapter 3

Results and discussion

1.7 Structure and chemical composition of GB and its effect on σ_{GB}

1.7.1 Sample characterization (polycrystalline)

1.7.1.1 Conventionally sintered samples (CS)

The x-ray diffraction patterns in **Fig. 10-a** confirm the formation of single phase BaZrO₃ in the conventionally sintered (CS) pellets ($\rho \leq 92\% \rho_{\text{theory}}$). The XRD pattern of 15 at.% Y-BaZrO₃ was fitted with a tetragonal phase and the unit cell size in Fig. 9-b is the pseudo-cubic lattice constant ($V^{1/3}$). The tetragonal phase for highly doped BaZrO₃ has already been reported^[44]. The unit cell size of Y-doped samples, due to the larger ionic radii of Y⁺³ (0.90 Å) compared to Zr⁺⁴ (0.72 Å), increases by the amount of dopant. The linear increase of unit cell size of sintered pellets with the amount of Y dopant is shown in **Fig. 10-b**. The data obtained for the samples are comparable with the reported lattice parameters^[44, 128].

Fig.11 compares the bulk and GB conductivity of CS-YBZ samples with different dopant concentration. Both bulk and GB conductivities increase with dopant concentration and at the same time the activation energy of conductivity slightly decreases with increasing dopant concentration. Some previous studies showed that bulk conductivity, as well as GB conductivity, of Y-doped BaZrO₃ decreases by increasing dopant concentration, mostly due to higher proton-dopant association or loss of BaO^[129], this effect apparently is more significant for samples containing more than 20 at.% dopant. In the absence of such effects, a higher dopant concentration leads to a higher bulk and GB conductivity.

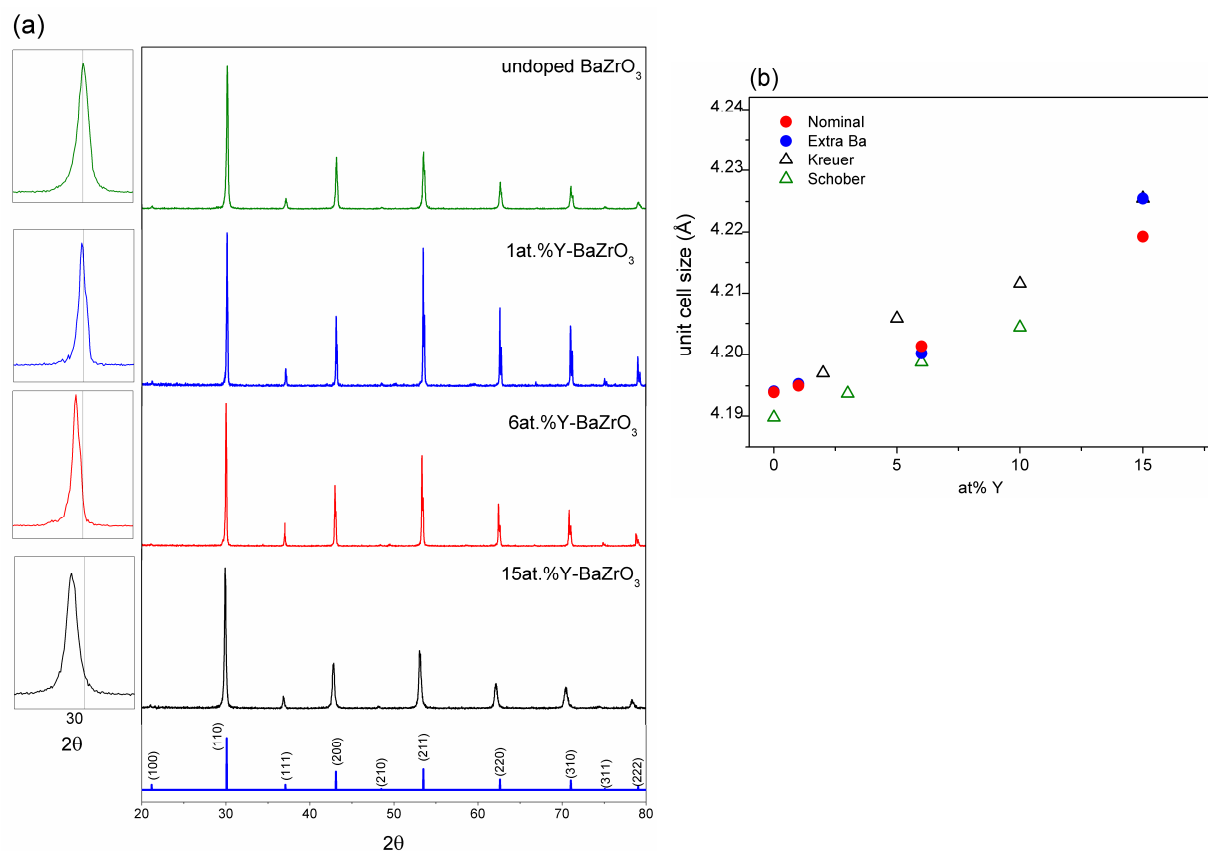


Figure 10 (a) X-ray diffraction pattern and (b) unit cell size of conventionally sintered pellets of undoped and Y-doped BaZrO₃ in comparison with Schober^[128] and Kreuer^[44] data. The undoped sample shows a relatively broad peak and a larger strain was obtained from pattern deconvolution of the sample.

The Y dopant content of CS samples measured by ICP-OES (**Table 2**) is in relatively good agreement with the nominal composition. The lower barium content is expected due to barium loss during sintering. To compensate a part of Ba loss, CS samples were also sintered from calcined powder with 1 wt% extra barium in the starting composition. In addition to the chemical analysis, the amount of “active dopant” can be determined from water uptake. Hydration is accompanied by weight increase of sample ($1 \text{ mol H}_2\text{O} = 2[\text{OH}^\bullet]$), therefore, the amount of water uptake is representative of available oxygen vacancies, i.e. the concentration of “active dopant”. The difference between nominal and measured amount of dopant can be due to BaO loss. **Fig. 12** compares the hydration behavior of CS-6YBZ with and without 1 at.% extra barium. The extracted standard hydration enthalpies and entropies from the water uptake data are in good agreement with previous results^[128]. The two samples underwent about 2-3% of barium loss and 1 at.% extra Ba apparently compensated a part of

barium loss (~ 1 at.%). The effect of extra barium on the electrical conductivity of sample is not unambiguous. The addition of extra barium to 6YBZ significantly enhanced σ_b and σ_{GB} , whereas the conductivity of 15YBZ did not change when using extra Ba (**Fig. 13-a,b**). It seems that it is not easy to control the composition of acceptor-doped BaZrO₃ with conventional sintering method. Therefore, ‘‘Spark Plasma Sintering’’ was used to obtain sintered pellets with a more reliable composition and higher bulk density.

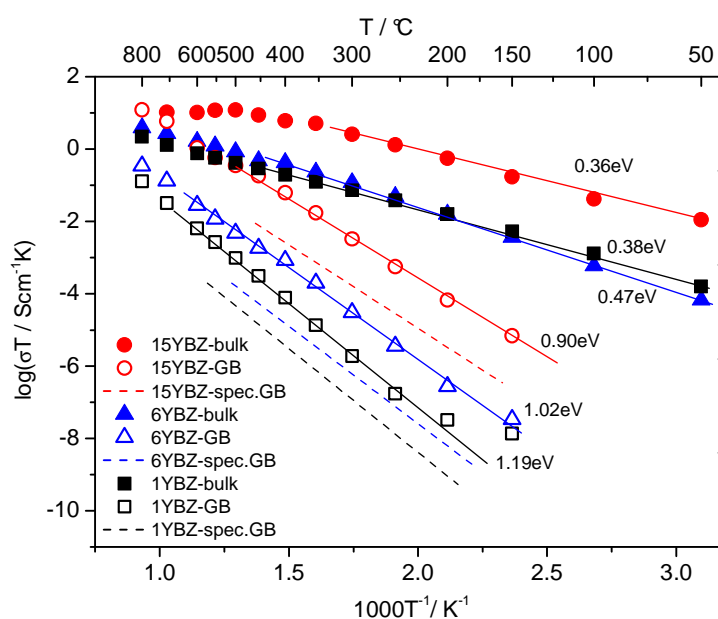


Figure 11 Arrhenius plots of conventionally sintered pellets of 1 at.% (1YBZ), 6 at.% (6YBZ) and 15 at.% (15YBZ) in wet N₂ (pH₂O = 20 mbar)

Table 2 Composition of conventionally sintered samples with different dopant concentration

Nominal composition	Composition measured by ICP-OES			
	Ba (wt%)	Zr (wt%)	Y (wt%)	
Ba(Zr _{0.94} Y _{0.06})O _{3-δ}	48.7±0.5	31.0±0.3	1.93±0.05	Ba _{0.98} (Zr _{0.94} Y _{0.06})O _{3-δ}
Ba _{1.01} (Zr _{0.94} Y _{0.06})O _{3-δ}	48.5±0.5	30.1±0.3	1.92±0.05	Ba _{1.00} (Zr _{0.94} Y _{0.06})O _{3-δ}

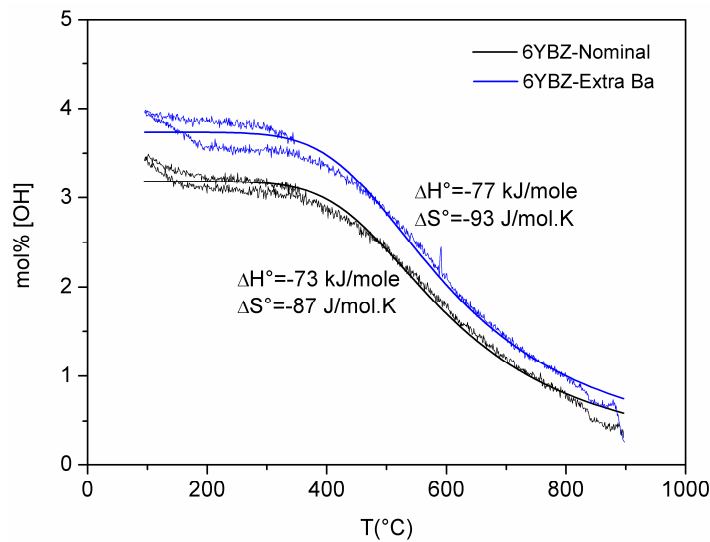


Figure 12 Water uptake of 6YBZ-Nominal and 6YBZ-extra Ba and thermodynamic information obtained from fit according to eq. (15)

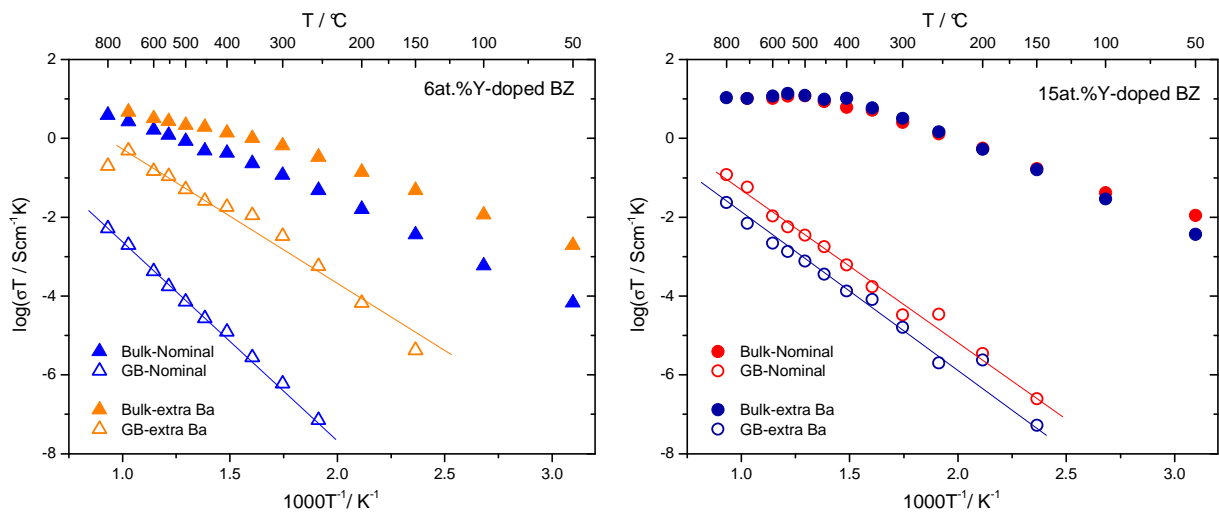


Figure 13 Arrhenius plots of (a) 6YBZ and (b) 15YBZ sintered from nominal composition and 1wt% extra barium calcined powder in wet N_2 ($p_{H_2O} = 20$ mbar)

1.7.1.2 Spark Plasma Sintered samples (SPS)

X-ray diffraction patterns of as-prepared SPS and additionally annealed (1700°C/20h) SPS samples are shown in **Fig. 14**. According to XRD, the SPS samples are single phase. The unit cell size of the annealed sample is comparable to the as-prepared sample. The unit cell of the

scandium doped sample, due to the small size mismatch between Sc^{+3} (0.75 Å)^[130] and Zr^{+4} (0.72 Å)^[130], is similar to that of undoped BaZrO_3 .

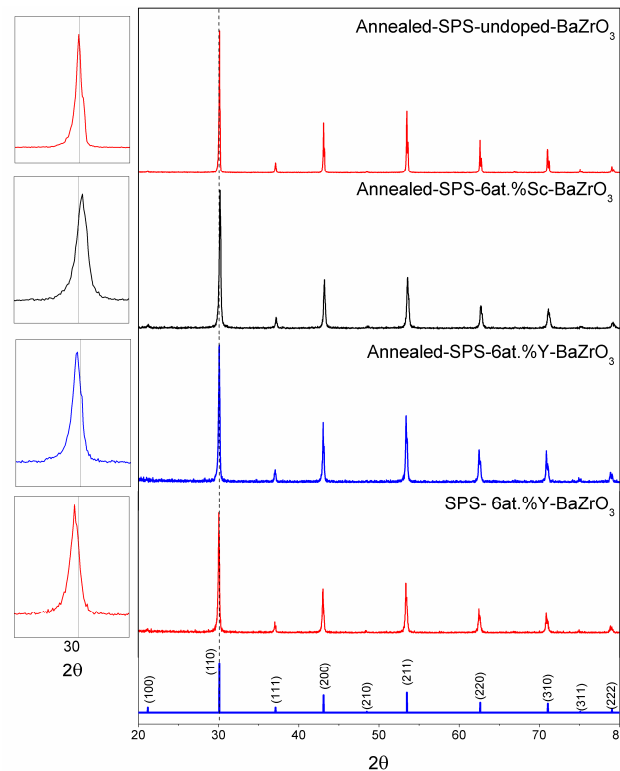


Figure 14 X-ray diffraction pattern of as-prepared (a) and annealed (b) SPS-6 at.%Y-doped BaZrO_3 , annealed SPS-6 at.%Sc-doped BaZrO_3 (c) and undoped BaZrO_3 .

SPS offered the possibility of a short sintering time (heating rate = 100°C/min, holding time = 5 min, cooling rate (1600°C-1000°C) \approx 400°C/min and cooling rate (1000°C-400°C) \approx 240°C/min) which decreases the amount of barium loss at high temperatures (> 1200°C). Nevertheless, a certain amount of barium loss at such a high sintering temperature is inevitable. Water uptake of conventionally sintered and as-prepared SPS samples, obtained by thermal gravimetric analysis (TG), are compared in **Fig. 15**. As expected, the barium loss for the SPS sample is less than for conventionally sintered samples. In spite of that, the bulk conductivity of the SPS sample with a lower barium loss is quite comparable (in log scale) to the conventionally sintered samples (**Fig. 16**). The main difference between two methods was observed in their fracture mode. As shown in **Fig. 17**, the SPS sample with transgranular broken section exhibits stronger cohesion at the grain boundaries in comparison with the conventionally sintered sample with intergranular fracture mode.

SEM images of thermally etched surface of as-prepared and annealed Y- and Sc-doped BaZrO_3 are shown in **Fig. 18**. The as-prepared SPS samples do not show a significant grain growth after annealing at high temperature (**Fig. 19**).

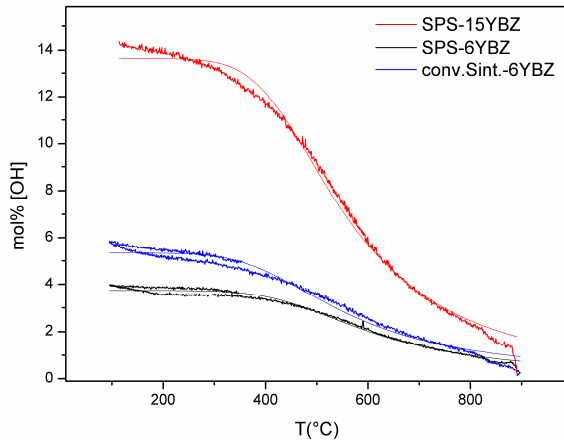


Figure 15 Hydration isobars of conventionally and

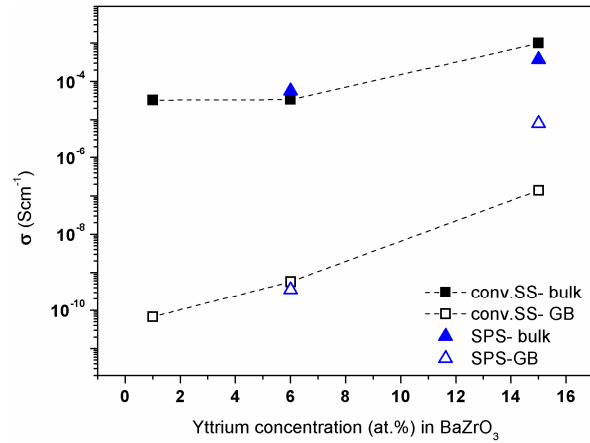


Figure 16 Bulk and GB conductivity of SPS and conventionally sintered samples with different dopant concentrations

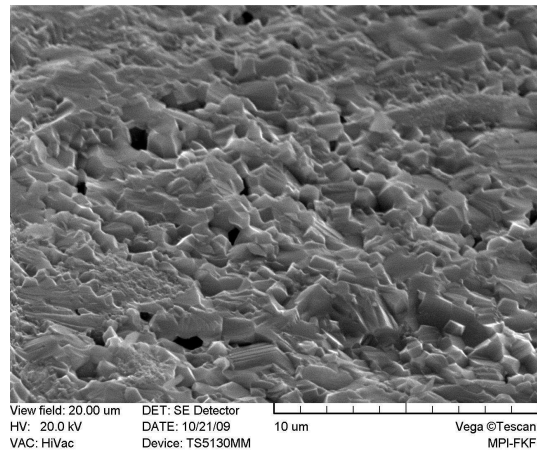
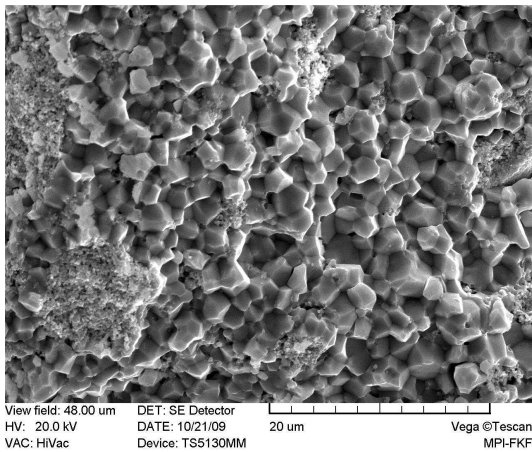


Figure 17 SEM images from broken section of conventionally sintered (left) and SPS (right) samples; the fracture mode has changed from intergranular (left) to transgranular (right).

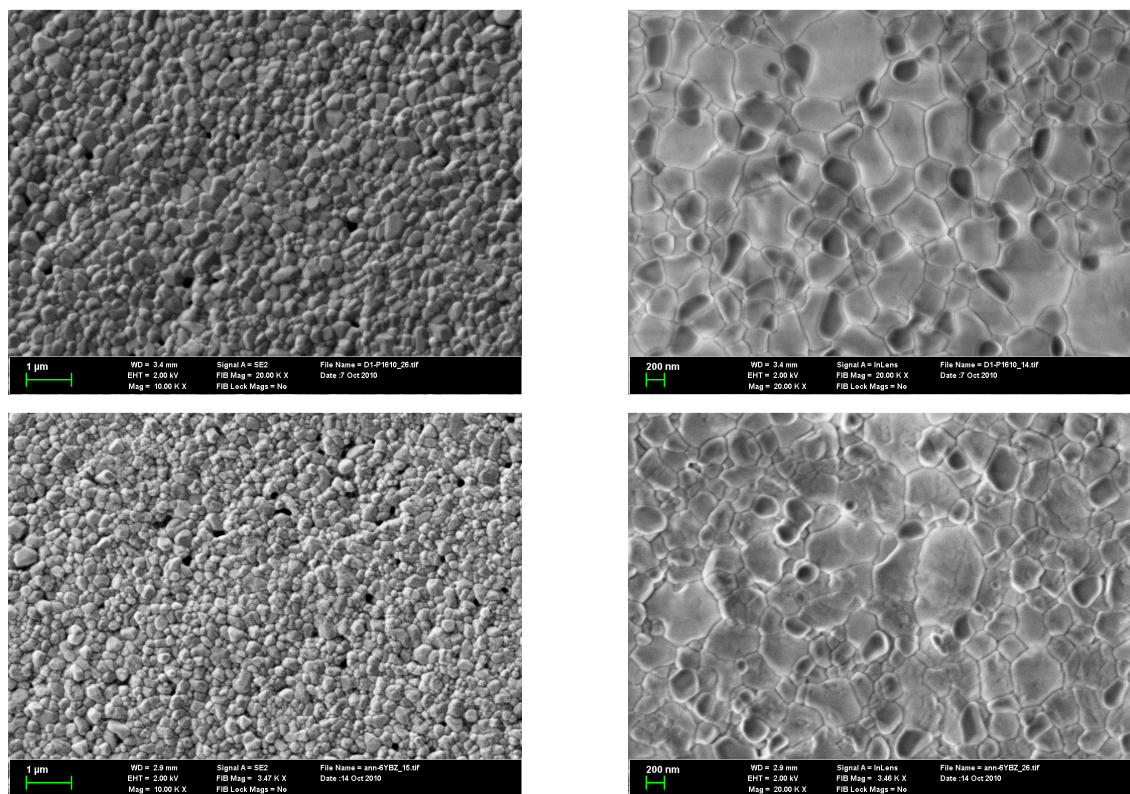


Figure 18 SEM image of as-prepared SPS (top) and annealed SPS (bottom) 6YBZ

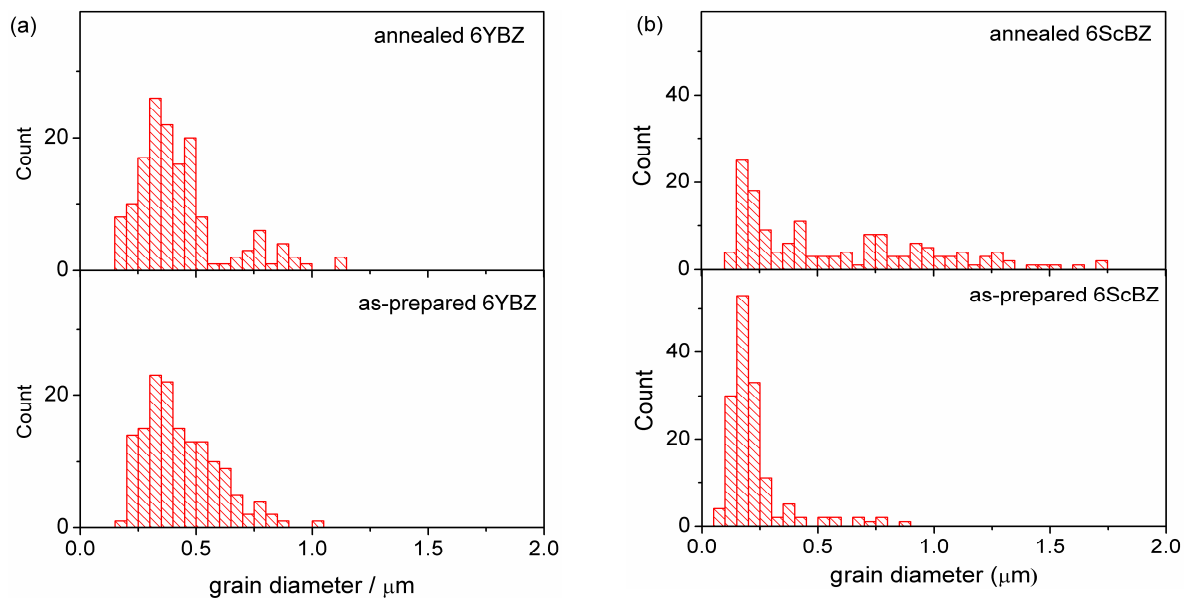


Figure 19 Grain size distribution of as-prepared SPS and annealed SPS (a) 6YBZ and (b) 6ScBZ obtained from SEM images

1.7.2 Grain boundary hydration behavior

The enhanced conductivity of YBZ in wet conditions is due to the formation of highly mobile protonic defects in the structure. Though, GB could behave differently upon hydration, and the low GB conductivity in wet condition might arise from low proton concentration or low proton mobility in the GB region. **Fig. 20** compares the bulk and GB conductivity of SPS-6YBZ in dry N_2 ($pO_2 = 10^{-4}$ atm) and wet N_2 ($pO_2 = 10^{-4}$ atm, $pH_2O = 0.02$ atm). The σ_{GB} enhancement is comparable to σ_b enhancement (~ 1000 times at $200^\circ C$). In addition, the hydration of a dried sample after exposing it to wet atmosphere, does not show any significant difference between bulk and GB behavior, at least in the first 100 hours at $500^\circ C$ (**Fig. 21**). Conclusively, the higher GB resistivity compared to the bulk is not due to a lower contribution of protonic conductivity or delayed hydration.

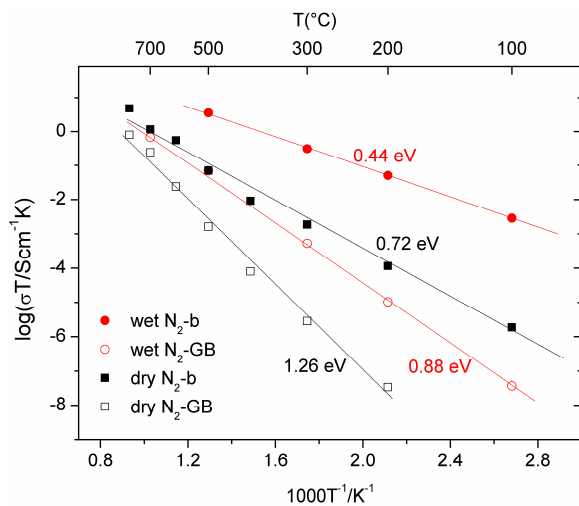


Figure 20 Arrhenius plots of SPS-6YBZ in nominally dry and wet nitrogen.

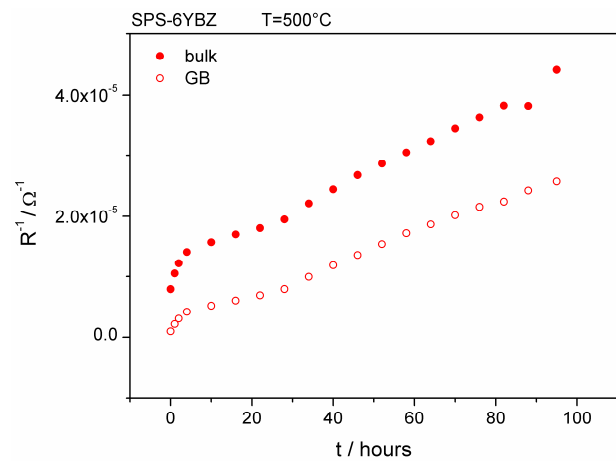


Figure 21 Relaxation behavior of bulk and grain boundary after exposing SPS-6YBZ to wet N_2 ($pH_2O = 20$ mbar); sample was previously dried under vacuum at $900^\circ C$.

The equilibrium concentration of charge carriers in Y-doped $BaZrO_3$ as a function of water and oxygen partial pressure^[131, 132] was used to draw a comprehensive picture of hydration in the GB region. On the basis of the conduction parameters determined in ref.^[132], the bulk oxygen vacancy, hole and proton conductivities can be obtained by the following Arrhenius equations in 20 %Y-doped $BaZrO_3$:

$$\sigma_{\text{H}^+} T = 10^{0.5 \log(\text{pH}_2\text{O} / \text{atm}) + 3.45} \exp(-0.38 \text{eV} / kT) \text{ Scm}^{-1} \text{K} \quad (20)$$

$$\sigma_{\text{V}_\text{O}^{\bullet\bullet}} T = 10^{3.69} \exp(-0.75 \text{eV} / kT) \text{ Scm}^{-1} \text{K} \quad (21)$$

$$\sigma_{\text{h}\cdot} T = 10^{0.25 \log(\text{pO}_2 / \text{atm}) + 5.32} \exp(-0.73 \text{eV} / kT) \text{ Scm}^{-1} \text{K} \quad (22)$$

The hole, oxygen vacancy, proton and total conductivities of Y-doped BaZrO₃ using these equations are plotted in **Fig. 22**. The E_a obtained from the defect chemical model^[132] are in a good agreement with our measurements on SPS-6YBZ in dry and wet conditions.

One can clearly observe that under dry conditions the dominant conduction mechanism is hole conductivity and not oxygen ion conductivity. In wet conditions and the same oxygen partial pressure, the proton conductivity is expectedly dominant. Accordingly, Y-doped BaZrO₃ under dry conditions exhibits hole conduction ($z = 1$) and in wet condition is a proton conductor ($z = 1$). On the basis of this information, schematic pictures of charge carriers under different conditions are suggested in **Fig. 23** for the case of GB properties determined by space charge effects. The potential barrier and width of GB under dry and wet conditions are comparable ($\Phi_0 = 0.5 \text{V}$ and $\lambda^* = 2.5 \text{ nm}$; calculated from conductivity data using Mott-Schottky model).

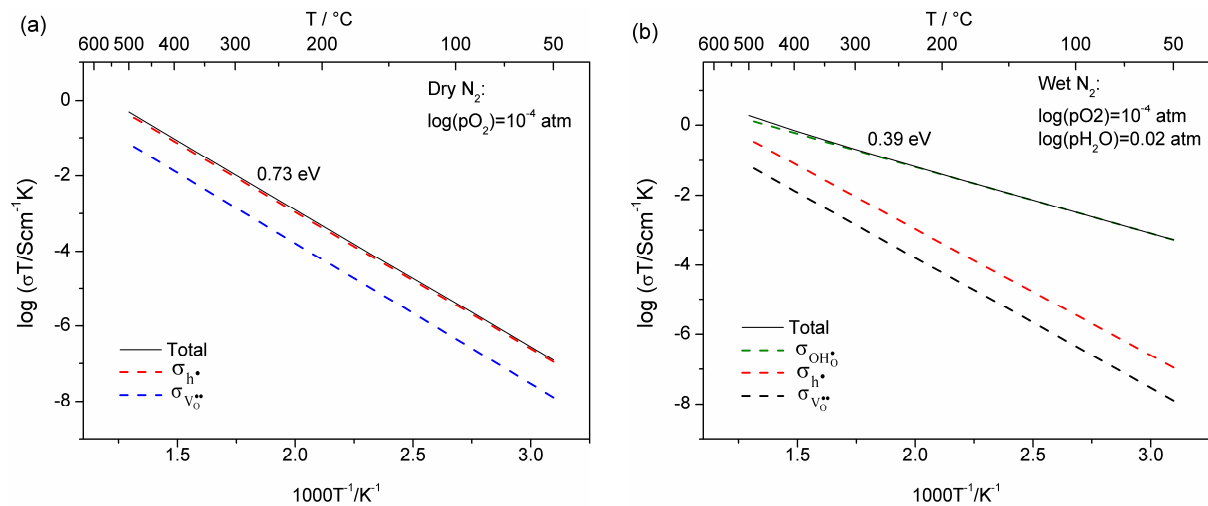


Figure 22 The calculated conductivities of different charge carries in (a) dry and (b) wet conditions using ref. [132]

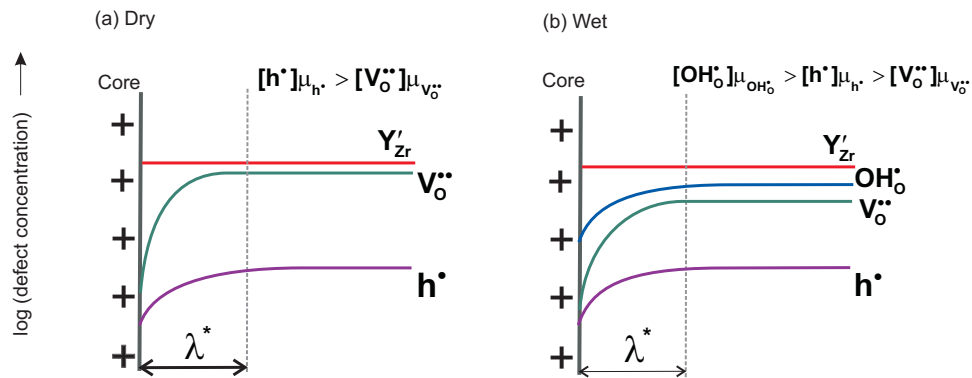


Figure 23 The schematic picture of charge carrier concentration in (a) dry and (b) wet conditions, for partial hydration, even if $[V_{O}^{\bullet\bullet}] \geq [OH_o^{\bullet\bullet}]$, the higher proton mobility leads to $\sigma_{OH_o^{\bullet\bullet}} > \sigma_{V_{O}^{\bullet\bullet}}$.

1.7.3 Secondary/amorphous phase at GB

No secondary phase inside the grains, along the GBs and at triple junctions of as-prepared and annealed Y- and Sc-doped BaZrO₃ was recognized. The bright-field TEM images of as-prepared and annealed 6 at.% Y-BaZrO₃ are shown in **Fig. 24**.

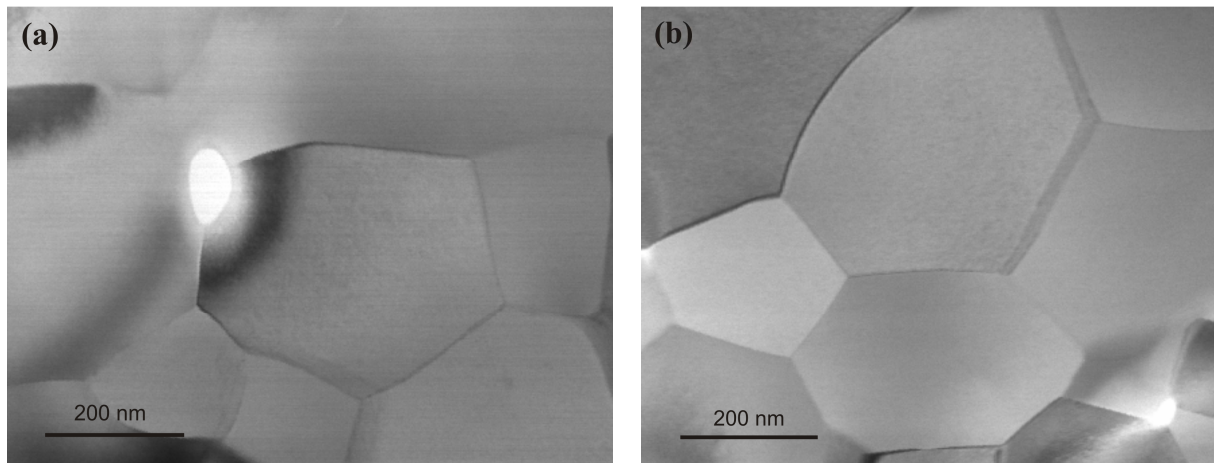


Figure 24 Bright-field images of (a) as-prepared and, (b) annealed 6 at.% Y-BaZrO₃ (the bright area in the images are holes)

1.7.4 Annealing effect

Fig. 25-a,b shows the impedance spectra and Arrhenius plots of as-prepared and annealed 6 at.% Y-doped BaZrO₃ under wet atmosphere in the temperature range of 100-700°C. After applying a high-temperature annealing (1700°C for 20 hours), the bulk conductivity is essentially unchanged. However, grain boundary conductivity increases significantly in the annealed sample (3 orders of magnitude at 200°C) and exhibits a lower activation energy ($E_a = 0.71$ eV) compared to the GB of the as prepared sample ($E_a = 1.04$ eV).

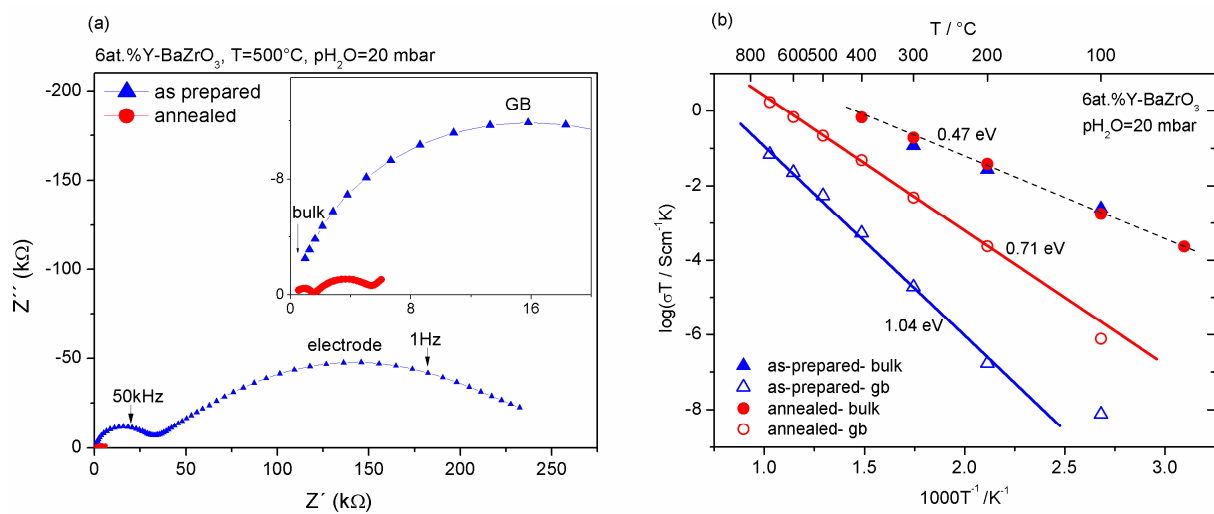


Figure 25 (a) AC impedance spectra and (b) Arrhenius plots of as-prepared and annealed SPS-6YBZ in wet atmosphere ($p_{H_2O} = 20$ mbar) at 500°C

As shown in **Fig. 26**, a GB conductivity enhancement was not observed after annealing at lower temperatures (1550°C), which can be due to low mobility of cations at lower temperatures. On the other hand, longer annealing at 1700°C (60 hours) yields a lower bulk conductivity, and also lower GB conductivity. This can be due to barium loss during the longer annealing step. ICP-OES results in **Table 3** shows that SPS samples after annealing for 60 hours contain less barium than the as-prepared and 20 hours annealed sample. 15 at.% Y-doped BaZrO₃ shows a similar effect after annealing at 1700°C for 20 hours (**Fig. 27**), although the σ_{GB} enhancement is less pronounced. This is probably related to the higher Y concentration at the GB of as-prepared SPS-15YBZ. The same behavior was also observed for the as-prepared and annealed scandium doped BaZrO₃ (**Fig. 28-a,b**). The calculated potential barrier (**eq. (14)**) and grain boundary thickness (**eq. (12)**) are smaller in the annealed samples (**Table 4**).

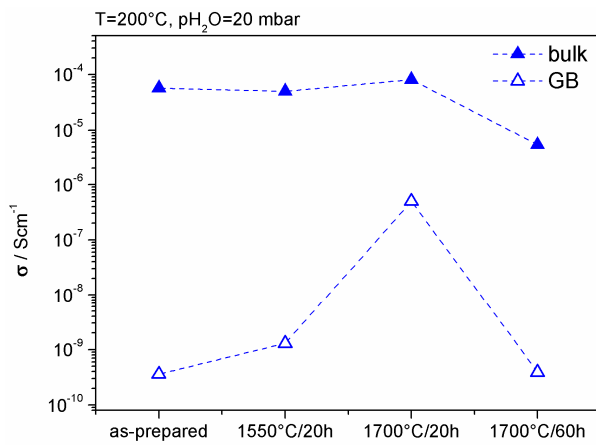


Figure 26 Bulk and grain boundary conductivity of 6 at.% Y-doped BaZrO_3 under different annealing conditions

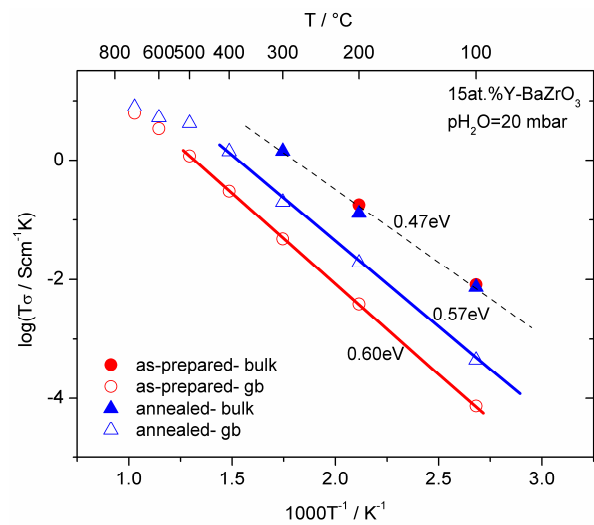


Figure 27 Arrhenius plots of as-prepared and annealed 15 at.% Y- BaZrO_3 in wet atmosphere

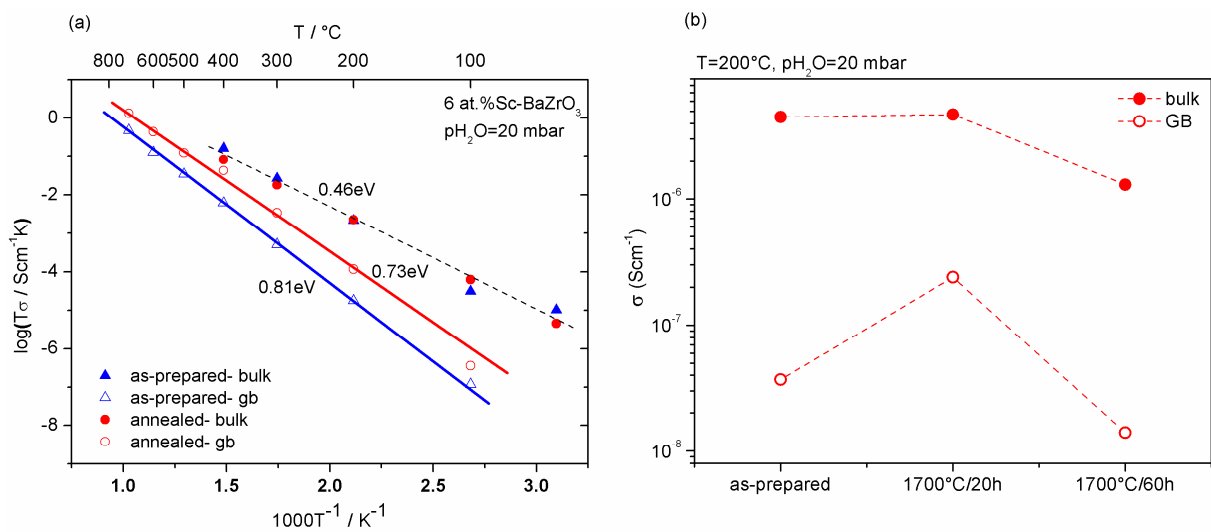


Figure 28 (a) Arrhenius plots of as-prepared and annealed SPS-6 at.% Sc-doped BaZrO_3 under wet atmosphere ($\text{pH}_2\text{O} = 20$ mbar) and, (b) bulk and grain boundary conductivity at 200°C for different annealing conditions

Table 3 Composition of SPS samples with different additional annealing

Nominal composition	Composition measured by ICP-OES			
	Ba (wt%)	Zr (wt%)	Y (wt%)	
$\text{Ba}(\text{Zr}_{0.94}\text{Y}_{0.06})\text{O}_{3-\delta}$				
as-prepared-SPS	49.0 ± 0.7	30.4 ± 0.5	1.91 ± 0.04	$\text{Ba}_{1.01}(\text{Zr}_{0.94}\text{Y}_{0.06})\text{O}_{3-\delta}$
annealed ($1700^\circ\text{C}/20\text{h}$)	48.8 ± 0.7	30.6 ± 0.5	1.90 ± 0.04	$\text{Ba}_{1.00}(\text{Zr}_{0.94}\text{Y}_{0.06})\text{O}_{3-\delta}$
annealed ($1700^\circ\text{C}/60\text{h}$)	48.3 ± 0.7	30.8 ± 0.5	1.90 ± 0.04	$\text{Ba}_{0.98}(\text{Zr}_{0.94}\text{Y}_{0.06})\text{O}_{3-\delta}$

Table 4 Bulk and GB potential barrier and GB thickness of as-prepared and annealed samples at 200°C

Sample		Φ_0 (V)	$\delta_{GB} = 2\lambda^*$ (nm)
6 at.% Y-doped BaZrO ₃	as-prepared	0.68	5.45
	annealed	0.49	4.62
15 at.% Y-doped BaZrO ₃	as-prepared	0.45	2.80
	annealed	0.40	2.64
6 at.% Sc-doped BaZrO ₃	as-prepared	0.52	4.76
	annealed	0.41	4.23

The GB potential and thickness are calculated assuming Mott-Schottky situation using **eq. (14)** and **eq. (12)**, respectively.

Since the high temperature annealing did not lead to a significant grain growth (**Fig. 19**), the enhanced GB conductivity refers to an enhanced specific GB conductivity. At such a high temperature and relatively long annealing, cations become mobile and even a large cation as Y can diffuse tens of nanometers in a perovskite structure. The cation diffusion coefficient can be estimated from the results obtained for SrTiO₃ and BaTiO₃ single crystal^[133, 134] (**Fig. 29**).

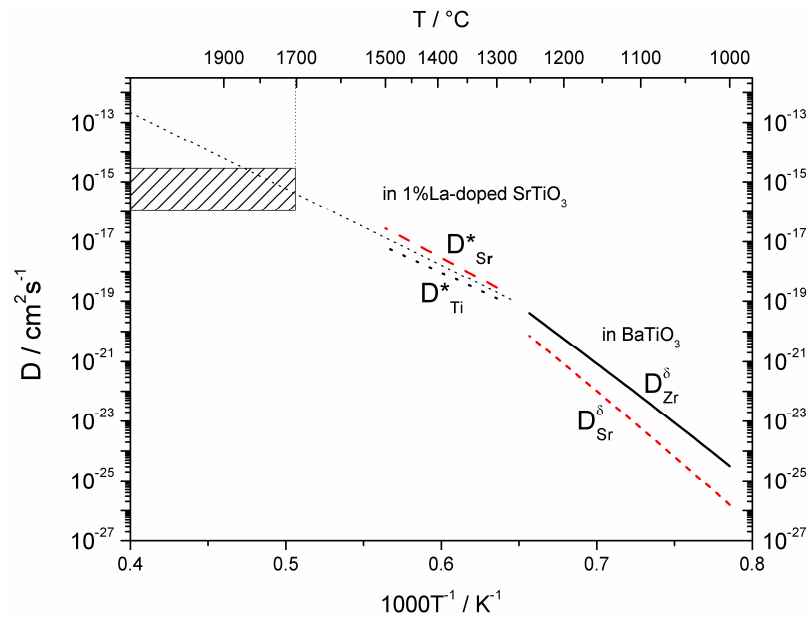


Figure 29 Chemical diffusion coefficients of strontium and zirconium in BaTiO₃ single crystal^[133, 134], tracer diffusion of titanium and zirconium in 1 at.% La-doped SrTiO₃ single crystal^[133] (measured by secondary ion mass spectroscopy)

Then cations with diffusivity of about 10^{-16} - 10^{-15} cm^2/s at 1700°C diffuse 30-80 nm in 20 hours and this length is sufficient for dopant cations to move from the grains to the GB region.

Thus, strictly speaking the Mott-Schottky model (constant dopant concentration) may not be applicable for the annealed samples. A more detailed discussion of this is given in **section 3.1.5.1**.

1.7.5 Dopant segregation

In order to understand how the electrical properties of grain boundaries is influenced by dopant segregation, the grain boundary composition of as-prepared and annealed SPS samples of Y- and Sc-doped BaZrO₃ exhibiting significantly different grain boundary resistivities was studied.

Fig. 30 shows typical EDXS spectra taken from an area of 2×3 nm at various GBs and within neighboring grains in the annealed 6YBZ sample. Dopant distribution between core and space charge zone will be discussed in **section 3.1.5.1**. In most of the measurements, the Y intensity at GB is clearly larger than the Y intensity in bulk. **Fig. 31** summarizes the EDXS measurements on 15-20 grain boundaries of as-prepared and annealed Y-doped samples. In each graph, the solid line shows the average concentration and the shaded box is the standard error of the mean value ($SE = SD/n^{1/2}$ where SD is the standard deviation and n is number of measurements). From the $[Y]/([Y]+[Zr])$ ratio, it is clear that in both samples, as-prepared as well as annealed, dopant cations segregate to the grain boundary region. But the amount of segregation is much more pronounced at the GB of the annealed sample, which has a much higher GB conductivity. The $[Ba]/([Y]+[Zr])$ ratio as representative of barium deficiency does not change significantly from GB to bulk.

It should be mentioned that the amount of dopant in the bulk (measured by EDXS-TEM) is lower than the nominal and actual (ICP-OES) composition. This could be due to some inhomogeneity in the sample prepared by SPS method and/or correction needed for the EDXS quantification (standard sample with a known composition). Also, the $[Ba]/([Y]+[Zr])$ ratio is only ~ 0.9, but again due to the lack of a standard sample, one should not directly conclude that 10% of barium is lost.

Fig. 32 and **Fig. 33** show the respective EDXS-TEM measurements on Sc-doped BaZrO₃. The Sc-doped samples also exhibit a larger amount of dopant cations at the GB of the annealed sample (with lower GB resistivity). The barium content at the GB is slightly lower than in the bulk, but with a high uncertainty due to the large error bars (**Fig. 33-d**).

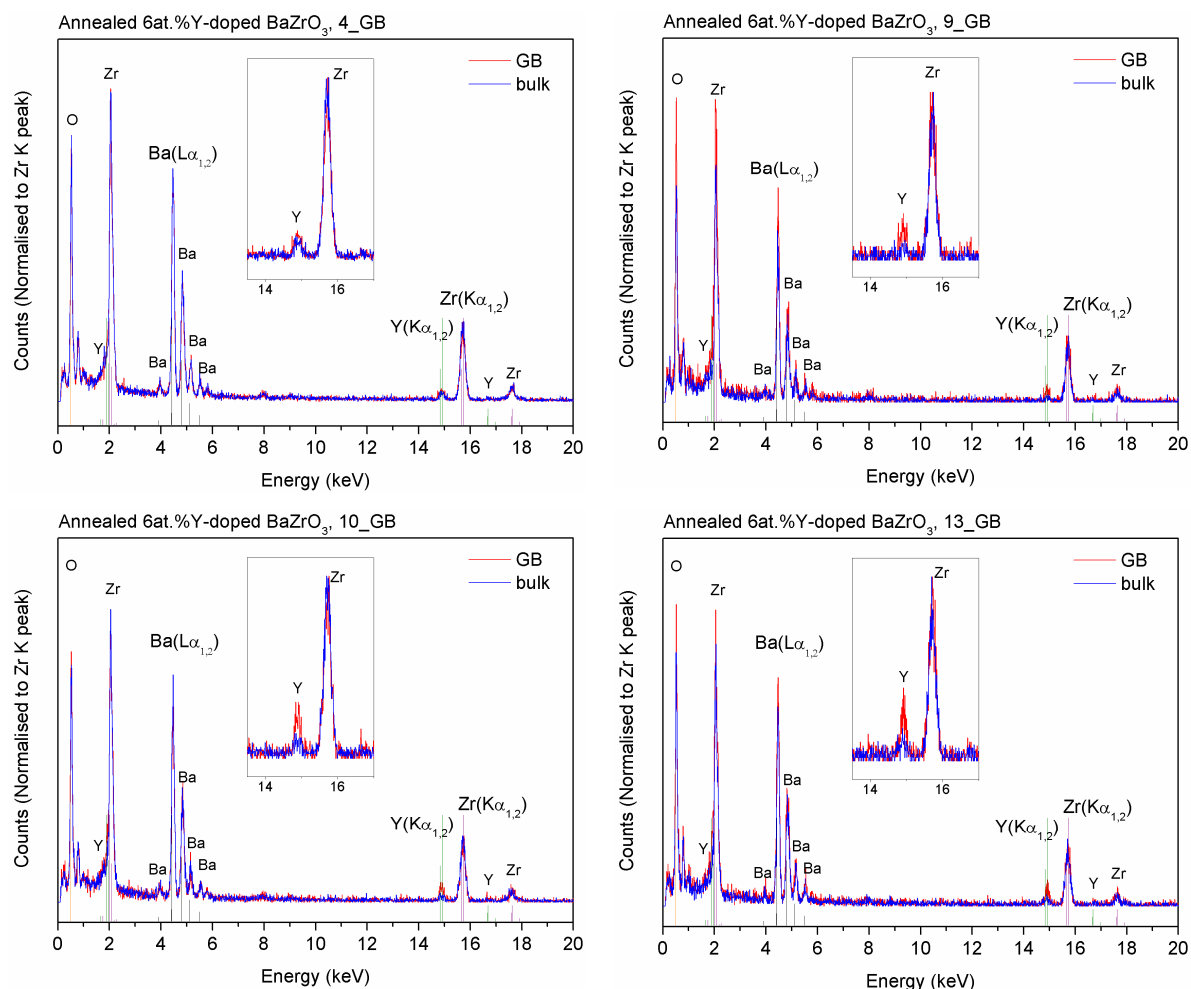


Figure 30 EDXS-TEM spectra from four different GBs of annealed SPS-6 at.% Y-doped BaZrO₃ (1700°C/20h)

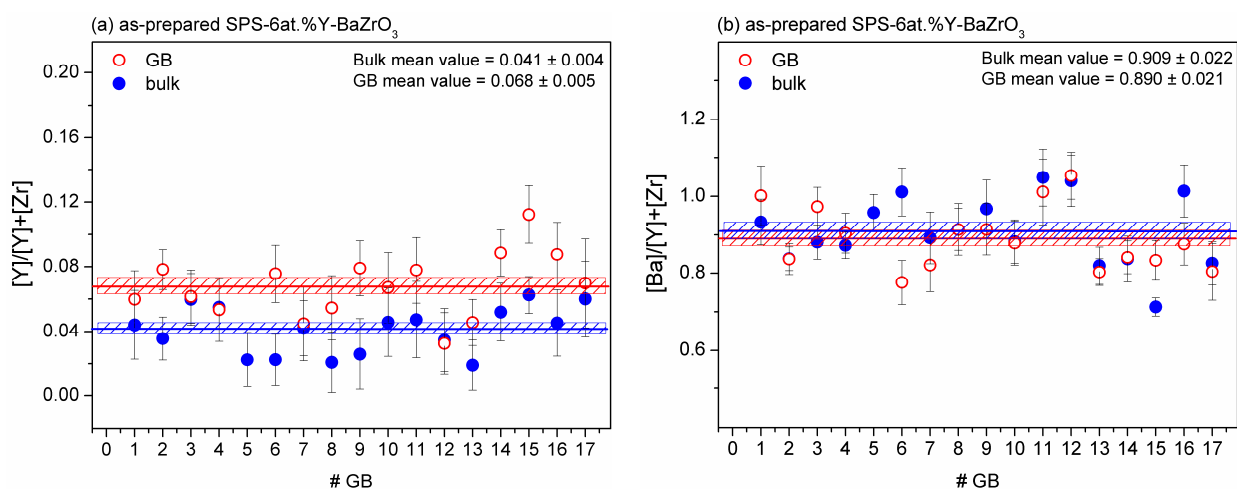


Figure 31 Y substitution and Ba deficiency of GB region compared to the bulk of as-prepared (a,b) and annealed (c,d) 6 at.% Y-doped BaZrO₃ (next page)

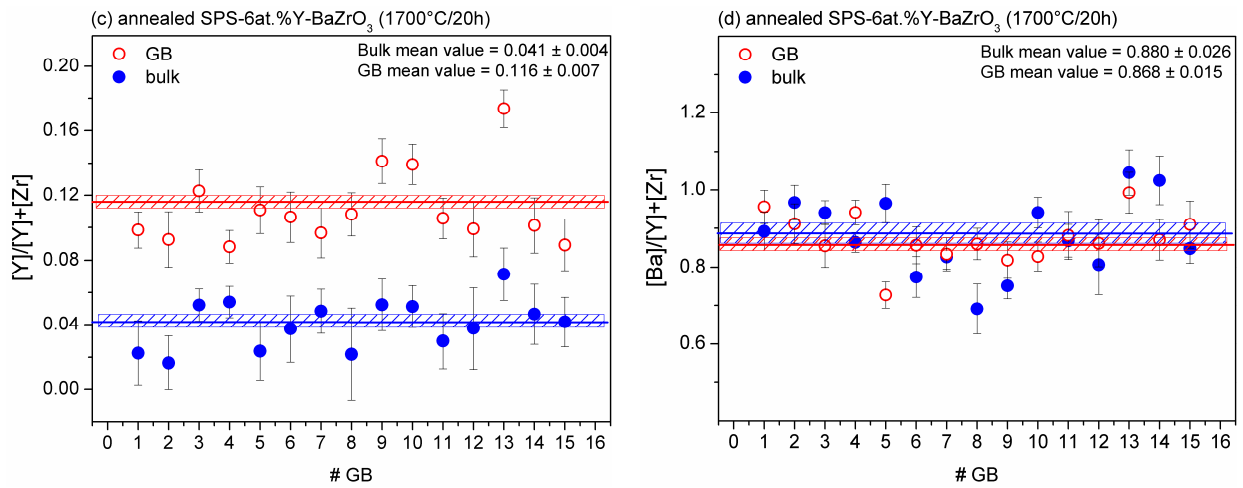
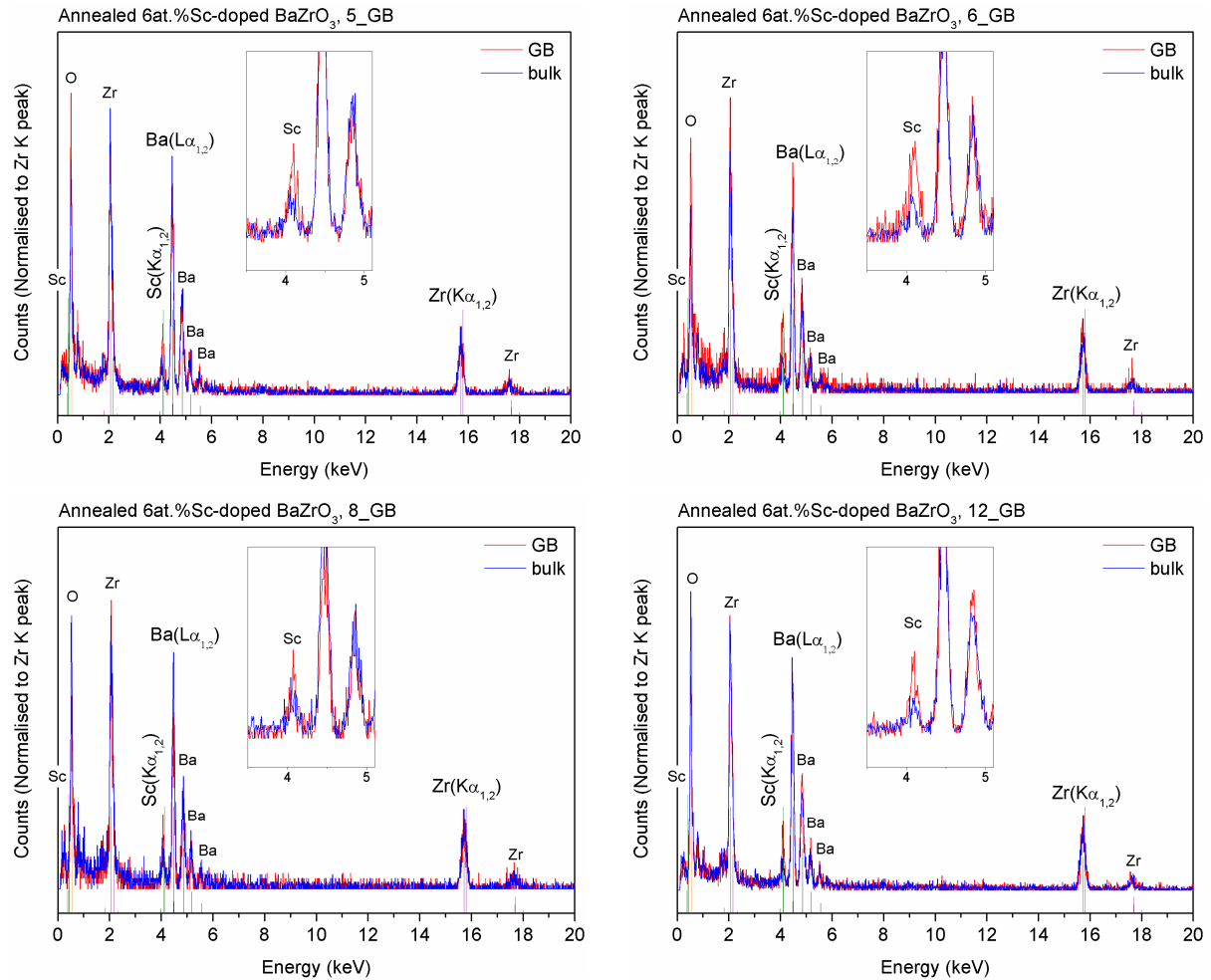


Figure 31 continued

Figure 32 EDXS-TEM spectra of annealed SPS-6 at.%Sc-doped BaZrO₃ (1700°C/20h)

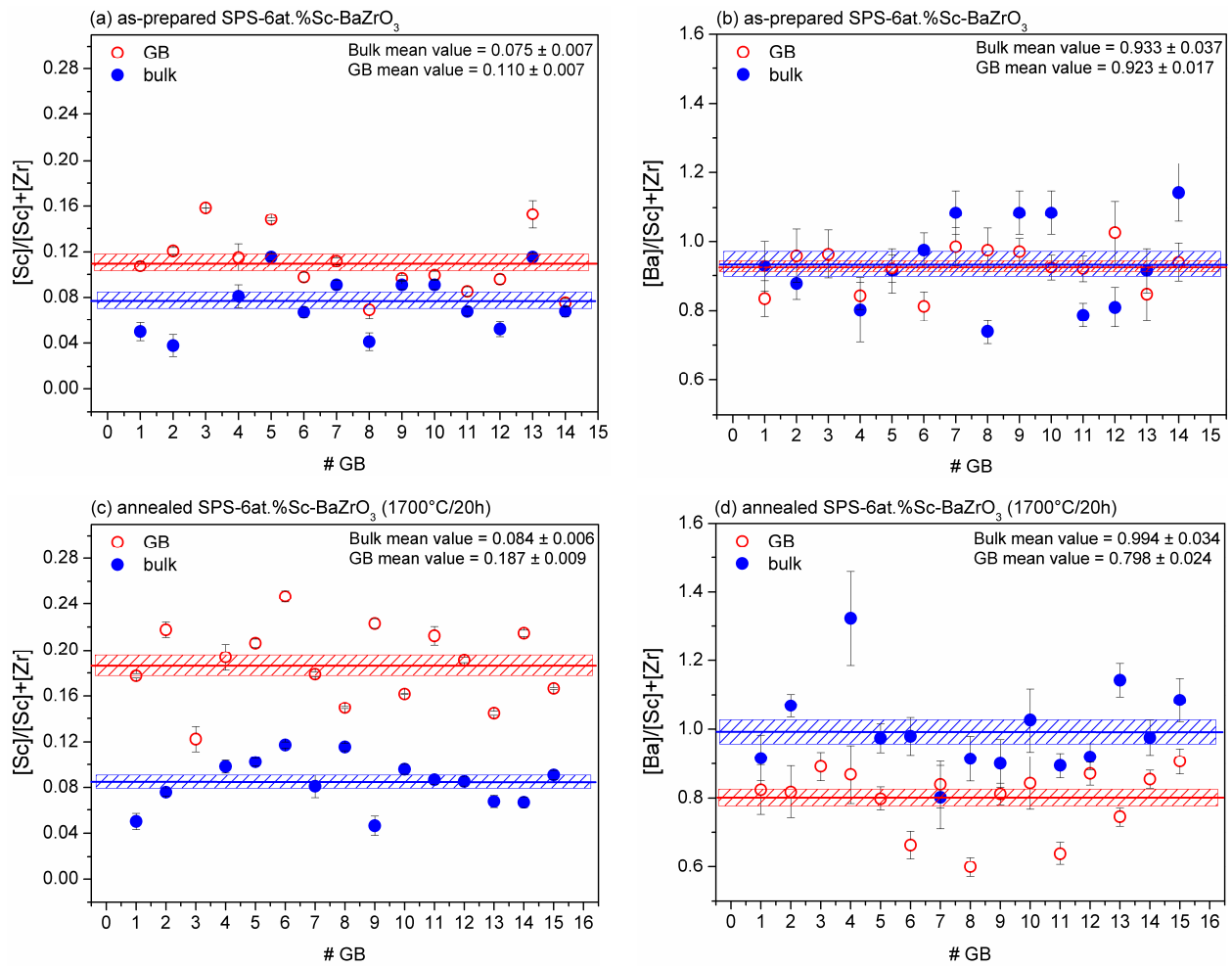


Figure 33 Sc substitution and Ba deficiency of GB region compared to the bulk of as-prepared (a,b) and annealed (c,d) 6 at.%Sc-doped BaZrO₃

EDXS-TEM measurements showed that the grain boundaries have a different composition from the grains, in particular after annealing for 20 hours at 1700°C. This indicates a relationship between GB composition and its electrical properties. Before discussing the space charge model, which is used to explain the electrical properties of GB in relation to its composition, the measured EDXS-TEM data will be discussed in terms of dopant cation segregation and segregation driving forces.

The free energy of segregation (ΔG_s°) can be expressed in terms of the molar fractions of solute/dopant (n_1) and solvent/host (n_2)^[105, 118, 135], as:

$$\ln\left(\frac{n_1}{n_2}\right)_{\text{GB}} = \ln\left(\frac{n_1}{n_2}\right)_{\text{bulk}} - \frac{\Delta G_s^\circ}{RT} \quad (6)$$

The non-configurational entropy of segregation is assumed to be negligible and therefore $\Delta G_s^\circ = \Delta H_s^\circ$. The enthalpy of segregation (ΔH_s°) in ceramics consists of an interfacial energy contribution (ΔH_γ°), a solute-solvent interaction (ΔH_ω°), an elastic strain energy (ΔH_ϵ°) and an electrostatic interaction (ΔH_ϕ°). Typically the last two contributions are more pronounced than the others and for simplicity we assume that $\Delta H_s^\circ = \Delta H_\epsilon^\circ + \Delta H_\phi^\circ$. If the chemical potential is extrinsically fixed, Eq. (6) does good service in most cases however the segregants determine or influence chemical potential. Then ΔH_ϕ depends on the concentration of segregants and Eq. (6) is only formally valid. The solution requires solving Poisson's equations and leads to space charge profiles that are discussed later.

When the electrostatic part is much smaller than the elastic part ($\Delta H_\epsilon^\circ \gg \Delta H_\phi^\circ$), ΔH_s° is proportional to $\{(r_2 - r_1)/r_1\}^2$, where r_1 and r_2 are the ionic radius of host and dopant cations, respectively. On the other hand, when the elastic driving force is negligible compared to elastic energy, ΔH_s° does not depend on r_1 and r_2 :

$$s = \ln \left\{ \frac{\left(\frac{n_1}{n_2}\right)_{\text{GB}}}{\left(\frac{n_1}{n_2}\right)_{\text{bulk}}} \right\} \propto \Delta H_s \propto \begin{cases} \left(\frac{r_2 - r_1}{r_1}\right)^2 & \text{if } \Delta H_\epsilon \gg \Delta H_\phi \\ \left(\frac{r_2 - r_1}{r_1}\right)^0 & \text{if } \Delta H_\epsilon \ll \Delta H_\phi \end{cases} \quad (7)$$

Accordingly when the elastic energy is the major driving force for dopant segregation in BaZrO_3 , one should expect very little segregation for Sc with its small ionic radius mismatch ($(\Delta r/r)_{\text{Sc}} = +0.04$, $(\Delta r/r)_{\text{Y}} = +0.25 \rightarrow s_{\text{Y}}/s_{\text{Sc}} \ll 0.03$). On the other hand, for Sc and Y, a similar degree of segregation is expected when electrostatic potential is the dominant segregation driving force. The measured data on Y and Sc segregation in annealed BaZrO_3 ($s_{\text{Y}} = 1.12$ and $s_{\text{Sc}} = 0.92$) in **Fig. 34** indicates that dopant segregation in this material is mostly driven by electrostatic attraction between dopant cations and positive core charge rather than dopant size mismatch.

Such a positively charged core in many ionic crystals as well as large-bandgap oxides forms due to $V_{\text{O}}^{\bullet\bullet}$ segregation to the GB core, which is explained by different formation energies of point defects in the GB core compared to the grain interior^[81, 136-138]. De Souza^[87] has recently extensively developed the idea of the positive charge caused by oxygen vacancies preferring to reside at the grain-boundary core of low-angle SrTiO_3 bicrystals. Also calculations on Y-

doped BaZrO_3 ^[75] suggest that the positive charge of core arises from the increased oxygen deficiency in the GB core of this material.

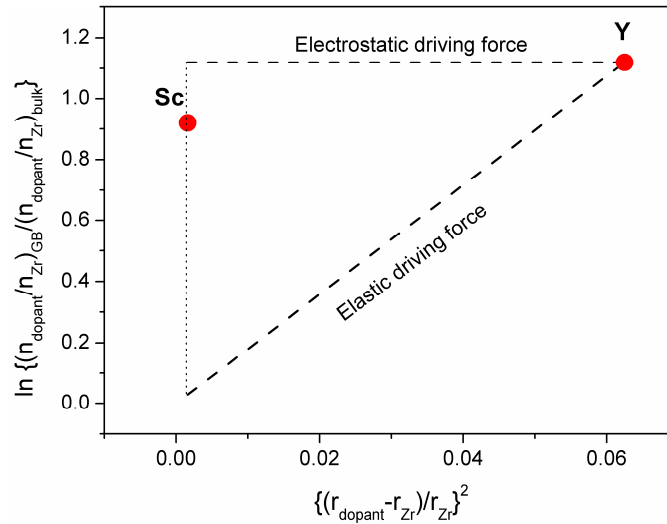


Figure 34 Contribution of elastic and electrostatic driving forces to the segregation of scandium in comparison with segregation of yttrium to the GB of BaZrO_3

1.7.5.1 Dopant segregation and space charge model

Fig. 35 shows simple schematics of a positively charged GB core and its related space charge layers. During annealing at high temperatures, at which dopant cations are mobile, the positive charge of the core can (partly) be compensated by either accommodation of dopant cations in the GB core (**Fig. 35-a**) or their accumulation in the space charge layers (**Fig. 35-b**). Accommodation of negatively charged dopant in the core annihilates a part of core charge and therefore decreases the GB potential. Thus proton depletion will be less and a higher GB conductivity is expected (negative dopants are mobile and the space charge potential still positive). Dopant enrichment which occurs in space charge layers compensates part of core charge, the proton depletion decreases, the space charge layers get thinner^[113, 139] and a lower GB resistivity is expected. Note that dopant accumulation in the GB region means transition to the Gouy-Chapman model away from the Mott-Schottky model.

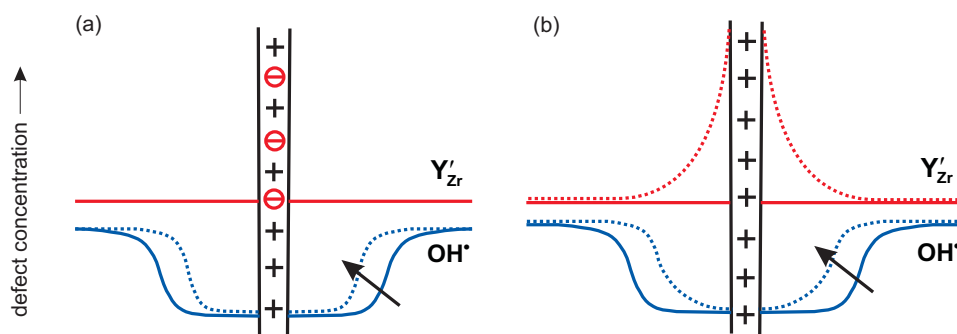


Figure 35 Space charge model, positively charged core and effect of segregation of negatively charged dopant (a) to the core and, (b) in space charge layers

Such a behavior was discussed in detail for Y-ZrO₂^[139]. The effect of GB dopant accumulation on enhancement of GB conductivity in acceptor-doped BaZrO₃ is discussed by Iguchi^[140]. They experimentally found a decrease of barrier height with increasing dopant concentration, which is parallel with a slightly increased yttrium excess in the GB region.

Our results on as-prepared and annealed samples are in a good agreement with the proposed models, and the large difference in GB conductivities and related significant composition differences measured by TEM clarifies the coupled role of dopant segregation and space charge layers.

In the absence of dopant segregation, the classical Schottky-barrier model extended to the case of mobile ions can be used to explain the GB defect profile of as-prepared YBZ (**Fig. 36-a**). This model assumes that dopant concentration is constant within the system ($[Y]_b \approx [Y]_{GB}$). The positive core charge is compensated by strong depletion of positively charged defects and the space charge layer extends to several nanometers. The potential barrier (**eq. (14)**) at the GB of as-prepared SPS-6YBZ is about 0.68 V and the GB thickness (**eq. (12)**) is about 5.5 nm (Mott-Schottky model).

A simultaneous dopant segregation to the core and space charge region^[141], due to presence of both elastic and electrostatic driving forces is possible. In order to get more insight about the exact location of segregants in the annealed sample, we separately discuss the resistivity of GBs for the two extreme cases of dopant segregation **(i)** only to the GB core and **(ii)** only to the space charge zone.

(i) Segregation only to the core:

According to the TEM-EDXS measurements $[Y]_b \approx 4$ at.% and $[Y]_{GB} \approx 12$ at.%. When all the detected Y in an area of 2×3 nm is located only in the core of 1 nm thickness, then the $[Y]_{core}$

is about 24 at.% and the excess dopant due to segregation is about $[Y]_{GB} - [Y]_{core} = 20$ at.%. Then the excess charge created by singly charged segregant cations (Y_{Zr}') is about $Q_{seg.} = 0.31$ Cm^{-2} in the GB core.

The core charge for as-prepared sample can be calculated using $Q_{interface} = (8\epsilon\epsilon_0e[Y]_b\Phi_0)^{1/2}$ according to Mott-Schottky model. The calculated potential using **eq. (14)** is $\Phi_0 = 0.68$ V and for $[Y]_b = 4$ at.% and $\epsilon = 40$, $Q_{interface} = 0.41$ Cm^{-2} . If all the segregants are accommodated in the GB core, the remaining core charge ($\Delta Q = Q_{interface} - Q_{seg.} = 0.10$ Cm^{-2}) would correspond to $\Phi_0 = Q^2/8\epsilon[Y]_be = 0.04$ V.

The proton profile for $\Phi_0 = 0.04$ V (**Fig. 36-b**) can be derived using **eq. (13)**. In this way, the GB conductivity would increase by about 6 orders of magnitude. Since this rough estimate yields a much stronger increase of σ_{GB} than observed, it points towards the fact that the segregated dopant cations are partially or fully located in the space charge zone. Now we discuss the second case.

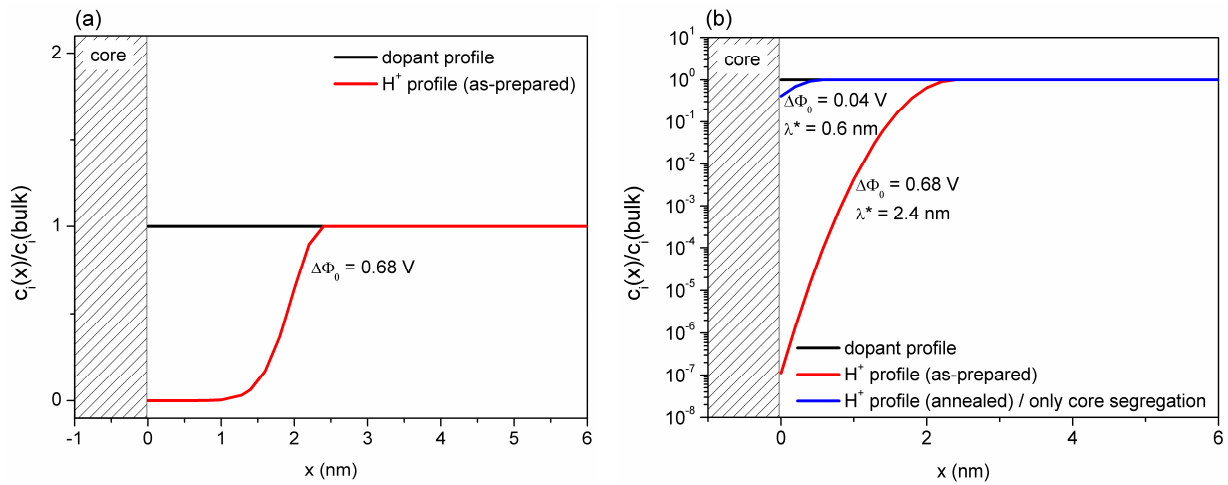


Figure 36 Dopant and proton profile of (a) as-prepared sample ($\Phi_0 = 0.68$ V) according to Mott-Schottky model, and (b) as-prepared sample at 200°C compared to the annealed sample when all the segregants are accumulated in the core ($\Phi_0 = 0.04$ V)

(ii) Segregation only to the space charge zone:

The electrical properties of the space charge zone depends on the profile of dopant cations and defects in this region.

As it was already mentioned, the Mott-Schottky model is used for the as-prepared sample with slight dopant segregation. However, the simple Mott-Schottky model cannot be used for the annealed sample which exhibits a significant GB segregation. It is plausible to assume that

during annealing at high temperature, the Y cations become mobile^[133, 134] and at least partially follow the so-called Gouy-Chapman model (Debye model)^[139, 142].

Here we take the approach proposed by Lee^[139] to describe the behaviour of GB electrical properties with a high dopant enrichment in space charge layers.

The resistance of GB regardless of dopant profile can be expressed as

$$R_{\text{sp.ch.l.}} = \frac{A}{\sigma_{i\infty}} \int_0^{\lambda_{\text{sp.ch.l.}}} \frac{c_{i\infty}}{c_i(x)} dx \quad (23)$$

$c_{i\infty}$ and $\sigma_{i\infty}$ are the concentration and conductivity of the species i in the bulk. The species i are sufficiently mobile and are in equilibrium according to

$$\frac{c_i(x)}{c_{i\infty}} = \exp\left(\frac{z_i e \Phi(x)}{kT}\right) \quad (24)$$

Then the integration of **eq. (23)** using **eq. (24)** will be

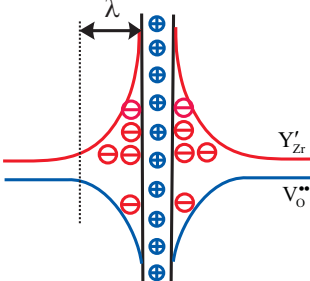
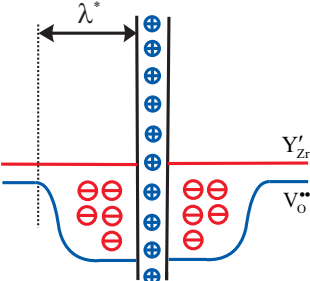
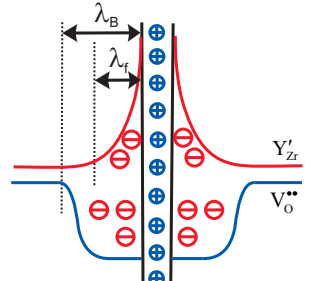
$$R_{\text{sp.ch.l.}} = \frac{A}{\sigma_{i\infty}} \frac{\exp\left(\frac{z_i e \Phi_0}{kT}\right)}{\left(\frac{z_i e}{kT} \frac{\partial \Phi}{\partial x}\right)_{x=0}} \quad (25)$$

The term $\left(\frac{\partial \Phi}{\partial x}\right)_{x=0}$ depends on the defect structure of GB zone. This term has been calculated^[139] for the so-called Gouy-Chapman, Mott-Schottky and frozen dopant profile in **Table 5**.

During annealing at high temperature, the Y cations become mobile and are able to reach the equilibrium concentration (cf. **Fig. 29** : $T_{\text{freezing}} > 1550^\circ\text{C}$), but the pure Gouy-Chapman case cannot be used for the annealed sample since dopant cations are not mobile at lower temperatures ($T < 800^\circ\text{C}$) and do not follow the equilibrium concentration. Thus a frozen dopant profile was used to calculate the resulting $R_{\text{sp.ch.l}}$ in the annealed sample.

Here we assume similar GB potential (Φ_0) for Mott-Schottky and Gouy-Chapman situations ($\Phi_0(\text{as-prepared}) = \Phi_0(\text{annealed}) = 0.68 \text{ V}$). It is worthy to mention that De Souza^[87] has explained different situations which lead to a constant or variable GB potential, but at high temperatures, in which dopant cations are mobile, the GB potential barrier can be considered as constant to a good approximation.

Table 5 Different situations for GB space charge model^[139]

Model	$\left. \frac{\partial \Phi}{\partial x} \right)_{x=0}$	definitions
Gouy-Chapman 	$-\frac{kT}{z_1 e} \frac{1}{2\lambda} \zeta_{10}^{1/2}$	z_1 : charge of species 1 ($z_1 = 1$ for Y'_{Zr}) $\lambda = \sqrt{\frac{\epsilon kT}{2z_1^2 e^2 c_{1\infty}}}$ $\zeta_{10} = \frac{c_1(0)}{c_{1\infty}} = \exp\left(\frac{z_1 e \Phi_0}{kT}\right)$
Mott-Schottky 	$\frac{z_1 e c_{1\infty}}{\epsilon} \lambda^*$	$\lambda^* = \sqrt{\frac{2\epsilon \Delta \Phi_0}{z_1 e c_{1\infty}}}$
Frozen dopant profile 	$\frac{z_1 e c_{1\infty}}{\epsilon} \left[\lambda_B + 4\lambda_f \left(\frac{\zeta_{10, \text{frozen}}^{1/2}}{2} - 1 \right) \right]$	λ_f : thickness of frozen profile λ_B : thickness of depletion $\left(\frac{\lambda^*}{\lambda_B} \right)^2 = 1 + 8 \left(\frac{\lambda_f}{\lambda_B} \right)^2 \ln \frac{\zeta_{10, \text{frozen}}^{1/2}}{2}$

To calculate the term $\left. \frac{\partial \Phi}{\partial x} \right)_{x=0}$, we need to know the frozen dopant profile. The mobile dopant cations ($> 1550^\circ\text{C}$) are in equilibrium according to

$$\frac{c_Y(x)}{c_{Y(\text{bulk})}} = \exp\left(\frac{e\Phi(x)}{kT}\right) \quad (26)$$

and

$$\zeta_{10} = \frac{c_Y(0)}{c_{Y(\text{bulk})}} = \exp\left(\frac{e\Phi_0}{kT_{\text{freezing}}}\right) \quad (27)$$

$\zeta_{10} \sim 75$ for freezing temperature of 1550°C and $\Phi_0 = 0.68$ V. The width of frozen profile (λ_f) using **eq. (11)** with $\varepsilon_r = 40$ and $c_Y = 4$ at.% is ~ 0.6 nm. With the calculated $\lambda^* = 2.4$ nm from **eq. (12)**, λ_B is approximately 1.4 nm. Accordingly

$$\frac{R_{\text{sp.ch.l.}}(\text{annealed})}{R_{\text{sp.ch.l.}}(\text{as-prepared})} = \frac{\frac{z_1 e c_{1\infty}}{\varepsilon} \left[\lambda_B + 4\lambda_f \left(\frac{\zeta_{10,\text{frozen}}^{1/2}}{2} - 1 \right) \right]}{\frac{z_1 e c_{1\infty}}{\varepsilon} \lambda^*} \approx 4 \quad (28)$$

The estimated ratio shows that in the presence of a strong dopant segregation ($\zeta_{10} \sim 75$) in space charge layers, the resistivity decreases by 0.6 order of magnitude at maximum.

On the other hand, the resistance of space charge layers in as-prepared and annealed samples using brick layer model (**eq. (29)**), results in the ratio of $R_{\text{sp.ch.l.}}(\text{annealed}) / R_{\text{sp.ch.l.}}(\text{as-prepared}) \approx 1000$ at 200°C .

$$R_{\text{sp.ch.l.}} = \frac{1}{\sigma_{\text{bulk}}} \frac{R_{\text{GB}}}{R_{\text{bulk}}} \frac{d_g}{2} \quad (29)$$

In summary, if GB core accommodates all the segregated dopant cations, the conductivity should increase by 6 orders of magnitude (case (i)) and accumulation of dopant cations only in the space charge zone can, at the highest, decrease the resistivity of space charge layers a factor of 4 (case (ii)). Therefore, the GB conductivity of the annealed samples has increased by ~ 3 orders of magnitude due to simultaneous dopant segregation to the GB core and space charge region. Obviously accommodation of a small part of segregants in the core is more effective in reducing the blocking effect than presence of majority of dopant cations in the space charge zone.

It should be mentioned that GB potential barrier and GB thickness of annealed samples in **Table 4**, using Mott-Schottky model, with a small correction due to the effect of dopants in space charge layers, gives a good agreement with the values estimated here.

EDXS line scan with the step size of 0.7 nm resolved the extension of segregated dopant cations near the GB. In **Fig. 37**, the dopant concentration is shown as a function of distance from the GB for the annealed Sc-doped sample. The segregation extends no farther than 3-4 nm.

The rough estimate of core charge and the amount of segregated dopant already implied that the segregated element is at least partially located in the space charge layers. The dopant

profile obtained by EDXS line scan also confirms the presence of dopants in a region larger than the actual core width. However, the limited spatial resolution of the TEM (VG) does not allow a final conclusion about the segregation of dopant into the GB core.

In principle, the local environment of atoms in the GB region compared to the bulk can give information on the possible formation of different phases containing yttrium, substitution of Y at the Ba site, formation of interstitials and even reduction of Zr^{+4} to Zr^{+3} at the GB. EELS measurements on Y-doped samples show very similar O K and Ba K edges. Due to overlap of Y and Zr M absorption edges it was difficult to identify variations. While in principle cation interstitials could form in the more loosely packed GB core, one should keep in mind that they have not been observed in any bulk perovskite.

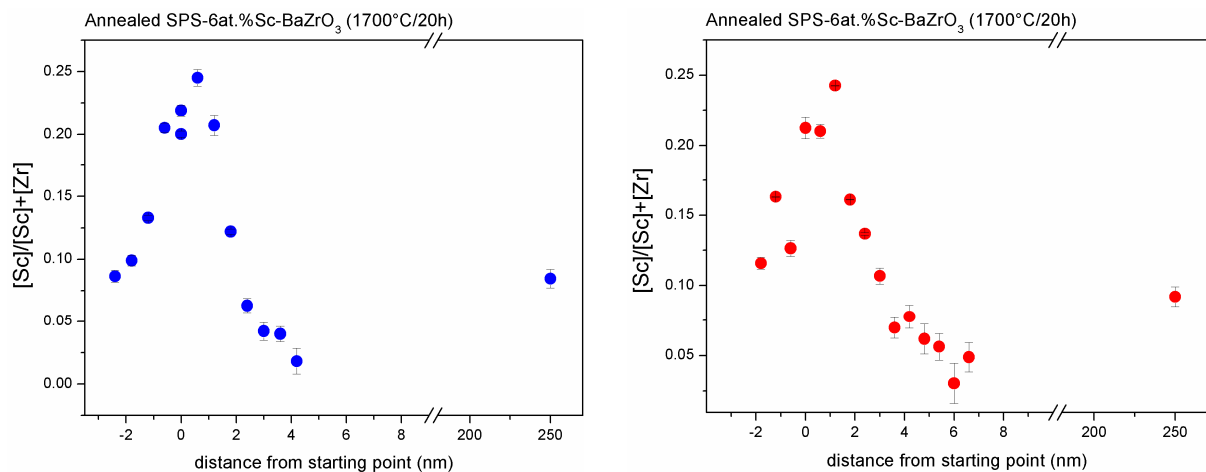


Figure 37 Line scans across two GBs of annealed SPS-6 at.%Sc-doped BaZrO₃ (1700°C/20h) using spot EDXS analysis

Beside the high GB resistivity, the limited grain growth is another issue which leads to bad sintering behavior and high grain boundary density in polycrystalline acceptor-doped BaZrO₃. The grain growth is closely related to the defect chemistry and structure of GB, which, in turn, depends on the type and level of dopant and sintering temperature. The undoped BaZrO₃ after annealing at 1700°C for 20 h exhibits large grains of ~ 10 -20 μm diameter (**Fig. 38**). It is reasonable to conclude that grain boundary mobility is lowered by the presence of dopant cations (Y as well as Sc) in the GB region. Dopant segregation to GBs is known to decrease grain growth due to solute drag. Also sintering needs cation diffusion, and in perovskites this is limited by the mobility of cation vacancies^[143, 144]. Doping creates $V_{\text{O}}^{\bullet\bullet}$ and according to the

Schottky reaction, decreases the amount of cation vacancies which might slow down the sintering process.

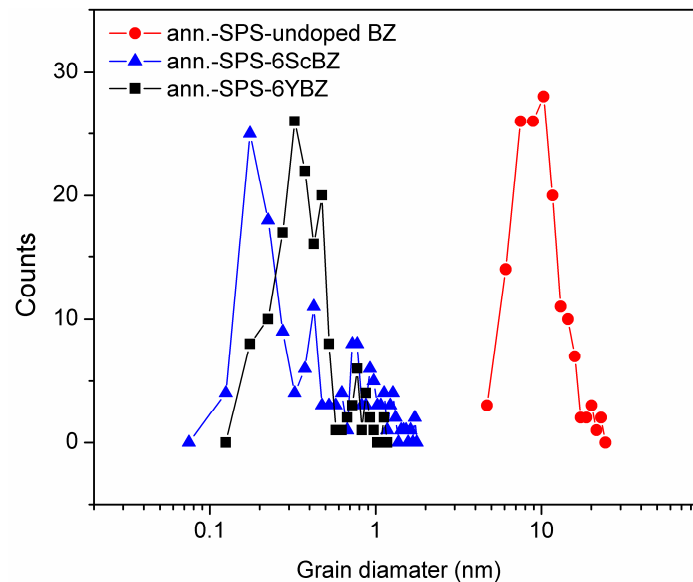


Figure 38 Grain size distribution of annealed SPS samples of Y-doped, Sc-doped and undoped BaZrO₃, data extracted from SEM image.

Orientation Imaging Microscopy (OIM) has been used to determine whether in doped samples a particular orientation relationship is preferred over others. **Fig. 39-c** shows that, as expected for polycrystalline oxides, most of the GBs in both doped and undoped samples cannot be classified as CSL GBs according to the Brandon criterion^[145]. As seen in Fig. 39-d, similar to most of the polycrystalline perovskite oxides^[146] $\Sigma 3$ is preferable over the other CSL boundaries.

The Σ value of CSL boundaries, as well as the misorientation angle, do not show a notable difference between undoped and Y-doped BZ (**Fig. 39-d,e**). Here we conclude that although the presence of dopant at the GB suppresses grain growth, it does not favor the existence of specific GB orientations which might be more blocking. Similar studies on YBZ with different dopant content and different sintering conditions did not reveal any difference in Grain Boundary Distribution Character (GBDC).^[59, 60]

¹ The Brandon criterion asserts that boundaries with a maximum deviation $\Delta\theta = 15^\circ/\sqrt{n}$ (n is the CSL index) might persist as CSL grain boundaries.

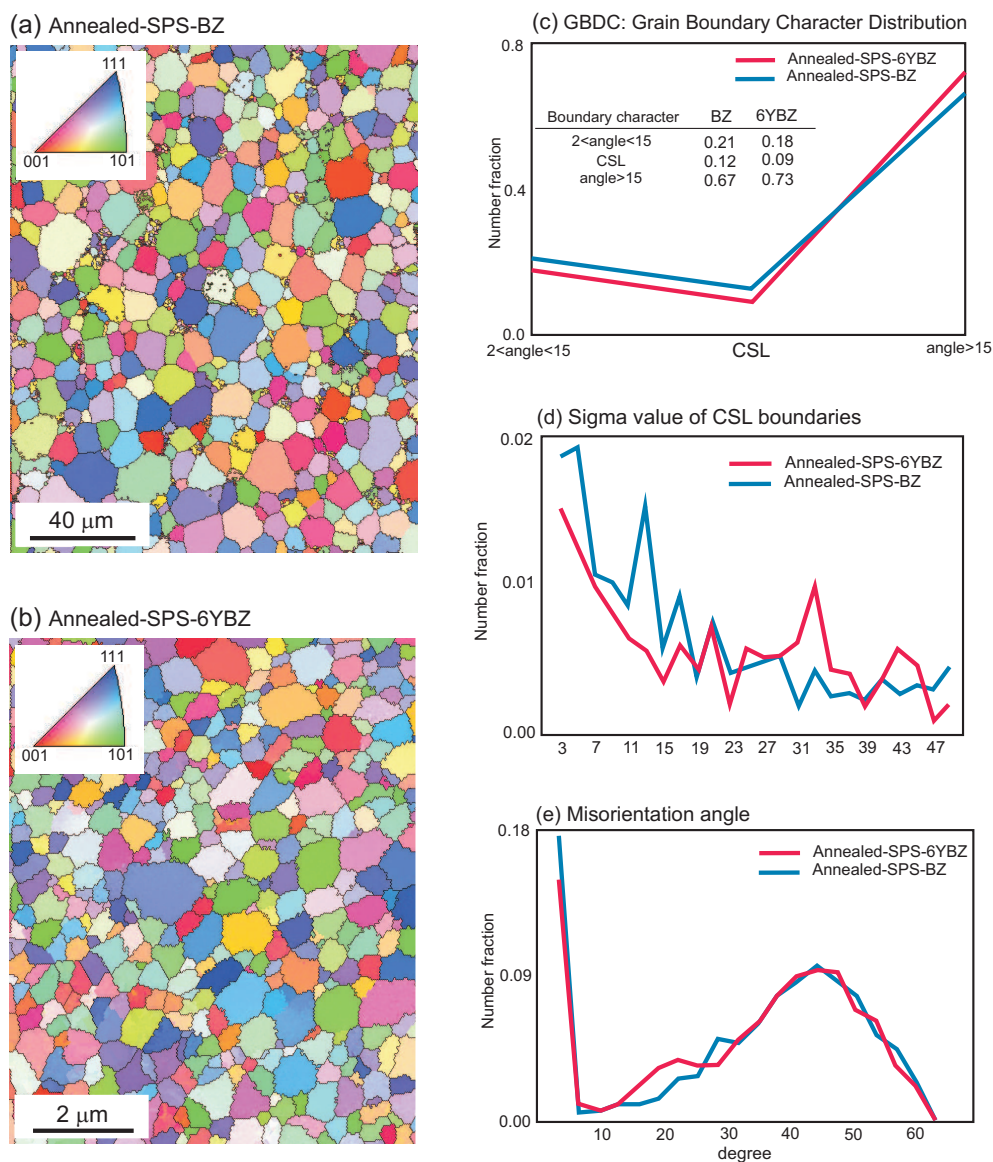


Figure 39 Inverse Pole Figure (IPF) map of (a) annealed SPS-undoped BZ and (b) annealed SPS-6YBZ, (c) Σ value of CSL boundaries, (d) Grain Boundary Character Distribution (GBDC) and (e) misorientation angle of annealed SPS 0YBZ and 6YBZ

1.7.6 Effect of Cesium

Investigation of as-prepared and annealed Y-doped BaZrO₃, revealed that the GB core is positively charged and a higher dopant segregation, partially compensating the core charge, decreases proton depletion and results in higher GB conductivities. Therefore, introducing some negatively charged defects with a high tendency for segregation to the GB core should increase the GB conductivity of BaZrO₃.

Increasing Y concentration to more than 20 at.% does not seem promising due to defect association and formation of noncubic phases which lower the bulk conductivity^[44, 147, 148]. Doping or co-doping of Zr-site with oversized dopants such as Gd, Nd and Pr, with a larger driving force for segregation to the core, can cause a higher cross substitution of dopant to the A-site ($[D]_A^+$) which creates positively charged species, decreases the amount of oxygen vacancies and consequently lowers the conductivity of both bulk and GB^[49, 149]. Therefore, we decided to introduce a singly charged dopant to the Ba-site which can, by segregation to the GB region, lower the positive core charge. One candidate was singly charged Cs^{+1} ($r = 1.88 \text{ \AA}$ for CN: 12, $r = 1.67 \text{ \AA}$ for CN: 6) with a significantly larger size than Ba^{+2} (1.61 \AA). Substitution of Zr^{+4} by Cs^{+} is prohibited by the Cs^{+} large ionic radius compared to Zr^{+4} (0.72 \AA). Due to its 15% size excess, Cs_{Ba} is expected to segregate to the GB core and lower the positive core charge. Little is known on Cs-doping in perovskites. Among similar structures, $SrTiO_3$ has been doped by up to 20 at.% cesium on the A site^[150].

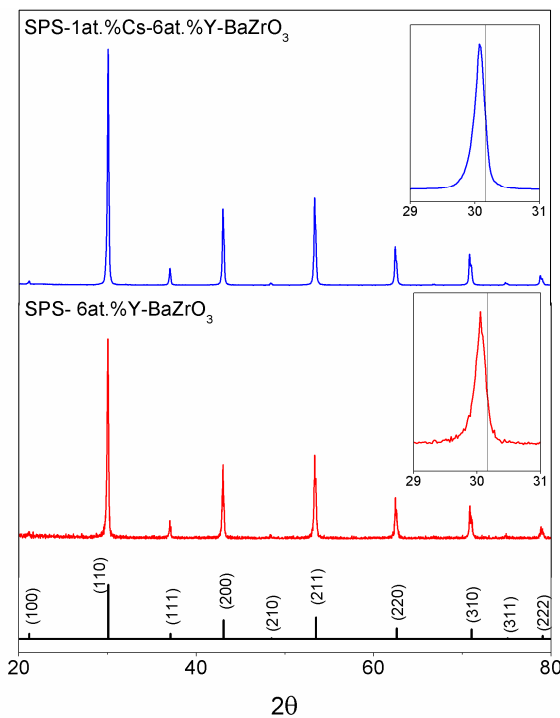


Figure 40 XRD pattern of SPS-1 at.%Cs, 6 at.%Y-doped $BaZrO_3$ ($a = 4.203 \text{ \AA}$)

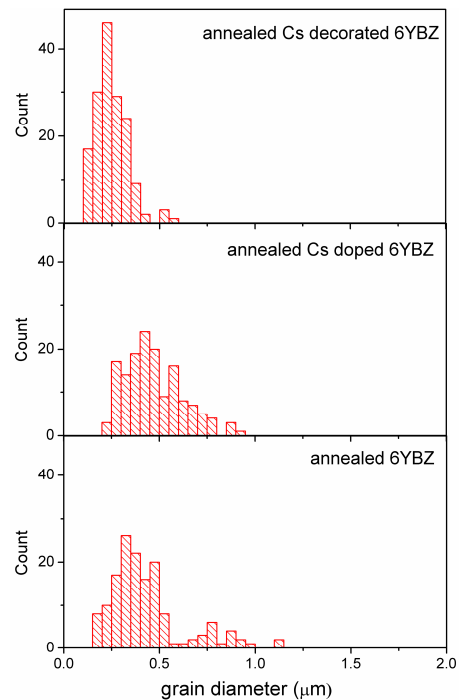


Figure 41 Grain size distribution of annealed Cs-doped and Cs-decorated samples in comparison with annealed 6YBZ

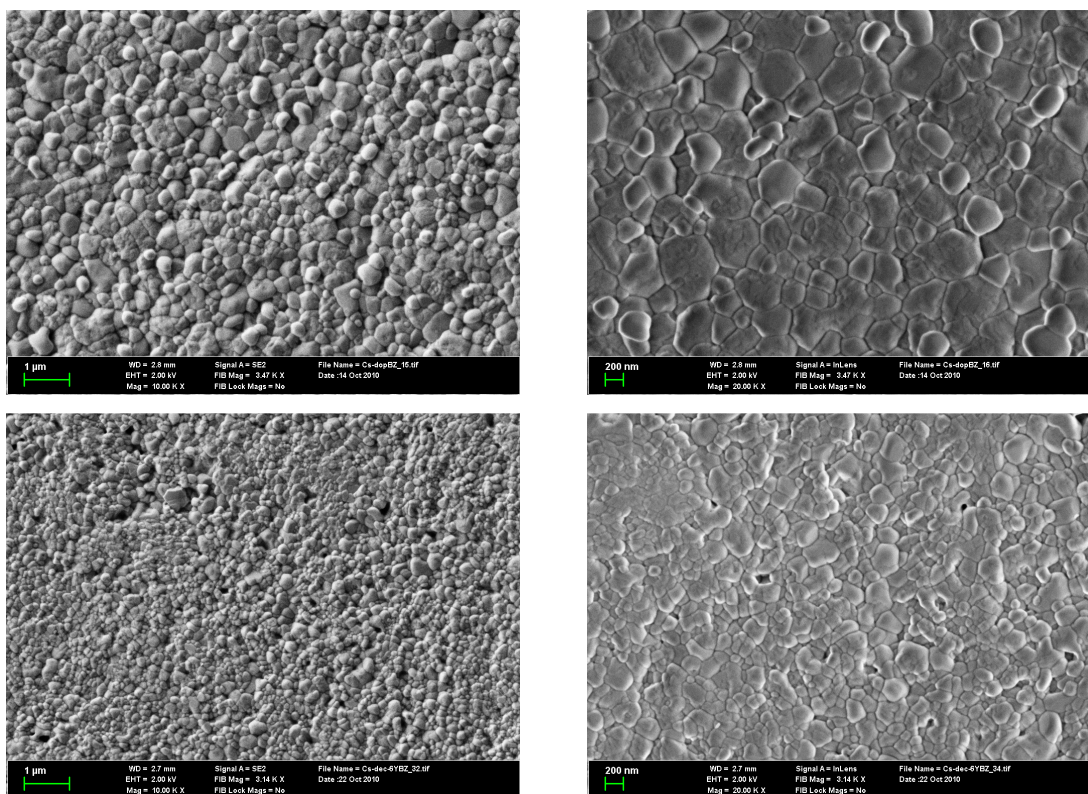


Figure 42 SEM images of annealed Cs doped (top) and Cs-decorated (bottom) 6YBZ

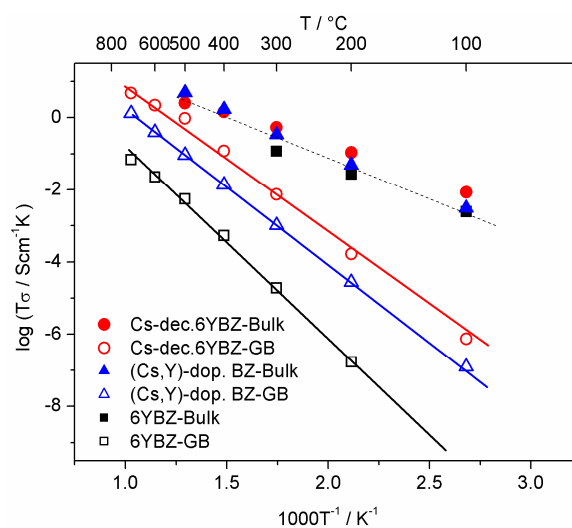


Figure 43 Arrhenius plots of Y-doped, (Cs,Y)-doped and Cs-decorated Y-doped BaZrO_3 in wet N_2 ($p_{\text{H}_2\text{O}} = 20$ mbar)

The Cs-decorated sample has an even higher GB conductivity than the Cs-doped sample, which can be explained by the higher local Cs concentration at the GB. The effect of annealing on the GB conductivity enhancement is consistent with that in Y-doped BZ (**Fig. 44**). **Table 6** summarizes the calculated potential barrier and width of GB in Cs-doped and Cs-decorated samples. The Cs-doped as well as Cs-decorated 6YBZ samples exhibit a lower GB potential barrier than the 6YBZ, and after annealing the barrier is even smaller.

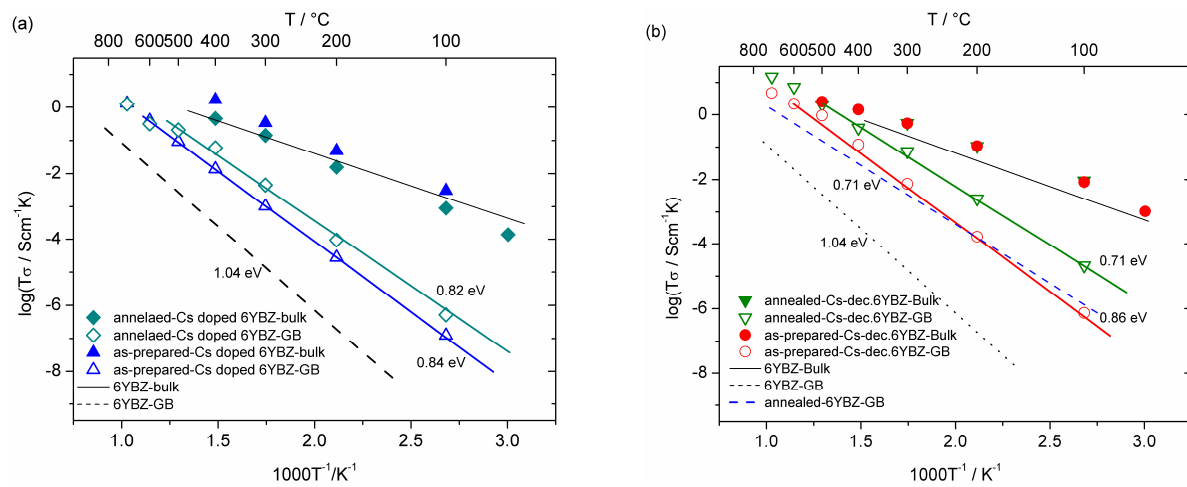


Figure 44 Effect of high-temperature annealing (1700°C/20h) on GB conductivity of (a) Cs doped and, (b) Cs decorated 6 at.% Y-doped BaZrO₃ in wet N₂ (pH₂O = 20 mbar)

Table 6 Bulk and GB potential barrier and GB thickness of as-prepared and annealed samples at 200°C

Sample		Φ_0 (V)	$\delta_{GB} = 2\lambda^*$ (nm)
6YBZ	as-prepared	0.68	5.45
	annealed	0.49	4.62
Cs-dop. 6YBZ	as-prepared	0.58	5.03
	annealed	0.48	4.58
Cs-dec. 6YBZ	as-prepared	0.56	4.94 [#]
	annealed	0.49	4.62 [#]

The GB potential and thickness are calculated assuming Mott-Schottky situation using **eq. (14)** and **eq. (12)**, respectively.

[#] The concentration is not known for the sample and the calculated numbers correspond to 6 at.% Y.

The conductivity measurements confirmed the idea of using Cs^+ as a negatively charged dopant which lowers the core charge. Nevertheless, it is necessary to also consider other reasons of GB conductivity enhancement by Cs.

Cs incorporation into the structure as a substitutional species in Ba-site, creates oxygen vacancies according to



Obviously cesium doping is accompanied by formation of oxygen vacancies, which can be filled by hydroxide ions and lead to a higher protonic conductivity in the bulk and even at the GB. However, since the bulk conductivity of (Cs,Y)-doped sample does not show a notable increase (**Fig. 43**), this effect is negligible at least for 1 at.% Cs dopant.

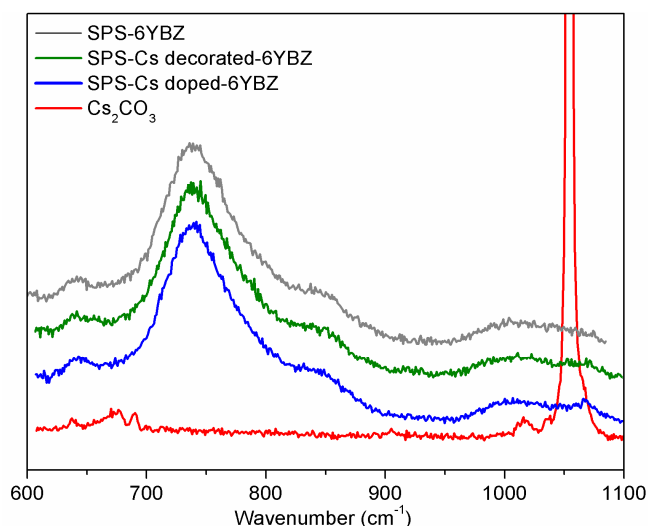


Figure 45 Raman spectra of cesium carbonate, Y-doped BaZrO_3 and cesium containing samples after exposing to CO_2 gas at 600°C

The absence of secondary Cs phases at the GB cannot completely be ruled out only by X-ray diffraction analysis, due to sensitivity limits. Reported proton conductivity of CsOH and other alkali hydroxides^[151, 152], can raise questions about the role of Cs on GB conductivity. According to ref.^[151, 152], the presence of CsOH in the grain boundary core could cause a drastic conductivity change in the temperature range of $500\text{-}600^\circ\text{C}$ in water and even CO_2 containing atmospheres. If the conductivity of grain boundaries stems from the formation of a hydroxide phase, a conductivity drop of about 4-5 orders of magnitude at around 550°C during cooling is expected^[151], which is not observed for Cs-doped and Cs-decorated samples.

Furthermore, the existence of some residual Cs compounds was checked by Raman spectroscopy. As the room temperature Raman and IR peaks of CsOH at 3535 cm^{-1} (O-H stretch vibration) are not very intense^[153], the samples (crushed to powder) were kept at 800°C and cooled down under pure CO_2 to form Cs_2CO_3 which has a sharp Raman line (1040 cm^{-1} -internal bending vibration of CO_3^{2-}) at room temperature^[154]. A Raman spectrum of cesium carbonate was used as a reference. The samples were sealed in sample holders with quartz window for Raman spectroscopy. Raman spectra of Cs-doped and Cs-decorated samples have the typical features of 6YBZ and no Raman line is observed at the frequency of 1040 cm^{-1} (**Fig. 45**).

To check the stability of GB conductivity, samples were kept at 700°C for 3-4 weeks under wet N_2 and their resistivity was recorded (**Fig. 46**). The conductivity of the initially dry sample increases after exposing the samples to wet atmosphere and then became stable.

In summary, according to the proposed model and the discussed effect of dopant segregation in acceptor-doped BaZrO_3 , substitution of Ba^{+2} site by Cs^+ improves the GB electrical properties. This can be regarded as a confirmation for the suggested mechanism as well as a practical solution for increasing total conductivity of this electrolyte material.

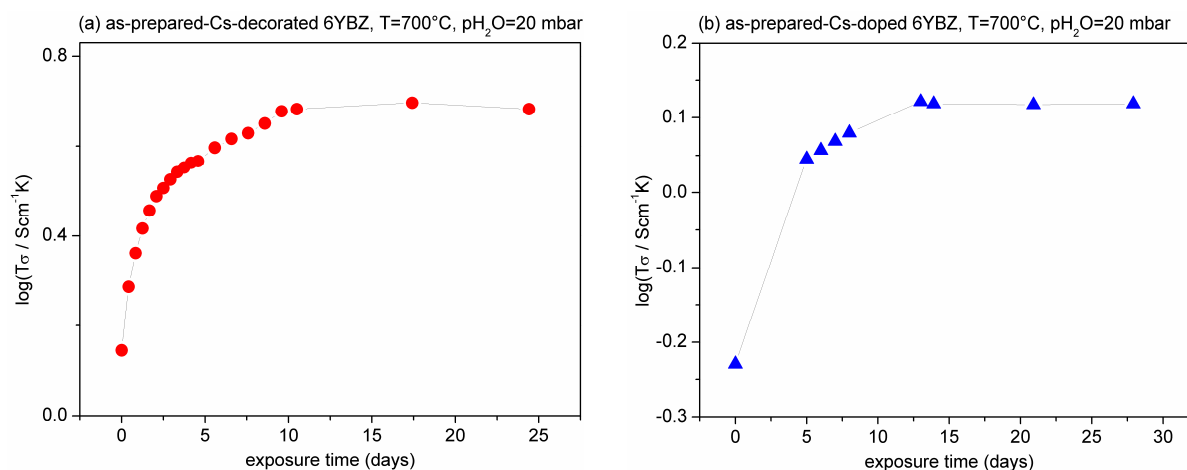


Figure 46 Conductivity change of (a) Cs-decorated and, (b) Cs-doped 6 at.% Y-BaZrO₃ with exposure time after switching to wet N_2 at 700°C

1.7.7 Effect of cooling rate

In the previous part, it was shown how the GB properties are influenced by additional annealing. Now the effect of cooling rate is studied on the GB conductivity of conventionally sintered samples. **Fig. 47-a,b** shows that GB conductivity in Y-doped and Sc-doped samples increases by 2-4 orders on increasing the cooling rate (down from sintering temperature) from 50°C/h to 300°C/h, while the bulk conductivity is independent of cooling rate. Applying higher cooling rates on 15YBZ (**Fig. 48-a**) does not show any further σ_{GB} improvement. The GB conductivity after long term measurement under wet conditions at 700°C did not drop and was still higher than that of the slowly cooled sample (**Fig. 48-b**). This excludes the possible effect of some residual stress remaining from rapid cooling.

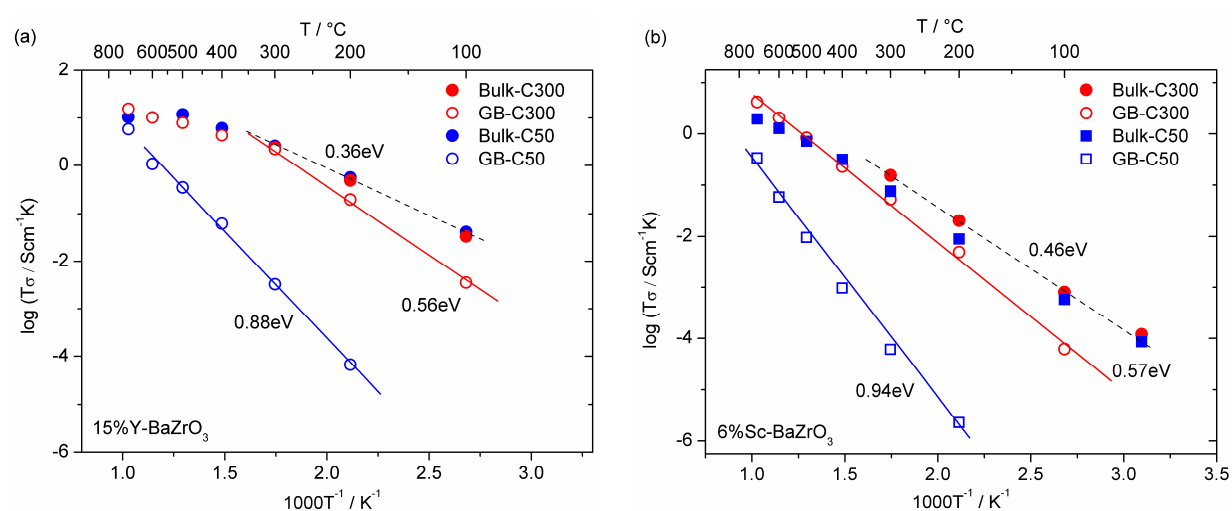


Figure 47 Arrhenius plots of slowly (C50) and rapidly (C300) cooled sample of (a) 15YBZ and (b) 6ScBZ

The lower GB conductivity of slowly cooled ceramics has often been correlated to the formation of precipitates and/or glassy phases at the grain boundary during cooling^[76, 155]. This however cannot explain the behavior of impurity free GBs in the samples studied here since TEM proved “clean” GBs.

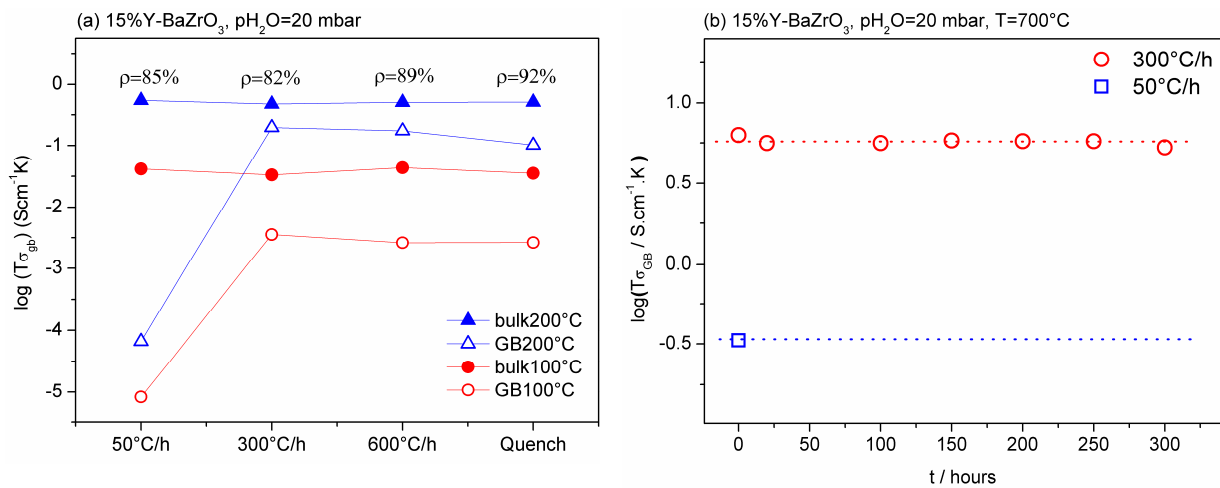


Figure 48 GB conductivity of 15YBZ as a function of (a) cooling rate and (sample density is indicated) (b) exposure time at 700°C

While the dopant cations are mobile, they follow the equilibrium distribution that corresponds to each temperature. Below a certain temperature the cations become immobile. Thus, the dopant distribution of all samples is a frozen dopant profile from some higher temperatures. This can result in lower dopant segregation for rapidly cooled samples^[104, 109, 135, 156]. The lower dopant segregation, as it was investigated for as-prepared and annealed SPS samples, leads to a higher proton depletion and lower GB conductivity. Thus, this effect is not able to explain the enhanced GB conductivity of rapidly cooled and quenched samples. Rather the following explanation is more conclusive.

As it was already mentioned, the conventionally sintered samples lose a few percent of barium during sintering. Therefore, the sample, at the end of the conventional sintering step at 1700°C, contains a considerable amount of barium vacancies (V_{Ba}'') which can play a decisive role in the defect structure of the GB. One should keep in mind that the CS samples have a significant remaining porosity (typically $\rho \approx 90\%$), and that pores are intergranular, suggesting BaO loss mainly from the GB region. For donor-doped BaTiO₃, it has been observed that diffusion of barium vacancies from GB into the grain is very slow^[157]. Thus, the concentration of V_{Ba}'' in the GB region of quenched samples is higher. The accumulated doubly charged barium vacancy can compensate a part of positive core charge and lead to less pronounced proton depletion in the GB region. The considerable barium vacancy concentration, which is doubly charged, can explain the significant conductivity enhancement of rapidly cooled samples. **Fig. 49** suggests a simple schematic of the defect concentration in

GB region of slowly and rapidly cooled samples. Mobility of V''_{Ba} is quite low at 700 °C, leading to stable GB conductivity values as shown in **Fig. 48-b**.

As the diffusivity of V''_{Ba} is a function of temperature ($D_{V''_{Ba}} = A \exp(-E/kT)$), the rate with which the sample is cooled down and thus the “freezing conditions” are expected to change the amount and width of V''_{Ba} accumulation region.

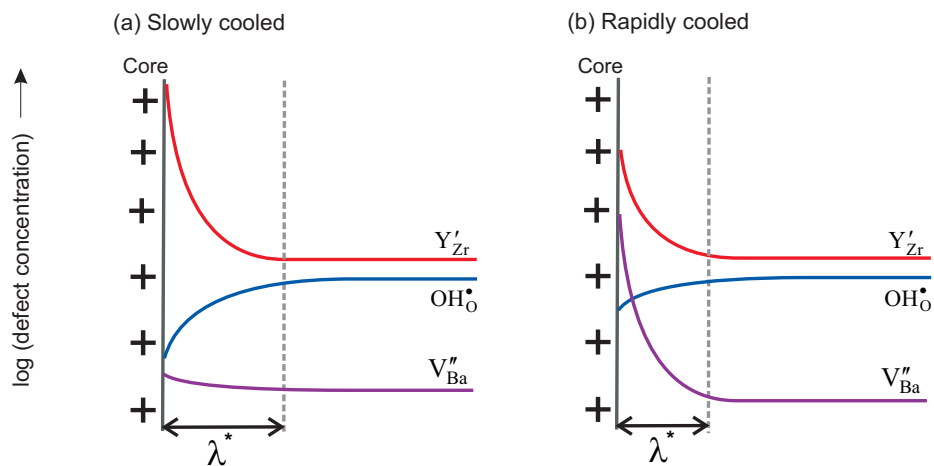


Figure 49 Proposed GB defect profile for (a) slowly, and (b) rapidly cooled samples

1.8 Effect of reducing conditions on grain boundary conductivity

Investigations on the composition and electrical properties of GBs in acceptor-doped BaZrO₃ revealed that the space charge concept allows so far a consistent explanation for the blocking character of GB in this material. As a consequence of a positive charge of core not only protons also oxygen vacancies are depleted. Negatively charged defects such as electrons are expected to accumulate adjacent to the positively charged core^[96, 99, 100] (**Fig. 50-a**).

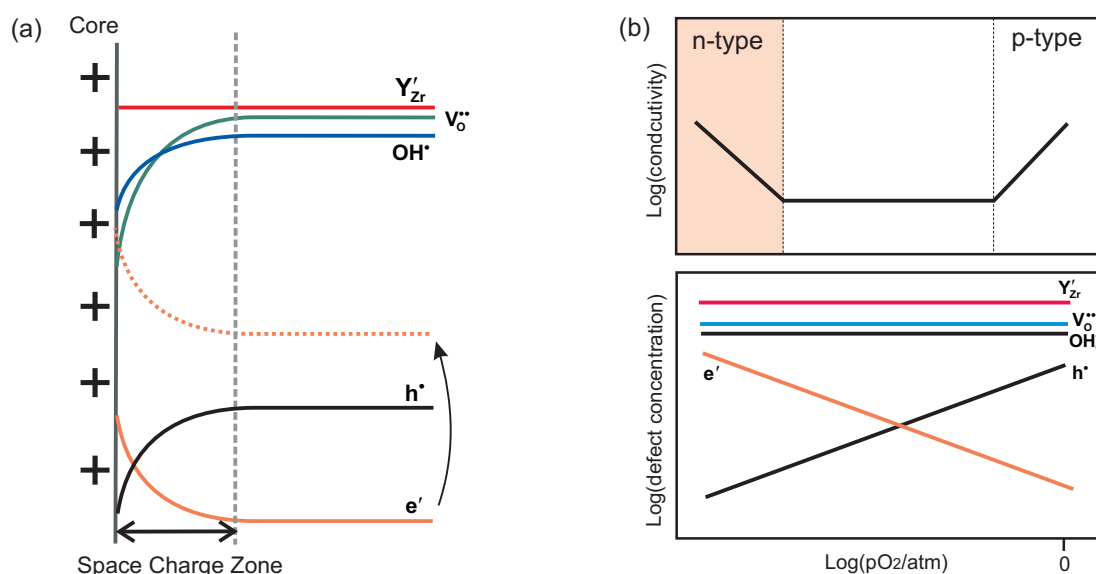


Figure 50 (a) Space charge model; Electron accumulation in space charge layers due to the positive charge of GB core (b) high population of electrons at low oxygen partial pressures

However, due to the low concentration of electrons, this effect is not visible at oxygen partial pressures of 1 to 10^{-4} atm (**Fig. 50-b**). Thus, if the concentration of electrons is increased by applying very low pO_2 , the GB should become at least nonblocking or even highly conductive. As already shown, SPS-6YBZ exhibits an extremely large grain boundary resistivity at low temperatures at $pO_2 = 10^{-4}$ atm, which is at low temperatures even difficult to be measured using available AC-impedance analyzers (**Fig. 51**). The bulk exhibits p-type conductivity in the pO_2 range of 1 to $\sim 10^{-5}$ atm, and at lower partial pressures becomes ionic (**Fig. 55**). At the lowest possible oxygen partial pressure using CO/CO₂ mixtures, the sample is still in the ionic regime. To apply even lower oxygen partial pressures, a layer of metallic Zr (300-500 nm) was deposited on the sample. During annealing under vacuum at 800°C, the metallic layer

extracts oxygen from Y-doped BaZrO_3 ($\text{Zr} + 2\text{O}_\text{O}^\times \rightarrow 2\text{V}_\text{O}^{\bullet\bullet} + 4\text{e}' + \text{ZrO}_2$) and creates conduction electrons which correspond to producing either Zr^{+3} or Y^{+2} in the system.

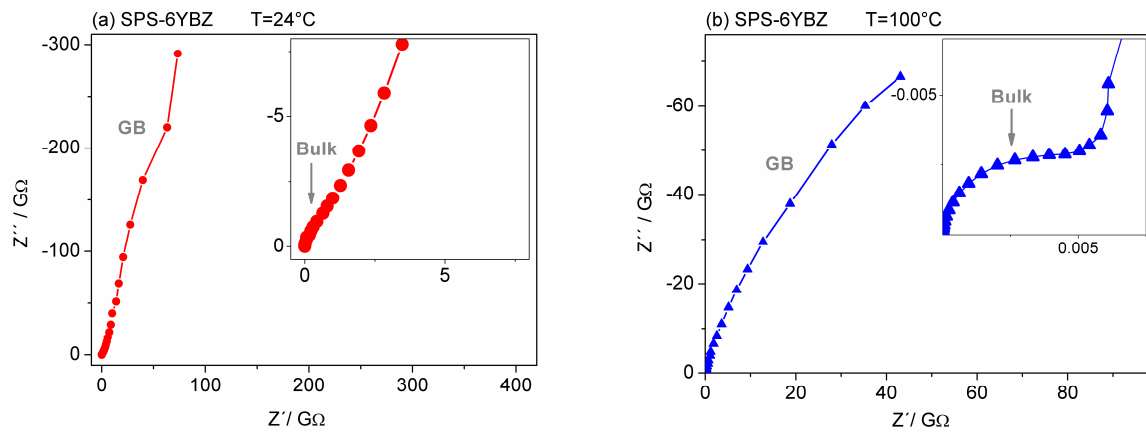


Figure 51 Blocking grain boundaries in 6 at.% Y-doped BaZrO_3 in dry N_2 at (a) 24°C and, (b) 100°C , $C_b \approx 30$ pF and $C_{\text{GB}} = 10$ nF.

The annealed sample after removing the oxidized zirconium layer, has changed from white to black due to the high conduction electron concentration in the material (**Fig. 52**). Similar color changes are known for reduced TiO_2 and SrTiO_3 , and YSZ after applying a large DC bias.

Reduced samples have to be measured under dry conditions (preferably under vacuum) to avoid oxidation by water molecules ($\text{Zr}'_{\text{Zr}} + \text{OH}_\text{O}^\bullet \rightarrow \text{Zr}^\times_{\text{Zr}} + 1/2\text{H}_2 \uparrow + \text{O}^\times_\text{O}$).

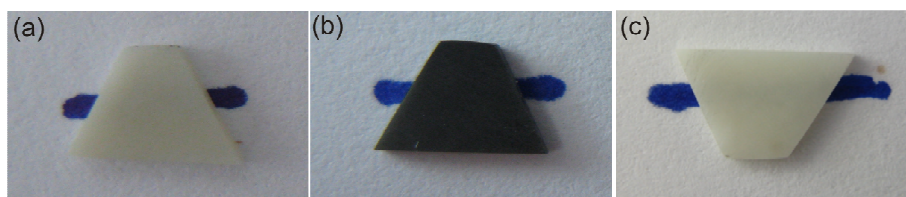


Figure 52 SPS-6 at.% Y- BaZrO_3 (a) before reduction (b) after reduction and removing the oxidized Zr layer (c) after re-oxidation

The AC impedance spectra of the black-reduced sample at room temperature in **Fig. 53-a** exhibit only one semicircle. A second semicircle starts appearing at 250°C and by time becomes larger (**Fig. 54-b**). The capacity of the second semicircle is 2 orders of magnitude higher than of the first semicircle ($C_1 = 10^{-10}$ F, $C_2 = 10^{-8}$ F). The capacitance of blocking grain boundaries in SPS-6 at.% Y- BaZrO_3 is in the range of 10 nF. The temperature of 250°C is too low to reach the final equilibrium state and after more than 100 hours, the second

semicircle is still increasing slowly. After oxidizing the sample in dry N_2/O_2 at $700^\circ C$, the impedance spectra of the sample exhibits again two semicircle and the color of the re-oxidized sample changes back to white (**Fig. 52-c**). The reduction reaction is reversible and no phase decomposition was observed by XRD. In addition, the annealing temperature is too low to expect cation diffusion (dopant segregation), therefore the reduction has only increased the concentration of conduction electron in the material.

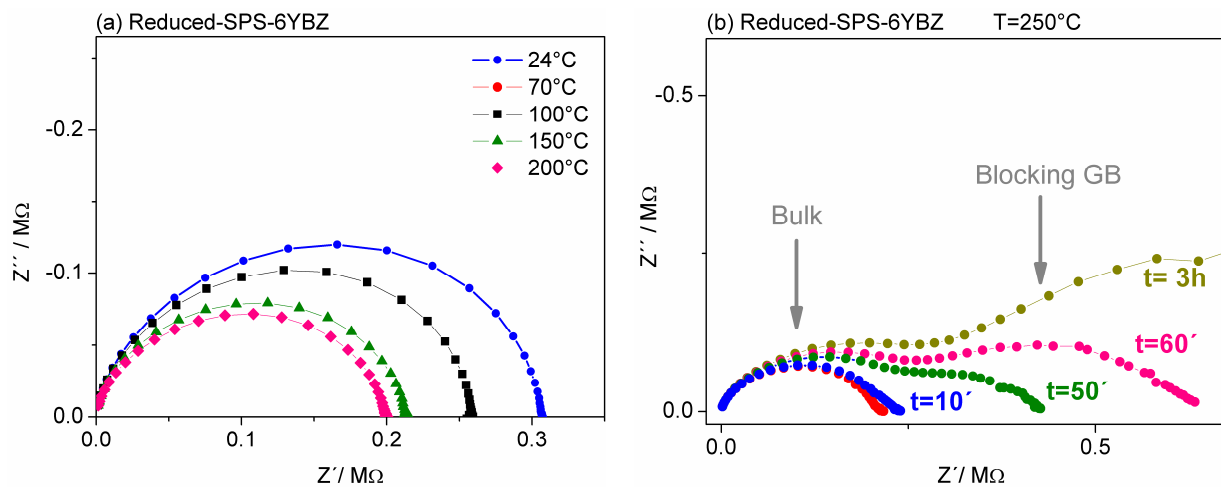


Figure 53 (a) Absence of blocking grain boundary in reduced sample (Zr layer : 500 nm) and (b) re-appearance of blocking contribution with time at $250^\circ C$ in N_2 with $pO_2 \approx 10^{-4}$ to 10^{-5} atm

The extra electrons in the polycrystalline sample can play different roles at different locations, shown in **Fig. 54**. Here extreme cases are considered to verify contribution of different mechanisms to the observed single semicircle ($C = 35 \text{ pF} \approx C_{\text{bulk}}$):

(I) Vanishing of the blocking GB semicircle could easily be explained by the change of the bulk to n-type electronic conduction with nonblocking accumulation layers at the “perpendicular” GBs still having a positive core charge (**Fig. 50-a**).

(II) Similar to (I), electrons are formed inside the grains, but their accumulation in space charge zone results in short-circuiting through a path parallel to the grain boundaries with high electron concentration. Nevertheless, due to the relatively low grain boundary density (grain size $\sim 500\text{-}1000 \text{ nm}$), this case is less probable.

(III) Accumulation of electrons in the core could form highly conductive GB cores parallel to the current while the bulk resistivity remains unchanged. Again, due to the low GB density this is less probable.

(IV) The absence of blocking GBs can be due to formation of the electrons in the core and completely annihilating the positive core charge. In this situation, no extra electrons would be required in the bulk to remove the blocking GB semicircle. Since the measured resistance of reduced sample is smaller than the oxidized sample, this mechanism cannot be the only reason for absence of blocking GBs in the reduced sample.

Therefore, case II and III has less probability and either electron accumulation in the space charge zone (I) or in the core (IV) are regarded as most probable; both of which confirms space charge model.

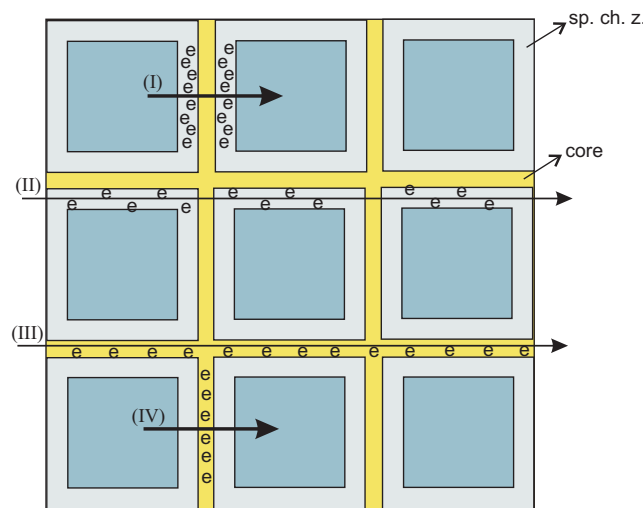


Figure 54 Possible locations for produced extra electrons in the polycrystalline material

According to equilibrium reaction of zirconium oxidation ($\text{Zr} + \text{O}_2 \rightleftharpoons \text{ZrO}_2$; $\Delta G_{800^\circ\text{C}} = -875$ kJ/mol), the oxygen partial pressure at the annealing temperature is about 10^{-42} atm. Therefore, reducing Y-doped BaZrO_3 using the metallic layer of Zr can be seen as exposing the sample to extremely low oxygen partial pressures ($\geq 10^{-42}$ atm). In addition, using different thickness of Zr layer allows producing different conduction electron concentrations in the system which leads to different total resistivity of the sample. The variation in the thickness of film can be assumed as different oxygen partial pressures, which cannot be precisely quantified. The Arrhenius plots of oxidized samples at different oxygen partial pressure in the $p\text{O}_2$ -independent regime (**Fig. 56-a**) show activation energies of ~ 0.65 eV and ~ 1.1 eV for bulk and GBs, respectively. This large E_a is a typical value for ionic conduction ($V_O^{\bullet\bullet}$). On the other hand, the reduced samples show a very low activation energy below 0.1 eV (**Fig. 56-b**) which could be assigned to electron migration in the conduction band.

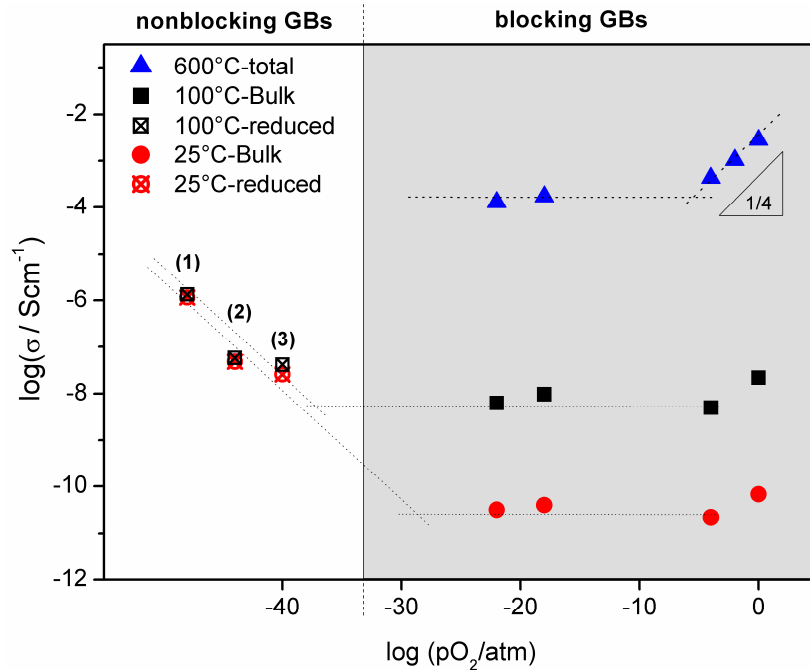


Figure 55 Conductivity of 6% Y-doped BaZrO_3 at different oxygen partial pressures at 100°C and 600°C, (1), (2) and (3) are reduced samples using Zr layer of 500, 400 and 300 nm, respectively. All measurements were performed in dry conditions. It should be mentioned that at low temperature the samples are not in equilibrium and exhibit a frozen defect concentration from higher temperatures.

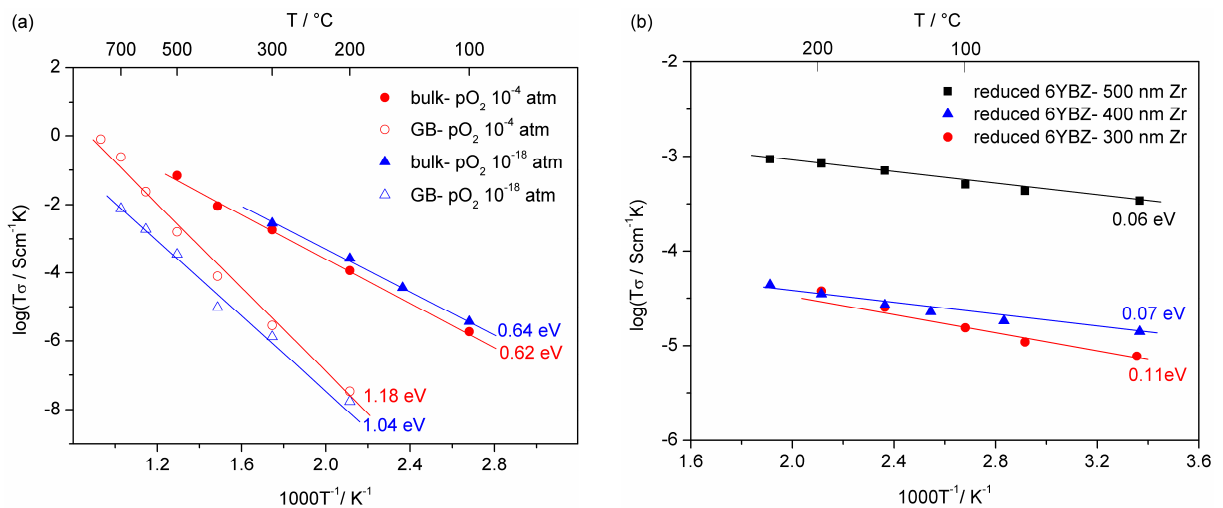


Figure 56 Arrhenius plots of (a) oxidized sample at different oxygen partial pressures and (b) reduced sample using different thickness of Zr layer

1.9 Nonlinear electrical properties of grain boundary

The electrical behavior of grain boundaries under DC-bias can be used to directly test the validity of the space charge model^[93-98]. The simulated dependence of GB conductivity on DC-bias for a p-type SrTiO₃ bicrystal^[98] is in agreement with actual measurements^[158] and has successfully explained the experimentally observed behaviour of space charge layers. In acceptor-doped BaZrO₃, similar to other nominally undoped and acceptor-doped perovskite oxides^[46], the conduction electron concentration is very low and main charge carriers in dry conditions are holes and oxygen vacancies. Thus, a similar nonlinear behavior is expected in this material if a space charge model applies.

The potential barrier at the grain boundary of Y-BaZrO₃ is derived to be in the range of 0.4 V to 0.68 V. To observe a GB response to the applied bias, the DC-bias per single GB should necessarily be comparable or larger than the GB potential barrier^[98]. A polycrystalline sample with a grain size of 500 nm and thickness of about 0.5 mm contains 1000 grain boundaries and even if a DC voltage of 10 V on the sample is applied, each GB can only feel only ~ 5 mV which is much smaller than the GB potential barrier. In this case, even if a nonlinear current-voltage behaviour is observed, it cannot convincingly indicate the presence of space charge layers. Recently, Iguchi et al.^[140] observed a small decrease of the GB semicircle upon increasing the AC amplitude up to 2.5 V on a polycrystalline sample. Since the applied amplitude over each GB is lower than 1mV the interpretation with respect to GB space charge zones has to be discussed critically. Applying a reasonable amount of bias over each grain boundary becomes possible with (i) using microelectrodes and measuring the conductivity of individual grain boundaries, which requires grains larger than 20 μm or (ii) preparing a sample with large grains, containing a few grain boundaries in a reasonable sample thickness for conductivity measurement in a conventional cell. Thus, it was intended to prepare ceramics with rather large grains ($\geq 100 \mu\text{m}$) which allows using microelectrodes of 20 μm for measuring impedance spectra of individual grain boundaries. As a consequence of the bad sintering properties and of the high melting point of BaZrO₃ (2600°C), conventional preparation methods are not able to produce a material with sufficiently large grains. Therefore, the optical floating zone technique (Infrared Image Furnace), which is commonly applied to grow single crystals, and features high temperatures exceeding 2800°C, was used to produce large-grained samples of YBZ.

During annealing in the infrared image furnace, there is a temperature gradient from bottom to top part of the rod. The bottom part has seen the maximum temperature, very close to or even exceeding the melting point of BZ, however, the upper part of the rod is annealed at lower temperatures. This inhomogeneous condition leads to different compositions and microstructures along the rod. X-ray diffraction analysis, orientation imaging microscopy and ICP-OES analysis were used to characterize different parts of the annealed rod.

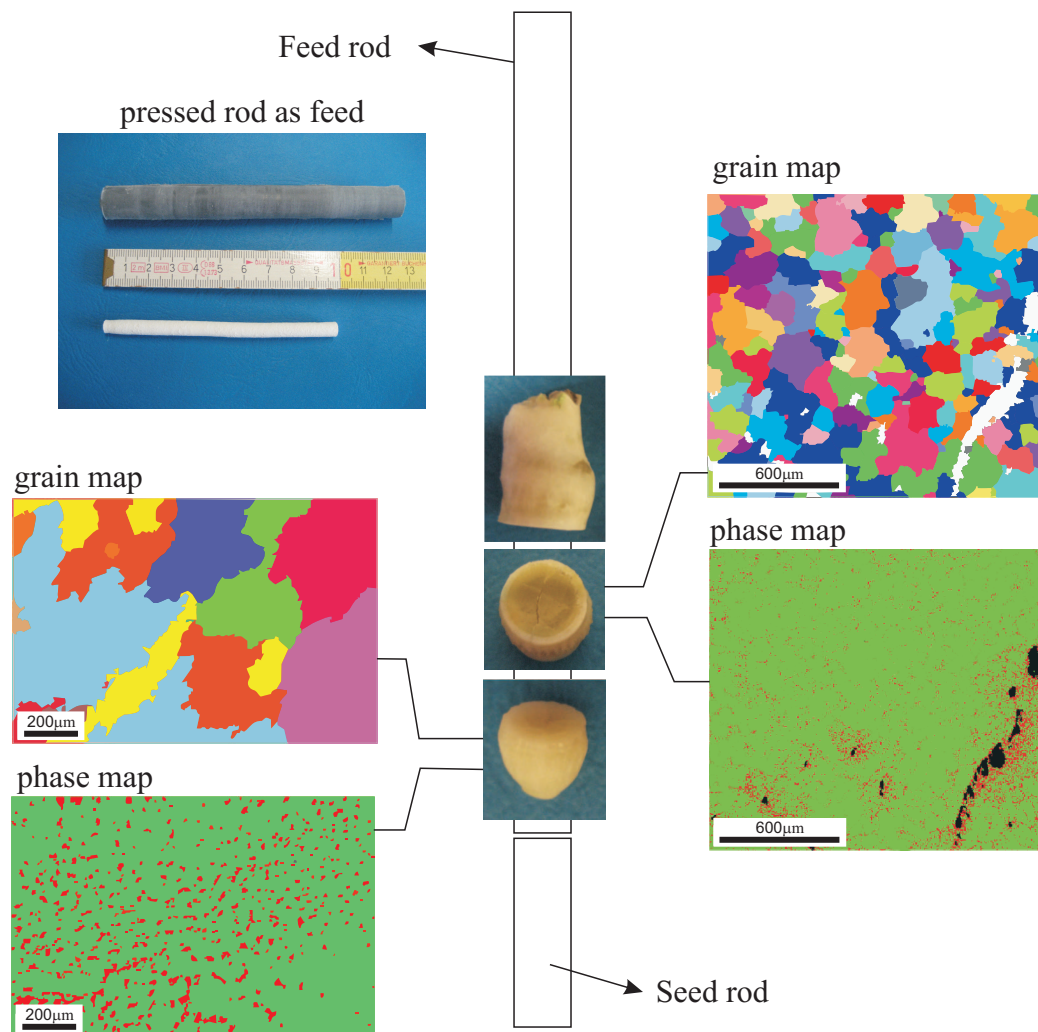


Figure 57 The feed rod pressed in a soft mold using isostatic press and the sample prepared in image furnace. Grain map and phase map from lower and upper parts; in phase map green color is Y-doped BaZrO₃ and red area refers to ZrO₂

According to the grain and phase maps shown in **Fig. 57**, the bottom part with extremely large grains contains more than 10% of secondary zirconia phase. The large amount of barium evaporation, which was detected during image furnace annealing, can cause this large amount

of zirconia phase. The upper parts, annealed at lower temperatures, exhibit a smaller grain size ($\sim 200 \text{ nm}$) and a lower amount of secondary phase. A higher ZrO_2 concentration is observed close to the pores and cracks, which are the areas with more barium loss. Nevertheless, most ZrO_2 (particle diameter: $4\text{--}8 \text{ }\mu\text{m}$) is formed within the grains and the effect of this secondary phase on the conductivity behavior of GB can be ignored in first approximation.

The bottom part of the annealed sample is crystallographically more oriented than the upper part (**Fig. 58**) and exhibits a smaller lattice constant due to a smaller amount of yttrium substitution.

As already shown, the unit cell size of conventionally sintered Y-doped BaZrO_3 , at least up to 10 at.% Y dopant, increases linearly with dopant concentration. Therefore, the yttrium concentration can roughly be estimated from the lattice parameters in the different parts of the annealed rod. This estimation is valid when lattice shrinkage due to Y substitution in Ba site (resulting from BaO loss) is negligible. The ICP-OES chemical analysis of a middle slice was in a good agreement with the estimated dopant concentration from unit cell size (**Fig. 59**). This suggests a negligible amount of Y in zirconia phase and indicates that at $T = 2600^\circ\text{C}$ not only barium but also some yttrium is lost by evaporation.

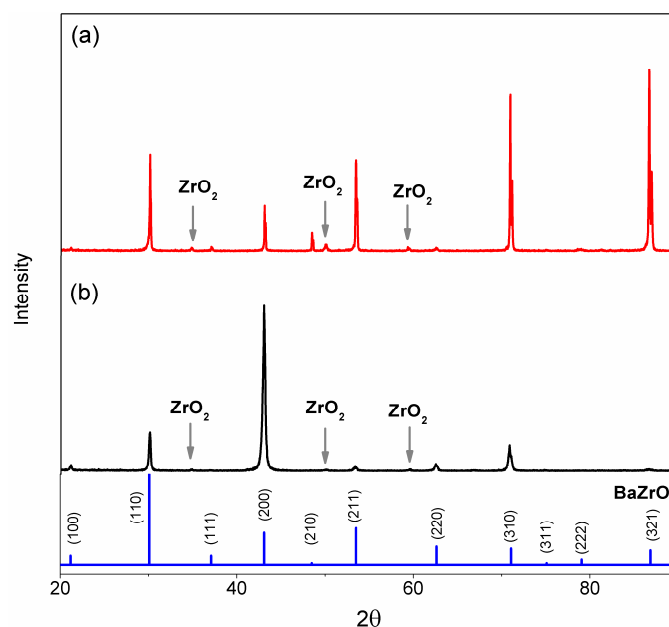


Figure 58 X-ray diffraction pattern of large grain sample prepared in image furnace, Y-doped BaZrO_3 and ZrO_2 phases in (a) bottom part and (b) middle part. The different peak intensity patterns in YBZ are due to the large grain size preventing a proper averaging over all grain orientations.

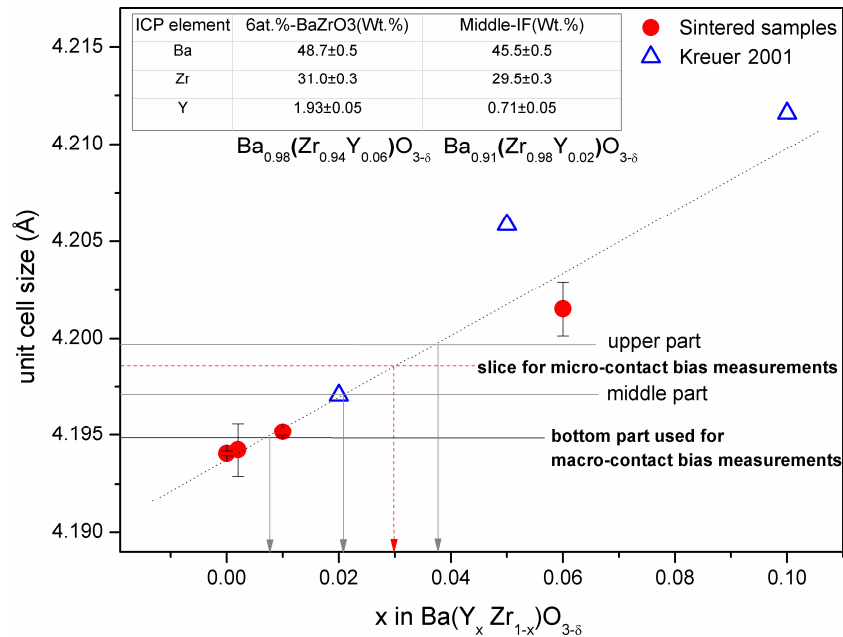


Figure 59 Unit cell size of Y-doped BaZrO_3 in different parts of the image furnace sample compared to conventionally sintered samples with different dopant concentration. The table shows the ICP elemental analysis of 6 at.% Y-doped BaZrO_3 and the middle part of the image furnace rod

The slice used for micro-contact measurements, with a unit cell size of 4.1985 Å contains about 3 at.% yttrium and the one used for macro-contact bias measurements contains lower than 1 at.% yttrium.

A relatively thin slice ($\sim 800 \mu\text{m}$) of the large-grained sample (bottom part) with 3-5 grain boundaries offers the possibility of applying a perceptible DC bias over each grain boundary (up to $\sim 2 \text{ V}$ per each GB). At zero bias, the impedance spectra exhibit three semicircles, corresponding to the bulk, GBs and electrode in order of decreasing frequency (**Fig. 60**). A DC-voltage of 0.5 to 10 V was applied at each temperature. The effective bias over one grain boundary^[94] is $U_{\text{dc}}R_{\text{GB}}/N_{\text{GB}}(R_{\text{b}}+R_{\text{GB}}+R_{\text{electrode}})$. Since after applying the first 0.5 V bias, the electrode semicircle disappears and also bulk resistivity is negligible compared to the GB resistivity, the applied bias over each GB is equal to $U_{\text{dc}}/N_{\text{GB}}$. With the effective bias of about 0.1 V to 2 V, the GB semicircle becomes significantly smaller. **Fig. 61** shows the behavior of resistance and capacitance with the applied DC bias at two different temperatures. Bulk resistance and capacitance are almost unchanged. The GB resistance decreases with the applied bias and in other words the sample exhibits a nonlinear current-voltage characteristic.

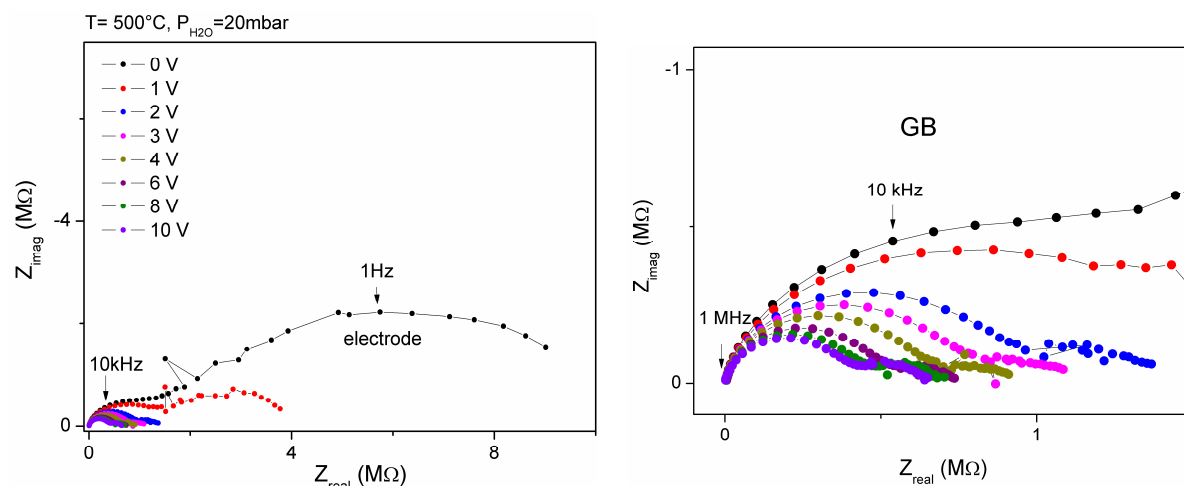


Figure 60 AC impedance spectra of large-grained Y-doped BaZrO₃ in wet O₂/Ar under DC bias from 0 to 10 V at 500°C

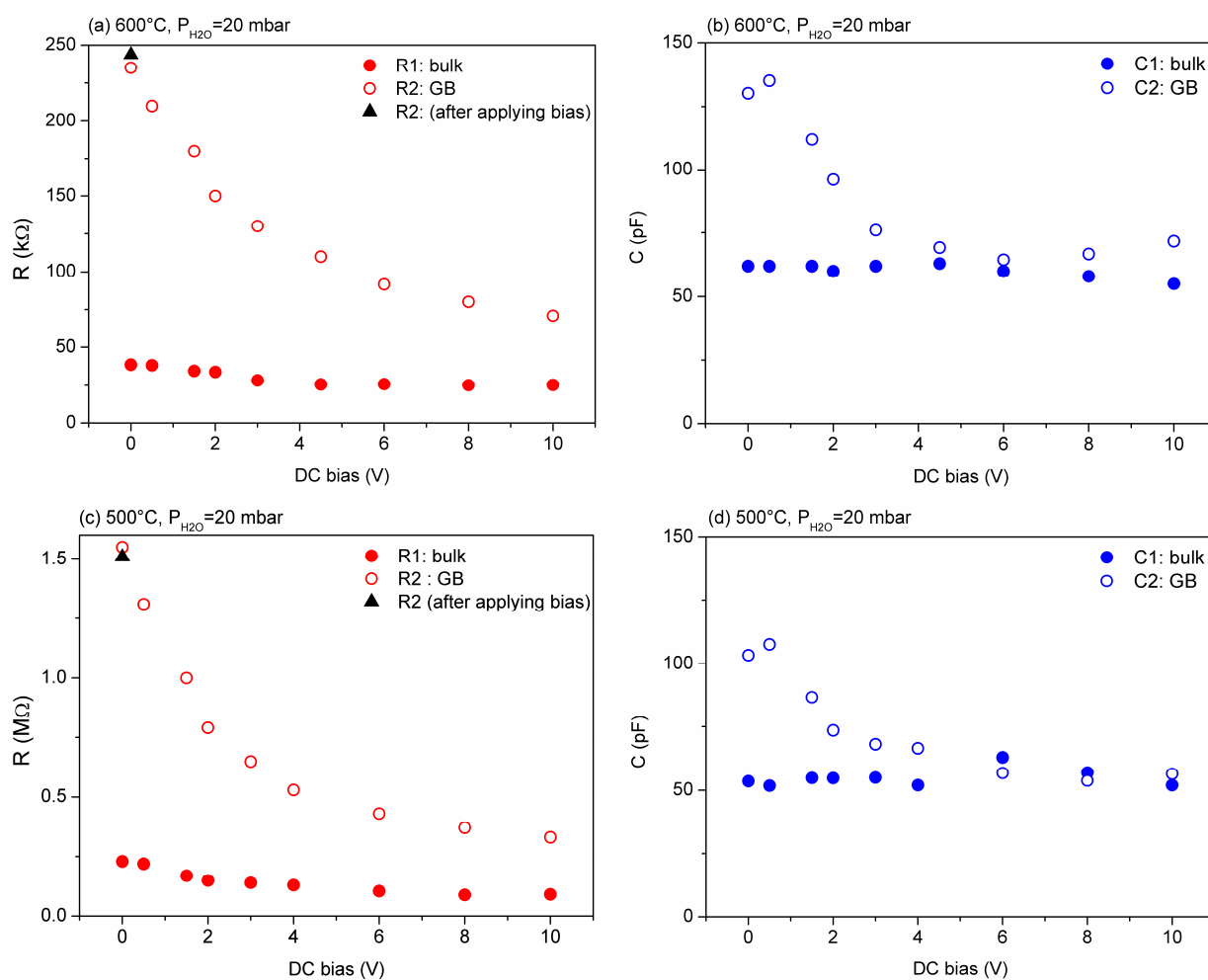


Figure 61 DC bias dependence of bulk and GB resistance and capacitance at (a,b) 600°C and (c,d) 500°C in large grained sample (IF-YBZ-bottom part) using macroscopic electrodes

Furthermore, the GB capacitance is slightly bias dependent. Both effects together can be considered as an indication for presence of space charge layers near the crystallographic GB. One has to note that C_{GB} (no bias) is slightly larger than C_b , while according to the brick layer model a large difference ($\sim d_g/d_{GB}$) would be expected. This discrepancy, which is more pronounced for the bottom part, might be due to the presence of some cracks.

1.9.1 Electrical properties of individual GBs in large grained sample

The achieved large grain size of about 200 μm in the image furnace sample is very suitable for investigating individual grain boundaries by microcontact impedance measurements. Applicability of microelectrodes for grain boundary characterization in polycrystalline ceramics, its potentials and limits have been already discussed^[97, 159]. This method has the advantage to assess electrical behavior such as bias dependence of individual grain boundaries. It needs to be considered that when a few GBs are much more blocking than the others, they may appear as “normal blocking” GBs due to current detour. Also there is an inherent uncertainty in the estimated GB area since only the cross-section of the surface is visible. Therefore, one should be cautious about correlating particular orientations of GBs to their electrical properties.

The applied microelectrodes of 20 μm diameter inside the grains and Pt/Ir tips for contacting the microelectrodes are shown in **Fig. 62**.

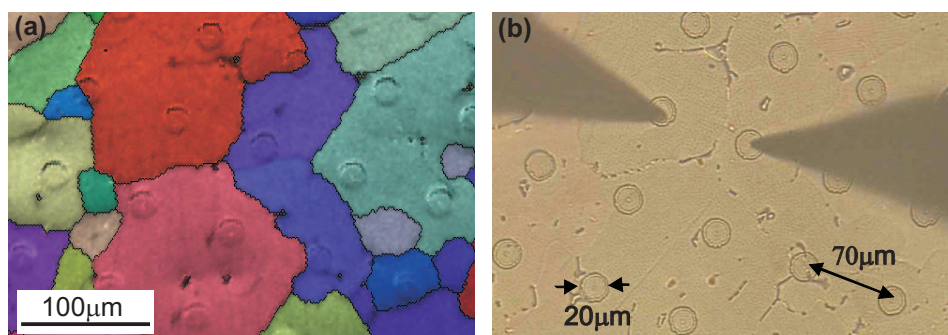


Figure 62 (a) Grain map combined with SEM image of microelectrodes and (b) positioning the tips on microelectrodes under the optical microscope in conductivity measurement setup.

Each AC-impedance spectrum inside a grain exhibits only one semicircle assigned as bulk contribution. The spectrum measured across a GB exhibits two semicircles from high to low

frequencies for bulk and GB, respectively (**Fig. 63**). The Bode plots (**Fig. 63-b**) clearly show the difference between the two measurements inside a grain and across a GB. **Fig. 64-b,c** displays resistivities obtained by measurements inside the grains (R_1) and across the GBs (R_1 and R_2) at different locations. The resistivity of the first semicircle measured inside the grains is comparable with the first semicircle from the measurements across the GBs. Although there is a slight scatter in the data, the GB resistivity, which is significantly (1-2 orders of magnitude) higher than bulk, can be recognized.

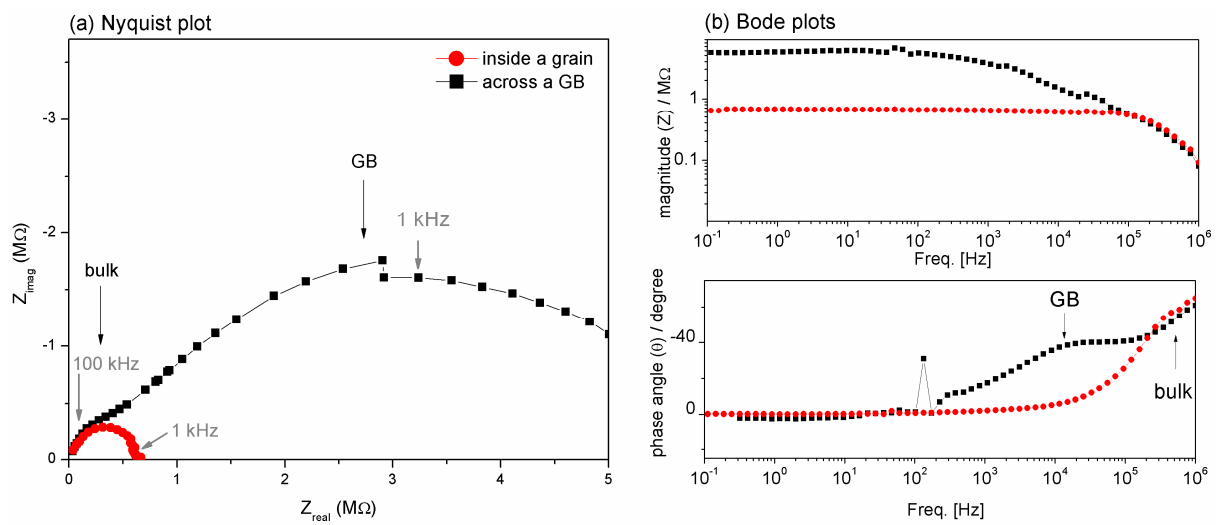


Figure 63 AC impedance spectroscopy using microelectrodes inside and across a GB (a) Nyquist and, (b) Bode plots at 700°C

As expected due to the different activation energies, the difference between bulk and GB resistivity at 500°C is higher than at 700°C.

R_2 , assigned as R_{GB} , shows a relatively smooth distribution which, as it was mentioned, does not exclude the possibility of some particularly strongly blocking grain boundaries. The bulk and grain boundary conductivities were calculated using^[97, 159]

$$\sigma_{\text{bulk}} = \frac{1}{R_1 \cdot d} \quad (31)$$

$$\sigma_{\text{GB}} = \frac{\gamma_{\text{corr}} \cdot \epsilon}{f_R \cdot R_2 \cdot C_2} \quad (32)$$

where R_1 and R_2 are the resistivities of first and second semicircles, d is the microelectrode diameter (20 μm) and C_2 is the capacitance of second semicircle. f_R and γ_{corr} are the correction factors due to the contribution of neighboring GBs to the resistance and capacitance,

respectively. As long as GBs are strongly blocking, f_R can be regarded as 1. γ_{corr} depends on the microstructure of the sample and according to Ref.^[159] a value of 3 has been taken here for γ_{corr} .

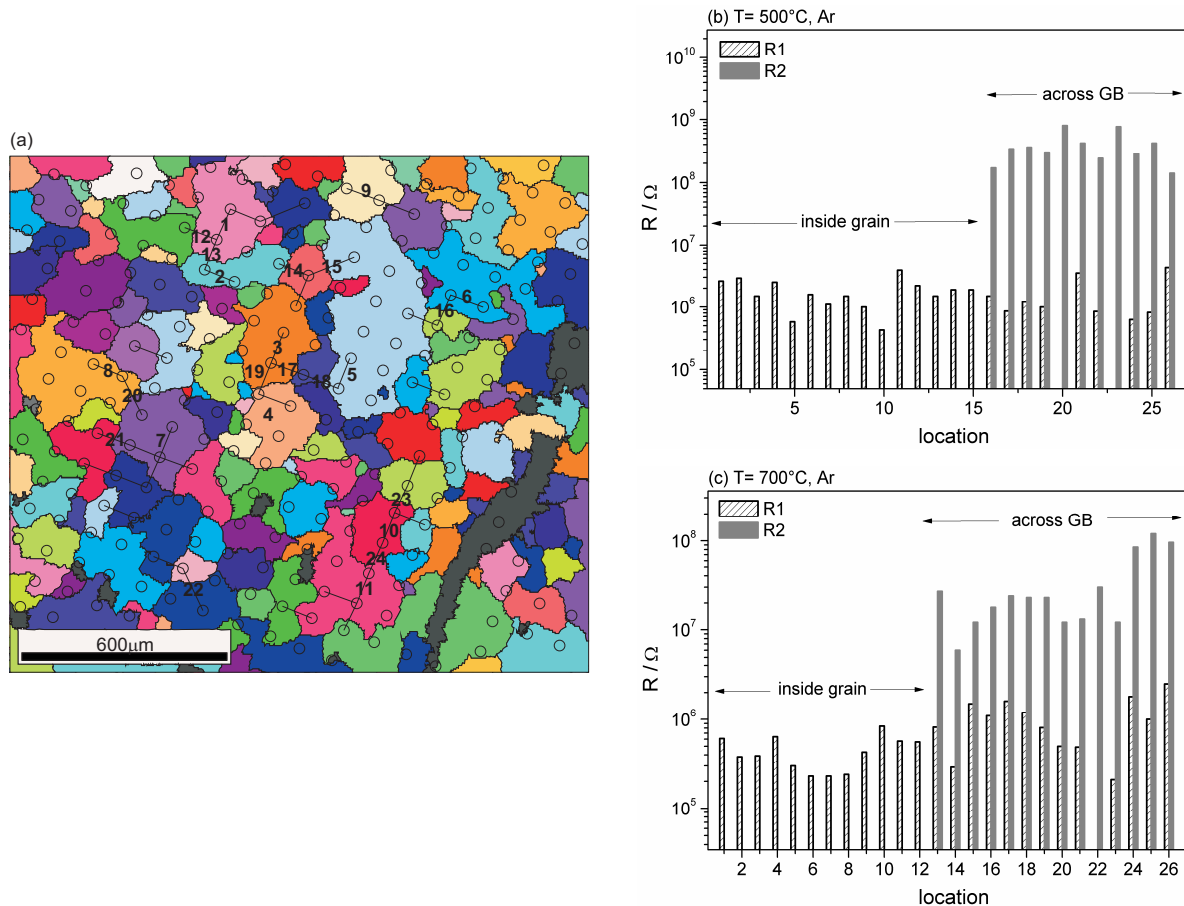


Figure 64 (a) Grain map of image furnace sample (middle slice); circles show the place of microelectrodes and numbers are the locations of conductivity measurements. Resistivity of first (R_1) and second (R_2) semicircles at (b) 500°C and (c) 700°C

In order to demonstrate the applicability of the method for polycrystalline Y-doped BaZrO_3 , the estimated bulk and grain boundary conductivity and their dependence on temperature were compared to the macroscopic impedance spectroscopy data of the sample (**Fig. 65**). The average bulk conductivity is very close to the measured conductivity of IF-YBZ using macroscopic electrodes in the conventional sample holder. The activation energy is also comparable to that of the bulk of polycrystalline Y-doped BaZrO_3 . The lower bulk conductivity of the large grain sample, in both micro- and macro- electrode measurements,

compared to polycrystalline 6 at.% Y-BaZrO₃ is due to the lower effective yttrium concentration in IF-YBZ (lower actual Y, and possibly some Y_{Ba}^{\bullet}).

Lacking a reliable C_b , the specific GB resistance for the macroscopic measurement is approximately calculated from R_{GB} , an assumed number of 20 GB within the sample thickness of 2 mm and the total GB depletion width of 20 nm estimated from the microcontact impedance. As shown in **Fig. 65**, the average conductivity and E_a of GBs from microcontact measurements are comparable with the values obtained by macroscopic electrodes.

The relatively high resistivity of bulk and grain boundary, the reasonable bulk conductivity values and activation energies that are comparable to Y-doped BaZrO₃ indicate that the microcontact measurements are not affected by a highly conductive surface layer^[160] or even artifacts from e.g. incomplete etching of the Pt layer in the lithography process.

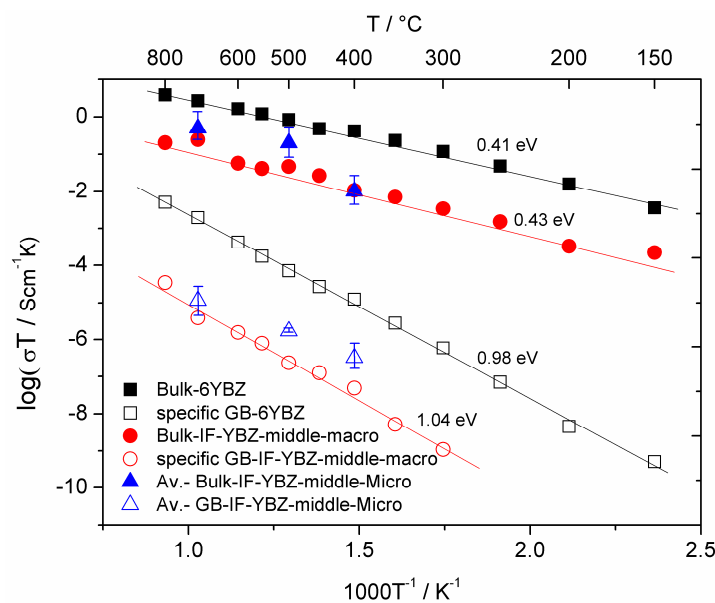


Figure 65 The average conductivity of bulk and GB using microelectrodes in comparison with the measured data on large grain sample (IF-YBZ-middle part: 2 mm thick) using macroscopic electrodes and CS-6YBZ

As a next step, the DC-bias dependencies of bulk and grain boundary resistivities were investigated. As the potential barrier at the grain boundary of Y-doped BaZrO₃ is about 0.4-0.68 V, applying a DC voltage of 0.1-1 V is sufficient to change the defect distribution near a single grain boundary. While the electrode semicircle is negligible in the microelectrode measurements at 700°C, it makes a contribution compared to the GB semicircle at 500°C (even with a rather similar capacitance due to the fact that only a single GB is measured). The

comparison with the image furnace macroscopic sample shows that the electrode semicircle decreases much more strongly under bias than the GB semicircle. On applying a DC bias of 0.2 V, the electrode semicircle disappears (**Fig. 66**) and the grain boundary semicircle shrinks.

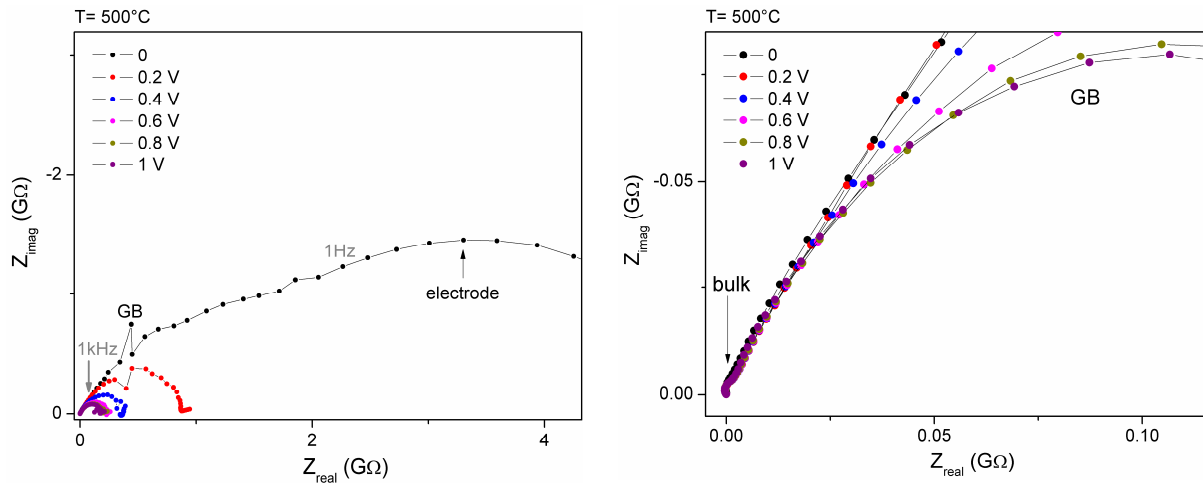


Figure 66 Impedance spectra and bias dependence of second and third semicircle across a grain boundary

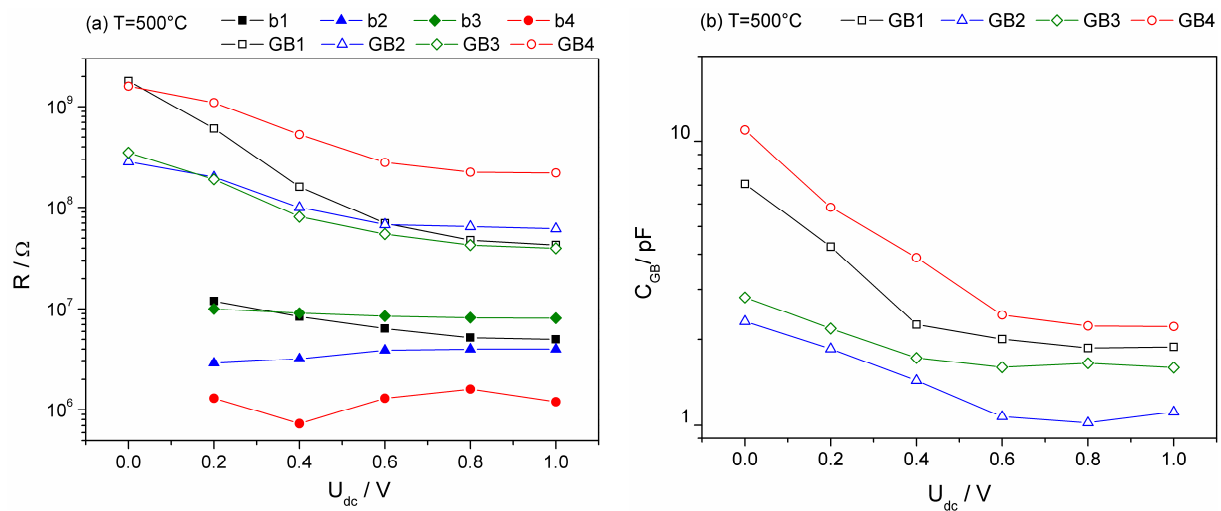


Figure 67 (a) Resistance of bulk (solid symbols) and grain boundary (open symbols) and (b) GB capacity as a function of DC-bias at 500°C, collected from two microelectrodes in neighbouring grains.

The bulk semicircle is very small compared to GB and does not change perceptibly with the applied bias. The DC-bias dependence of bulk and grain boundary resistances for different grain boundaries is plotted in **Fig. 67-a**. The bulk resistance remains unchanged with the applied bias; however, grain boundary resistance depends considerably on the applied DC bias.

C_2 , assigned as GB capacitance, moderately decreases with applied DC-bias (**Fig. 67-b**). This decrease is observed for most of the measurements at different measurement positions. Due to difficulties in finding suitable microelectrodes and other practical limitations there are not sufficient data to give a statistics, but the results provide enough confidence about the electrical behavior of GBs in response to the applied DC-bias.

The nonlinear I-U character of GB has been attributed to either existence of a secondary layer at the GB or presence of space charge layers^[98, 161-163]. It was however assumed that when insulating layers have a bias-dependent resistance, still the capacitance should remain constant with the applied bias. Whilst, in case of space charge layers, the capacitance changes with the applied bias^[162, 163].

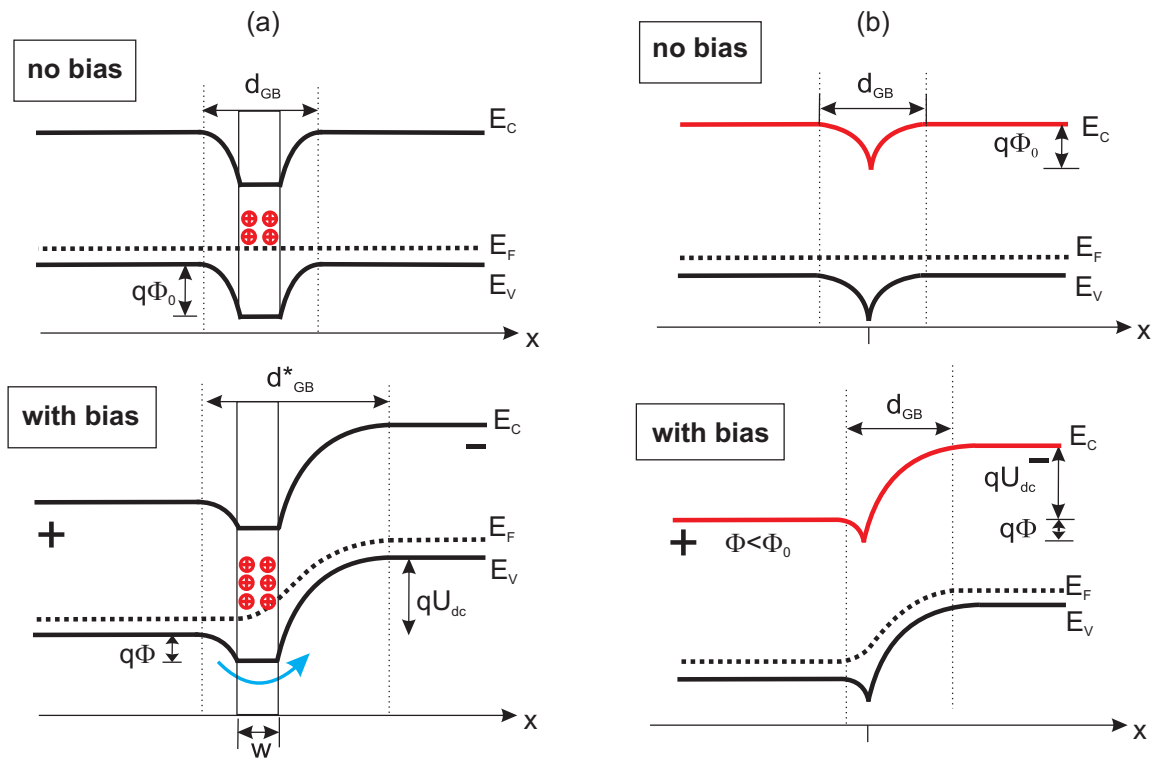


Figure 68 Band structure model for a grain boundary (a) with and (b) without interface state effect in a p-type semiconductor for zero bias and an applied bias across the GB; E_C , E_V and E_F are conduction, valence and Fermi energies, respectively. w is the width of GB core and d_{GB} refers to the total width of GB (core and depletion layers).

The Schottky model^[161, 164] with and without interface state effect is discussed to explain the GB electrical properties, in particular capacity, of Y-doped BaZrO₃ with the applied bias. Fig. 68-a shows the band structure of a GB^[161, 164] with some occupied interface states which are

bias dependent. On the other hand, **Fig. 68-b** shows the GB band model^[98] when the interface states are completely unoccupied and therefore the interface charge is independent of the applied bias.

In the model with interface states (**Fig. 68-a**) and within the thermionic emission mechanism, the hole current density (j) across the GB can be expressed by^[161]

$$j = A^* T^2 \exp\left(-\frac{\Phi_0 + E_F - E_V}{kT}\right) [1 - \exp\left(-\frac{qU_{dc}}{kT}\right)] \quad (33)$$

where for p-type semiconductors $E_F - E_V = kT \ln(N_V/N_A)$. A^* is a constant which depends on the effective mass of the material, N_A is acceptor density and N_V is the effective valence band density of states. One should note that the drift-diffusion model of transport in space charge zones^[92] is closer to the behavior of perovskite oxides than thermionic emission. Since the resulting current mainly differs in a temperature-dependent prefactor, at a constant temperature the general trend would be the same.

The nonlinear current-voltage behavior at a given temperature (**Fig. 69**) can be decomposed into three regimes^[161, 165]:

(I) For low voltage ($1 - \exp(-qU_{dc}/kT) \approx qU_{dc}/kT$), Φ is constant and j shows an ohmic behavior with applied bias according to

$$j = A^* T^2 \exp\left(-\frac{\Phi_0 + E_F - E_V}{kT}\right) \left(-\frac{qU_{dc}}{kT}\right) = \alpha U_{dc} \quad (34)$$

(II) At intermediate voltage ($1 - \exp(-qU_{dc}/kT) \approx 1$), Φ is constant and j is independent of the applied bias and exhibits a quasi-saturated behavior. This region becomes less visible by increasing dopant concentration and disappears in highly doped materials.

$$j = A^* T^2 \exp\left(-\frac{\Phi_0 + E_F - E_V}{kT}\right) \quad (35)$$

(III) At sufficiently high voltage ($1 - \exp(-qU_{dc}/kT) \approx 1$), the potential barrier decreases according to

$$\Phi(U) = \frac{1}{4} U_0 \left[1 - \frac{U_{dc}}{U_0}\right]^2 \quad \text{where } U_0 = \frac{Q_i^2}{2\epsilon\epsilon_0 q N_0} \quad (36)$$

This drop of the barrier is accompanied by a rapid increase in current according to

$$j = A^* T^2 \exp\left(-\frac{\Phi(U) + E_F - E_V}{kT}\right) \quad (37)$$

The applied bias (U_{dc}) brings the Fermi level in the GB core closer to the valence band edge (**Fig. 65-a**) and thus increases the interface charge (Q_i). This increases the total width of the depletion zone (d^*_{GB}) as $d^*_{GB} = Q_i/qN_0$ ^[166, 167]. Such an increase in depletion width decreases

the capacitance. The relation between capacitance (C) and applied bias^[168] can be expressed as

$$\left(\frac{1}{C} - \frac{1}{2C_0}\right)^2 = \frac{2}{q\epsilon\epsilon_0 N_0} (\Phi_0 + U) \quad (38)$$

$$C_0 = \frac{\epsilon\epsilon_0}{d_{GB}^*} = \frac{\epsilon\epsilon_0 q N_0}{Q_i} = \left(\frac{q\epsilon\epsilon_0 N_0}{2\Phi_0}\right)^{1/2} \quad (39)$$

This condition holds below a certain bias, in which the hole interface states play the dominant role and electrons as minority carriers can be neglected^[169].

The other transport mechanism through the barrier is electron tunneling. The tunneling current^[170] depends also on the applied voltage according to Fowler-Nordheim equation ($j = AU^2 \exp(-B\Phi^{3/2} / U_{dc})$). However, at high temperatures this mechanism is negligible for oxides^[171, 172].

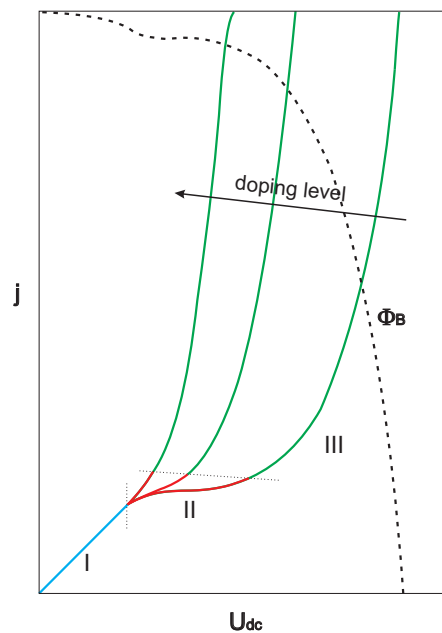


Figure 69 Current-voltage curves for different levels of doping density, simulated by Pike and Seager^[93]

In the model without interface states (**Fig. 68-b**), the nonlinear GB conductivity is similarly described in terms of lowering the barrier^[161]. In this model, the interface charge is assumed to be constant and one would expect a DC-bias independent capacitance for GBs. In spite of that, the simulation of charge transport across the grain boundaries in p-type SrTiO₃^[98] revealed a bias dependence of GB conductivity and capacitance even with constant interface charge (**Fig. 70-a**). The simulated space charge density (**Fig. 70-b**) shows that at intermediate voltages for

which the conductivity increases (varistor behaviour), the total thickness of depletion layers does not change. Only toward higher voltages, the incomplete depletion of oxygen vacancies and the resulting increase of space charge depletion width, leads to a lower GB capacitance. The experimental data on SrTiO₃ bicrystals^[158] also show a moderate decrease of GB capacitance with applying DC-bias in the range of 0.1 to 0.3 V per GB.

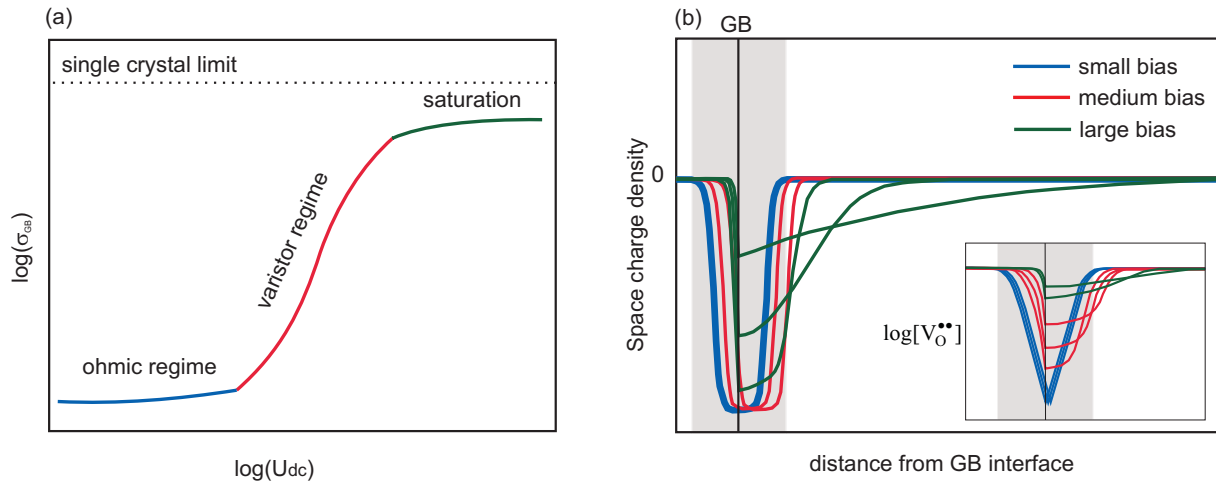


Figure 70 Simulated DC-bias dependence of (a) GB conductivity (b) space charge potential density and oxygen vacancy concentration^[98]

Hopping process as in insulating secondary layers at GB can also cause a bias-dependent behavior^[173]. Applying DC bias lowers the hopping barrier of a single particle transfer to the neighboring site by $\Delta\Phi/2$. The hopping current according to the Butler-Volmer equation is expressed as:

$$j = A \left[\exp\left(-\frac{ze\Delta\Phi}{2kT}\right) - \exp\left(\frac{ze\Delta\Phi}{2kT}\right) \right] \quad (40)$$

For small $e\Delta\Phi/2kT$ values, current is bias independent as $j \propto (ze/2kT)\Delta\Phi$ (ohmic behavior) and for larger $e\Delta\Phi/2kT$ values, where $j \propto \exp(ze\Delta\Phi/2kT)$ a nonlinear I-U character is observed.

In conclusion, the DC-bias dependence of GB conductivity in Y-doped BaZrO₃ very strongly indicates the presence of space charge depletion layers, regardless of the role of interface states. The DC-bias dependence of the capacitance excludes any possible nonlinear I-U characteristics due to an intergranular phase, which is inconsistent with the clean GBs observed by TEM measurements.

1.10 PLD thin films and grain boundary properties

The grain boundary resistivity of a polycrystalline sample is an average value including a variety of grain boundaries. To correlate the grain boundary characteristics and electrical properties it is necessary to investigate a single grain boundary. The high melting point of BaZrO_3 restricts preparation of a well-defined bicrystal. However, bicrystalline substrates can be used to produce single grain boundaries between epitaxial BaZrO_3 films. To reproduce the same pattern as the substrate, with two well-defined orientations, first the conditions of growing an epitaxial layer were optimized.

Growth conditions of epitaxial Y-doped BaZrO_3 and SrZrO_3 films have been reported in some references^[174-182], however nominally identical PLD conditions often yielded different results.

Fig. 71 shows conductivity measurements on 20 at.% Y-doped BaZrO_3 films and compare them with the bulk conductivity of a sintered polycrystalline sample. There are significant discrepancies in the absolute values as well as the activation energies.

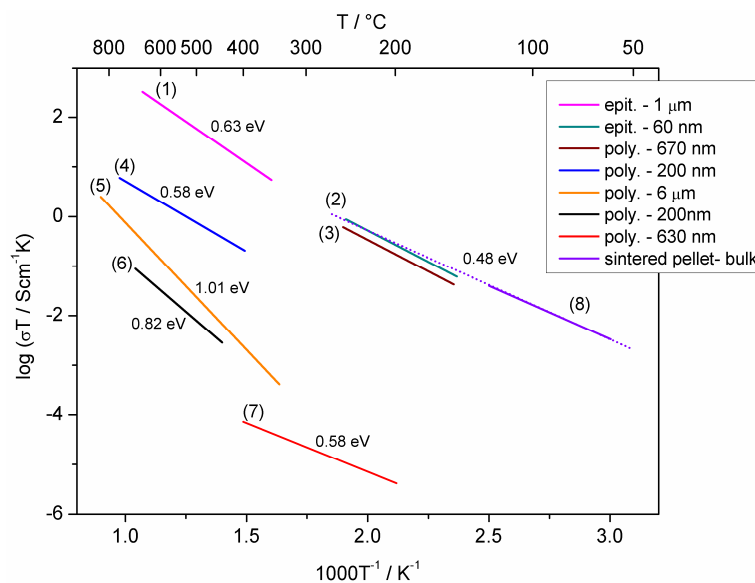


Figure 71 Conductivity of 20 at.% Y-doped BaZrO_3 thin films (1) epitaxial PLD on MgO wet H_2 ^[181], (2) epitaxial PLD on MgO in wet N_2 ^[180], (3) polycrystalline PLD on MgO in wet N_2 ^[180], (4) polycrystalline PLD on Y-doped BaCeO_3 in wet H_2 ^[178], (5) polycrystalline PLD in wet air^[55], (6) PLD on silicon in wet N_2 ^[174], (7) polycrystalline CSD (Chemical Solution Deposition) on silicon in wet H_2 ^[182] and, (8) bulk of sintered pellet in wet conditions.

In this thesis, $\text{BaZr}_{0.85}\text{Y}_{0.15}\text{O}_{3-\delta}$ thin films were deposited on single crystal MgO(100) substrates by pulsed laser deposition (PLD). The good lattice match between $\text{BaZr}_{0.85}\text{Y}_{0.15}\text{O}_{3-\delta}$

($a = 4.20 \text{ \AA}$) and MgO ($a = 4.21 \text{ \AA}$) is essential for epitaxial growth. The deposition conditions for PLD thin films are described in **Table 7**.

Table 7 PLD conditions for thin film deposition

Film	Target	Nominal thickness (\AA)	$T_{\text{substrate}}$ ($^{\circ}\text{C}$)	$p\text{O}_2$ (mbar)	Energy per pulse (J/cm^2)
PLD-15Y-1	SPS-15YBZ	1000	750	10^{-4}	1.6
PLD-15Y-2	SPS-15YBZ	3000	750	10^{-4}	1.6
PLD-15Y-3	SPS-15YBZ	6000	750	10^{-4}	1.6
PLD-15Y-4	SPS-15YBZ	10000	750	10^{-4}	1.6
PLD-15Y-5	SPS-15YBZ	10000	650	10^{-4}	1.6
PLD-15Y-6	SPS-15YBZ	3000	750	10^{-4}	3
PLD-15Y-7	SPS-15YBZ	3000	600	10^{-2}	3

X-ray diffraction patterns of the films (and substrate) are shown in **Fig. 72** (intensity in log scale to emphasize impurity phases if present). The PLD-15Y-1 and PLD-15Y-2 samples are single oriented (100) and PLD-15Y-1 contains a small amount of ZrO_2 . The (100) peak of the two samples is compared to the peak position of the target (15 at.% Y-BaZrO₃) in **Fig. 72-b**. The PLD-15Y-1 peak is shifted to lower 2θ values, but the (100) peak of PLD-15Y-2 is shifted to the higher 2θ values. The peak shift here can be representative of strain effect and/or different lattice size. Since the lattice constant of MgO is slightly smaller than that of 15 at.% Y-BaZrO₃, elongation of the YBZ unit cell perpendicular to the interface seems possible, combined with a compressive strain in lateral direction which shows up as peak shift to lower 2θ values. On the other hand, the smaller unit cell size of PLD-15Y-1 can be due to higher barium loss, yttrium substitution in A-site and lattice shrinkage. The rocking curves of PLD-15Y-1 and PLD-15Y-2 (**Fig. 72-c,d**) for the (100) reflections represent a slight deviation from perfect epitaxial structure. The rocking curve of PLD-15Y-2 shows peak splitting, but the FWHM is smaller than PLD-15Y-1. Increasing the film thickness to 600 and 1000 nm in PLD-15Y-3 and PLD-15Y-4, at the same oxygen partial pressure, substrate temperature and energy, forms multi-oriented films with higher amount of zirconia secondary phase, most probably due to longer deposition time leading to higher barium loss. Deposition on the substrate at lower temperature (650°C) leads to the absence of zirconia, but the film (PLD-15Y-5) is multi-oriented. The film grown with higher pulse energy (PLD-15Y-6) is single-oriented. At a pulse energy of $3 \text{ J}/\text{cm}^2$ and higher $p\text{O}_2$ (10^{-2} mbar), growing an epitaxial layer

with lower substrate temperature (600°C) became possible (PLD-15Y-7). Later the conductivity measurements show that obtaining a crystallographic single oriented film does not give the expected bulk conductivity and other parameters like actual composition and strain might play a decisive role in the electrical properties of thin film.

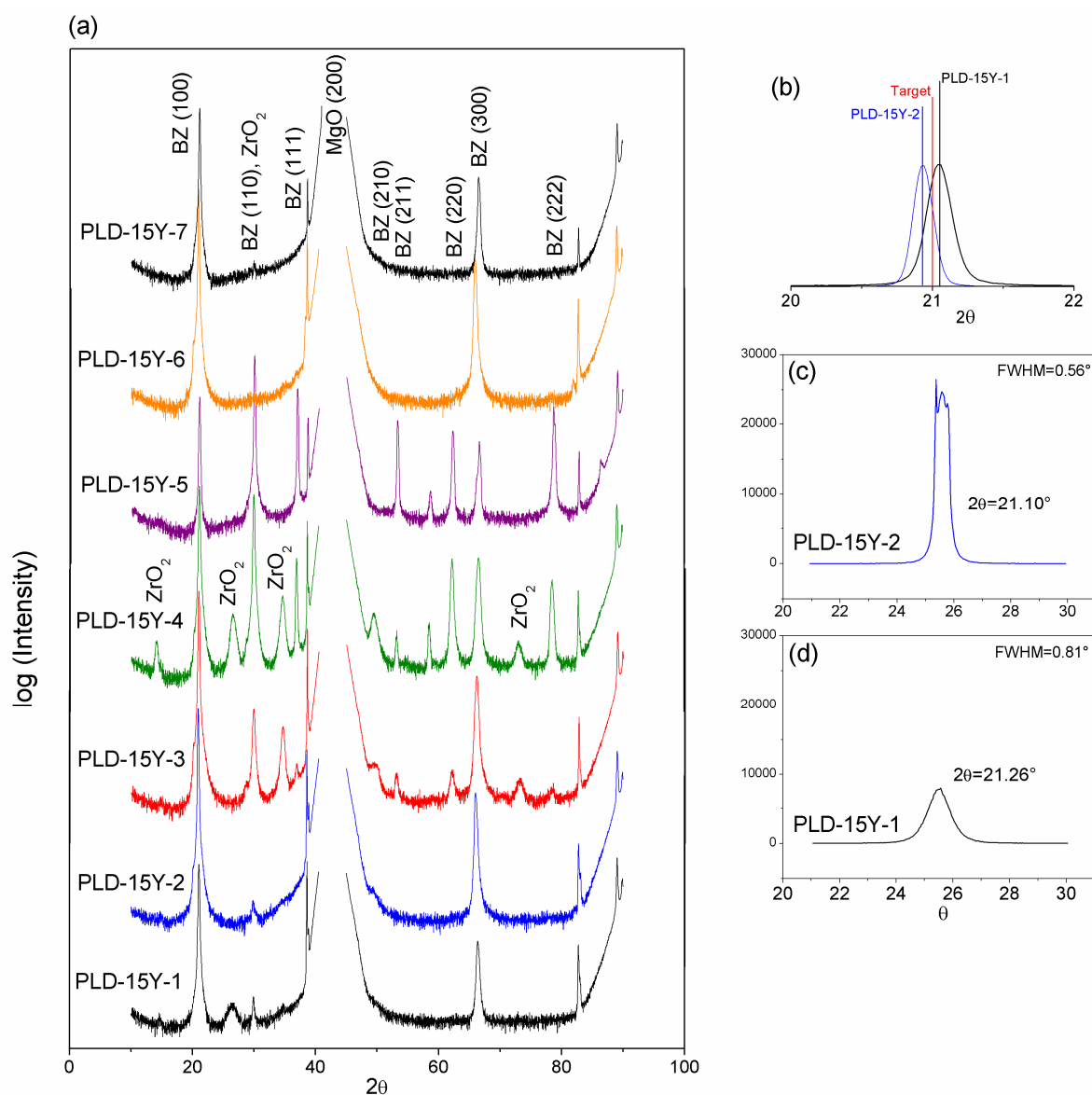


Figure 72 (a) X-ray diffraction pattern of thin films, (b) peak shift of PLD-15Y-1 and PLD-15Y-2, rocking curve of (c) PLD-15Y-2 and (d) PLD-15Y-1

* The BaZrO_3 peaks are assigned according to JCPDS 01-074-1299. The JCPDS 06-0399 does not assign the peak at $2\theta = 67.098$ for (300).

The pole figure and orientation map of PLD-15Y-1 (**Fig. 73**) confirm the single oriented YBZ film. The OIM analysis has the advantage of collecting data from a depth of less than ~ 50 nm, but secondary phase grains smaller than 80 nm cannot be studied by this method.

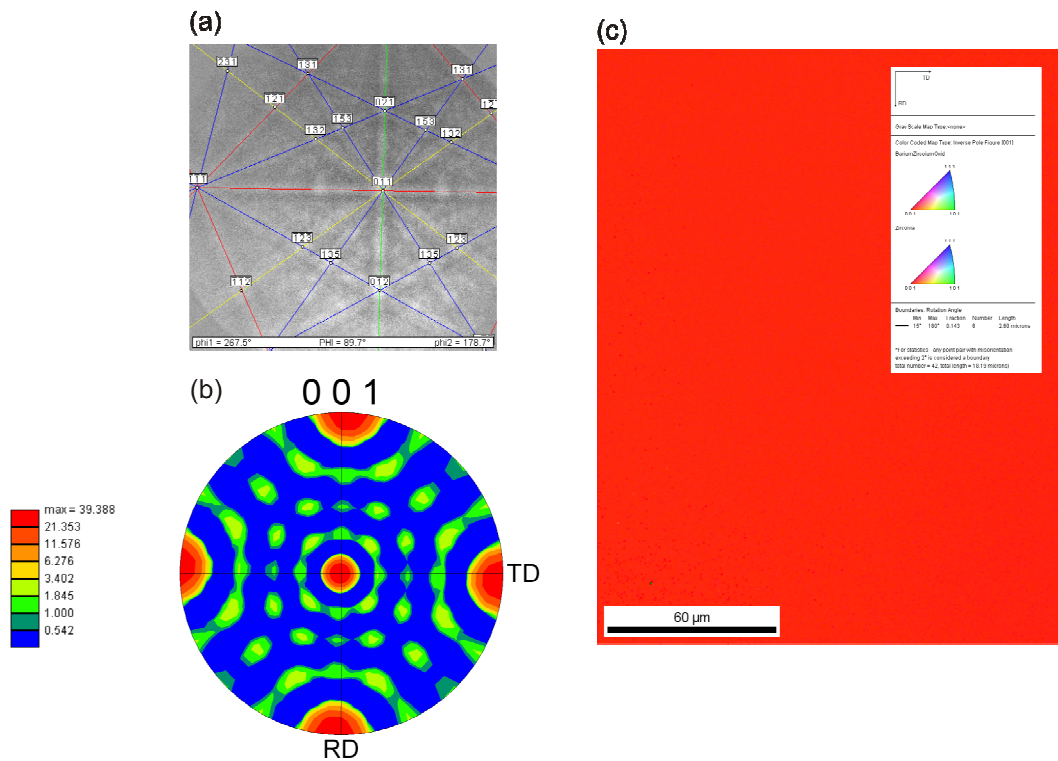


Figure 73 (a) A typical indexing of the EBSD pattern , (b) pole figure (001) and (c) orientation map (inverse pole figure) of PLD-15Y-1

The chemical composition of the films was measured by XPS from an as received sample and after ion beam sputtering (Ar^+ , 1 min.). The results on as received and sputtered samples do not show any significant changes (apart from a slight carbon contamination on the as received samples). The quantification results on sputtered surfaces are summarized in **table 8**. XPS data indicate that all the films are Ba deficient and the dopant concentration is close to the nominal composition. According to the literature^[177, 183], the Ba content of BaZrO_3 films is a function of $p\text{O}_2$, $T_{\text{substrate}}$, deposition time (film thickness) and energy. The XPS data on the films investigated here do not show any simple correlation between Ba concentration and PLD conditions.

Table 8 Chemical composition of thin films by XPS

Thin film	Ba	Zr	Y
PLD-15Y-1 (sputtered)	0.79	0.84	0.16
PLD-15Y-2 (sputtered)	0.66	0.83	0.17
PLD-15Y-3 (sputtered)	0.87	0.83	0.17
PLD-15Y-4 (sputtered)	0.63	0.82	0.18
PLD-15Y-5 (sputtered)	0.63	0.84	0.17
PLD-15Y-6 (sputtered)	0.63	0.84	0.17
PLD-15Y-7 (sputtered)	0.73	0.83	0.17

AC impedance spectroscopy was performed in the in-plane direction using sputtered Pt electrodes. The impedance spectra exhibit one semicircle (**Fig. 74**) assigned as the film resistance in parallel to stray capacitance ($C_{\text{stray}} \sim 1$ pF). The resistivity of these films in wet conditions is remarkably higher than in dry atmosphere, which indicates the existence of proton conduction in the films.

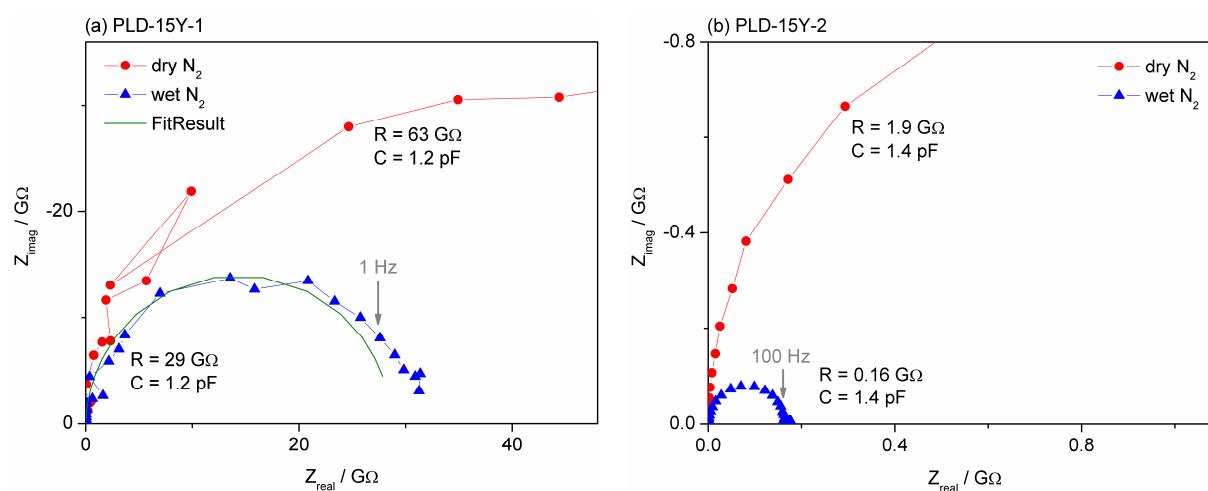


Figure 74 AC impedance spectra of PLD-15YBZ films before and after hydration

The Arrhenius plots of the films in wet conditions are shown in **Fig. 75**. The conductivity of the films is more than 2 orders of magnitude lower than the bulk of a polycrystalline sample. The activation energy of PLD-15Y-2, 3 and 4 (~ 0.5 eV) is close to the bulk value (~ 0.4 eV), but the activation energy of PLD-15Y-1 (~ 0.88 eV), which is epitaxial according to XRD, is high and close to the GB activation energy. The high activation energy in Y-doped SrZrO_3 ^[175] thin films has been attributed to the existence of grain boundaries between columnar crystallites despite the overall epitaxial character of the film. On the other hand, the

conductivity of epitaxial YBZ films (thickness ≤ 110 nm) in ref.^[180] is only ~ 2 times higher than of multi-oriented films (thickness ≥ 450 nm) and activation energies are similar. This can be either due to presence of GBs in the epitaxial layer or high conductivity of GBs in multi-oriented films.

The change in conductance ($1/R$), conductivity (σ) and activation energy (E_a) of the films grown at the same conditions (PLD-15Y-1, 2, 3 and 4) as a function of thickness is shown in **Fig. 76**. The films of 100 and 300 nm are strongly textured and the 300 nm film shows a significantly higher conductivity. This sample exhibits a shift to higher 2θ values in the XRD pattern. The thicker films (600 and 1000 nm) are multi-oriented and their lower conductivity can be explained by presence of some domains in the sample.

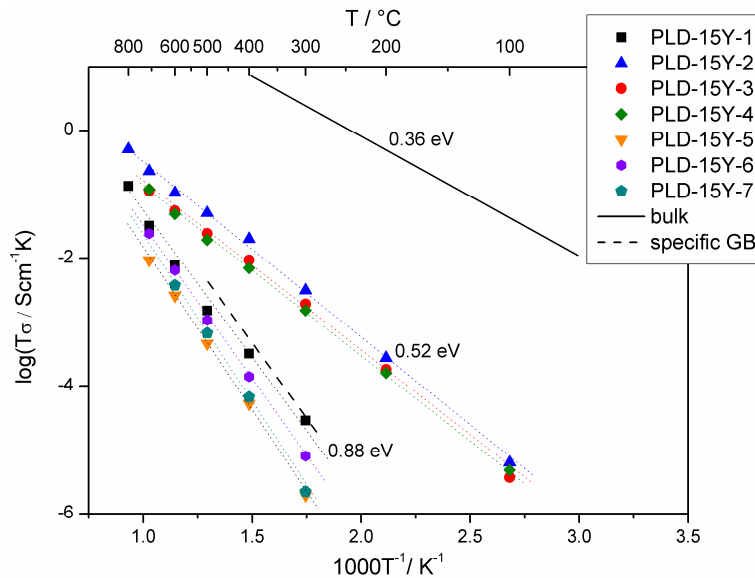


Figure 75 Arrhenius plots of PLD-15YBZ films in wet N_2 ($p_{H_2O} = 20$ mbar) compared to the bulk conductivity of 15 at.% Y-doped BZ

As mentioned, the low conductivity of thin films can be due to presence of blocking GBs which cannot be distinguished by impedance spectroscopy due to the geometry of the films. A rough estimation shows that the capacitance of the epitaxial film with 100 nm thickness ($C_b = \epsilon_0 \epsilon_r A/L = \epsilon_0 \cdot 40 \cdot 10 \text{ mm} \cdot 100 \text{ nm} / 1 \text{ mm} \approx 10^{-16}$ F) is much smaller than the typical stray capacitance ($\sim 10^{-12}$ F), thus the measured capacitance is not the bulk value (**Fig. 77-a**). In a polycrystalline film the GB capacitance is ($C_{GB} = C_b d_g / \delta_{GB} = 10^{-16} \cdot 1000 \text{ nm} / 1 \text{ nm}$) about 10^{-13} F. Therefore, both bulk and GB capacitances are smaller than the stray capacitance ($\sim 10^{-12}$ F) and a separate GB semicircle does not appear in the impedance spectra (**Fig. 77-b**). A similar

estimation shows that in the case of one single GB in the film deposited on bicrystal, the capacitance will be ($C_{GB} = \epsilon_0 \epsilon_r A/L = \epsilon_0 \cdot 40 \cdot 10 \text{mm} \cdot 100 \text{nm}/1 \text{nm}$) $\sim 10^{-10}$ F which is larger than the stray capacitance. Therefore, there is a high chance to measure the resistance and capacitance of well-defined GBs on the bicrystal substrates (**Fig. 77-c**).

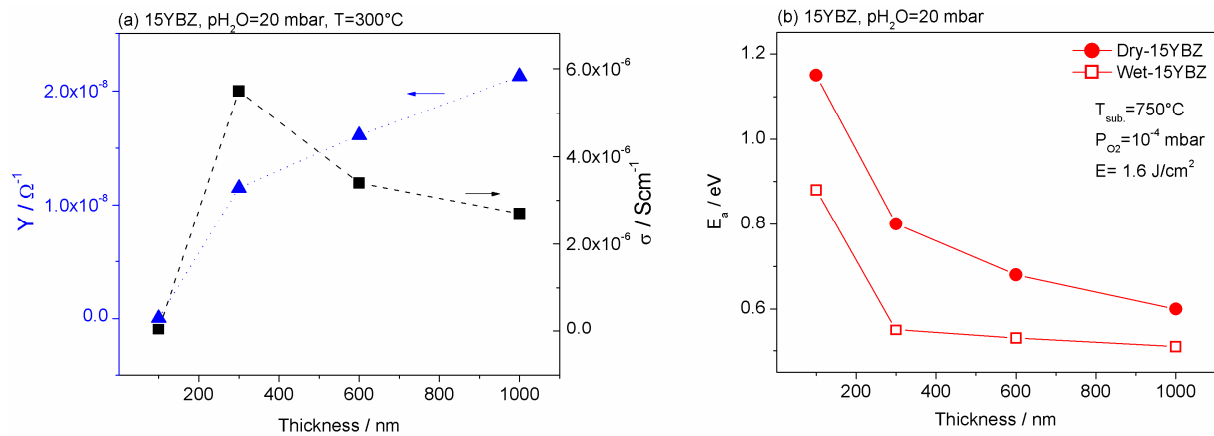


Figure 76 (a) Conductance and, (b) activation energy of thin films (similar deposition conditions) as a function of thickness

The conductivity measurements showed that the single oriented PLD-15Y-1 and PLD-15Y-2 films exhibit different resistivities. TEM investigations were performed to resolve any difference between the films, in particular presence of GBs, different interface features and inhomogeneous composition.

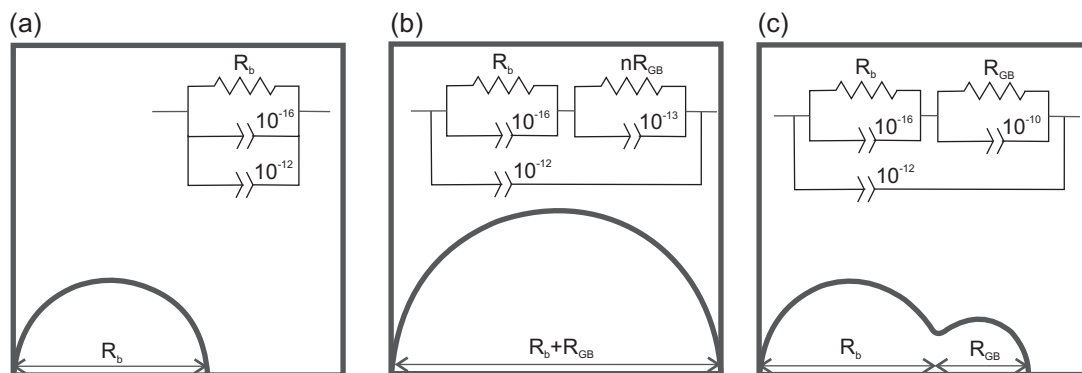


Figure 77 Simulated impedance spectra for (a) an epitaxial layer, (b) a polycrystalline layer (with lateral grain size of 1000 nm) and, (c) a bicrystal layer in a material with highly blocking GBs measured in a cell with stray capacitance of 1pF.

The cross-sectional structures of the PLD-15Y-1 and PLD-15Y-2 films are shown in the bright field TEM images **Fig. 78**. The two films exhibit an epitaxial structure, and no GB, in-plane as well as columnar, is observed in the number of images from different parts along the FIB sample. The thickness of films is slightly smaller than the nominal value and no extra features (amorphous phase, interface roughness) are observed at the interface of film and substrate. The line scan EDXS-TEM (**Fig. 79**) does not show any significant change in the cation concentration across the film thickness for PLD-15Y-1 and PLD-15Y-2. The absolute values obtained by EDXS are not consistent with the XPS results (**Table 8**). Without a standard sample it is difficult to decide about the exact composition of films and the XPS and EDXS data can only be used for a comparison between the films.

A closer look at the interface using high-resolution TEM is given in **Fig. 80**. These images do not show a difference between the two films, and growth of highly oriented YBZ film on the MgO substrate is clear.

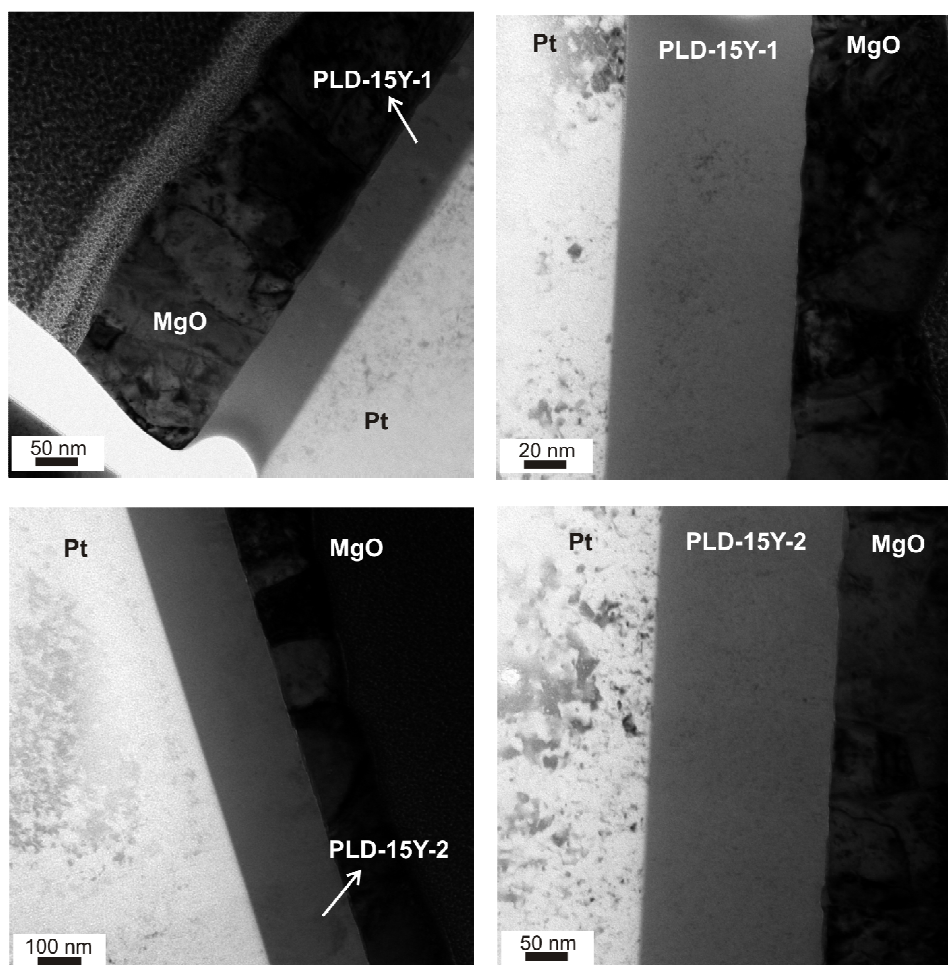


Figure 78 TEM bright-field image from cross-section of PLD-15Y-1 and PLD-15Y-2

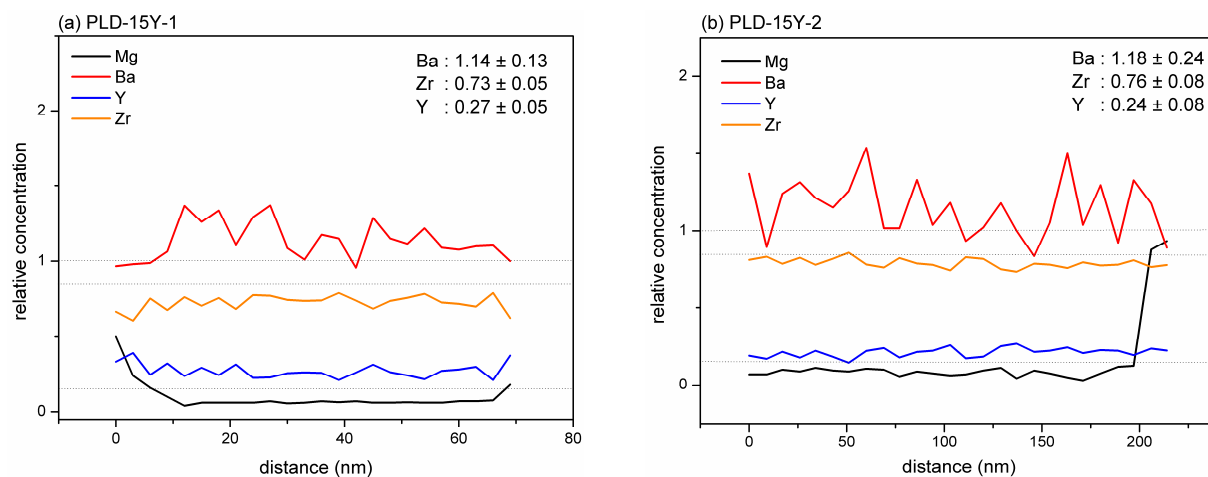


Figure 79 EDXS-TEM line scan on (a) PLD-15Y-1 and (b) PLD-15Y-2

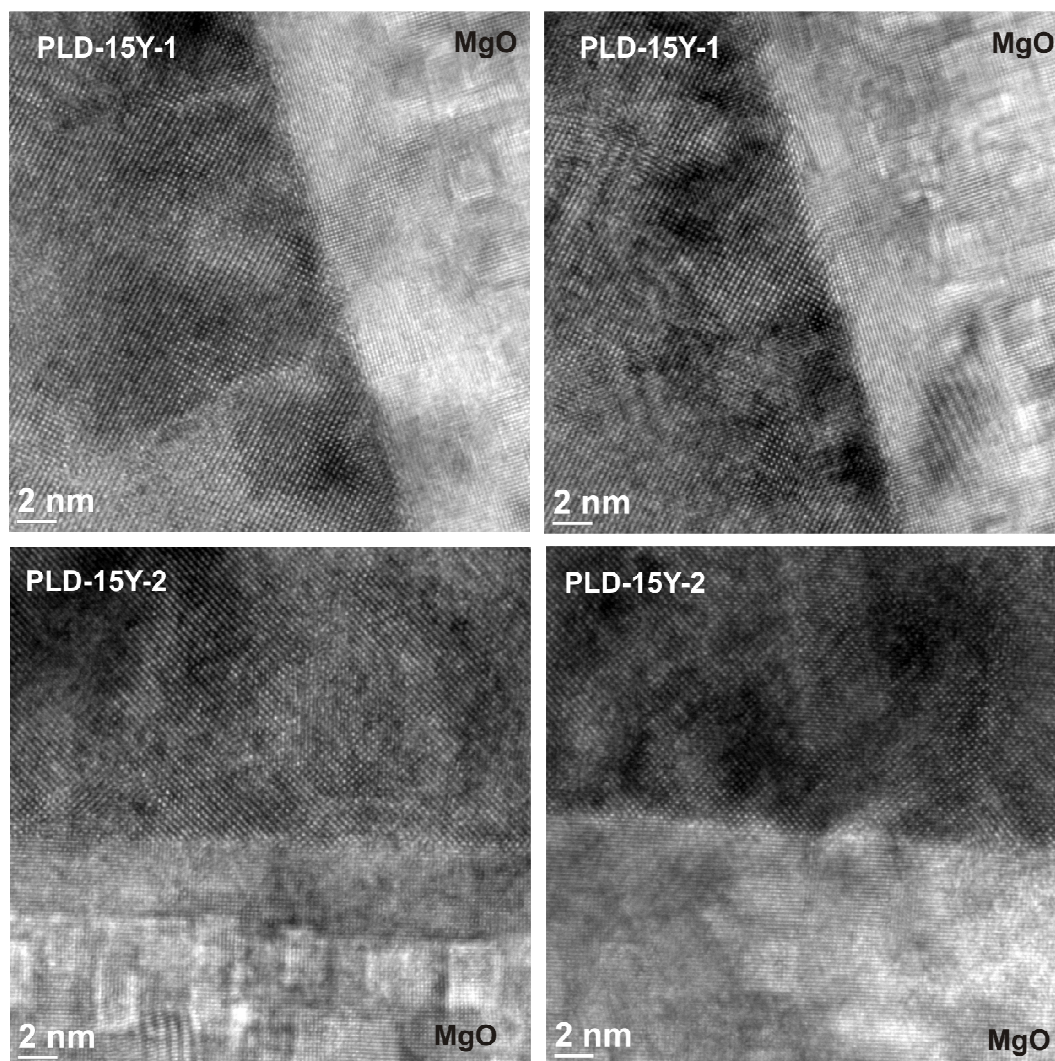


Figure 80 High resolution TEM image from PLD-15Y-1 and PLD-15Y-2

In the end, the growth conditions of PLD-15Y-2 were selected to apply an epitaxial layer on different bicrystal substrates. Preliminary conductivity measurements on the two thin films applied on the selected bicrystal substrates did not show a considerable difference. However, the low angle or non-CSL grain boundaries might show different blocking behavior.

Chapter 4

Conclusions

The present thesis deals with the origin of the high grain boundary resistance of proton conducting oxides, specifically for BaZrO₃. The study of hydration behavior, composition and structure of grain boundaries revealed that weak hydration of GBs and secondary/amorphous phase at the GB plane do not have a notable contribution to the blocking character of GBs in this material. Also, for the majority of GBs in a polycrystalline ceramic, the details of the crystallographic misorientation between the grains do not significantly affect the low GB conductivity.

On the other hand, segregation of negatively charged dopant cations to the GB core and neighboring space charge zones considerably enhances the conductivity of GB. The effect of dopant enrichment on σ_{GB} as well as electrical behavior of GB for different cooling rates (V_{Ba}'' segregation) suggested the existence of a positively charged GB core. The excess charge leads to depletion of positive charge carriers, (protons, holes and oxygen vacancies) in space charge region.

This picture was confirmed by reducing the sample to a regime where electron conduction in the GB region becomes decisive and electron accumulation (may be combined with a decrease of the positive core charge) leads to disappearance of the blocking GB character. Furthermore, the nonlinear electrical properties of GB under DC-bias, in particular the decrease of GB resistance as well as of GB capacitance with applied bias, give direct evidence for the formation of depletion layers near the GB plane. Thus, the GBs in acceptor doped BaZrO₃ exhibit a similar behavior as in acceptor doped SrTiO₃ where the space charge model could be studied in great details using bicrystal samples. For low-angle GBs in SrTiO₃ bicrystals, oxygen vacancies appear as regular structure motifs in the GB core to avoid too close contacts

between certain oxide ions. A similar intrinsic origin for the positive core charge in acceptor doped BaZrO_3 may be relevant here as well.

In summary, the present study on GB of BaZrO_3 clarified the major contribution of charged core and related space charge layers to the blocking character of the GB. This phenomenon, which is closely coupled to the composition of grain and grain boundaries, determines the defect structure and consequently electrical and sintering properties of GB.

Based on these findings, a deliberate substitution of the Ba site with the relatively large Cs^+ cation with expected high segregation tendency was undertaken, and indeed improved GB conductivity.

These strategies show how to modify acceptor-doped BaZrO_3 and also other proton conducting ceramics to render them as suitable solid electrolytes for intermediate temperature fuel cells or related applications.

Abbreviations and Symbols

List of Abbreviations

AC	alternating current
BET	Brunauer-Emmett-Teller method
BZ	BaZrO ₃
CS	conventionally sintered
CSL	coincidence site lattice
C50	cooling rate of 50°C/h
C300	cooling rate of 300°C/h
DC	direct current
EDXS	energy dispersive x-ray spectroscopy
EELS	Electron Energy Loss Spectroscopy
FIB	Focused Ion Beam
GB	Grain Boundary
GBs	Grain Boundaries
ICP-OES	inductively coupled plasma- optical emission spectroscopy
IF	image furnace
IF-YBZ	image furnace Y-doped BaZrO ₃
OIM	Orientation Imaging Microscopy
PLD	pulsed laser deposition
ScBZ	Sc-doped BaZrO ₃
SCCM	Standard Cubic Centimeters per Minute
SEM	scanning electron microscopy

SESAM	Sub Electronvolt Sub Ångstrom Microscope
SOFC	solid oxide fuel cells
SPS	spark plasma sintered
TEM	transmission electron microscopy
TG	thermogravimetry
XPS	X-ray photoelectron spectroscopy
XRD	X-ray diffraction
YBZ	Y-doped BaZrO ₃

List of Symbols

C	capacitance
C_b	bulk capacitance
C_{GB}	grain boundary capacitance
d_g	grain diameter
δ_{GB}	grain boundary thickness
E_a	activation energy
Φ_0	space charge potential barrier
λ	Debye length (eq. (11))
λ^*	thickness of space charge layer (eq. (12))
Q	constant phase element
R	gas constant
R	resistivity
R_b	bulk resistance
R_{GB}	grain boundary resistance
σ	electrical conductivity
σ_b	electrical conductivity of bulk
σ_{GB}	electrical conductivity of grain boundary
$\sigma_{GB,sp}$	specific electrical conductivity of GB
U_{dc}	DC bias

References

- [1] S. C. Singhal, *Solid State Ionics* 2000, 135, 305.
- [2] T. Takahashi, H. Iwahara, *Revue De Chimie Minerale* 1980, 17, 243.
- [3] H. Iwahara, H. Uchida, S. Tanaka, *Solid State Ionics* 1983, 9-10, 1021.
- [4] H. Uchida, N. Maeda, H. Iwahara, *Journal of Applied Electrochemistry* 1982, 12, 645.
- [5] H. Iwahara, H. Uchida, S. Tanaka, *Journal of Applied Electrochemistry* 1986, 16, 663.
- [6] S. M. Haile, K. D. Kreuer, J. Maier, *Acta Crystallographica Section B-Structural Science* 1995, 51, 680.
- [7] H. Iwahara, T. Esaka, H. Uchida, N. Maeda, *Solid State Ionics* 1981, 3-4, 359.
- [8] H. Iwahara, H. Uchida, K. Ono, K. Ogaki, *Journal of the Electrochemical Society* 1988, 135, 529.
- [9] T. Yajima, H. Kazeoka, T. Yogo, H. Iwahara, *Solid State Ionics* 1991, 47, 271.
- [10] H. Iwahara, T. Yajima, T. Hibino, K. Ozaki, H. Suzuki, *Solid State Ionics* 1993, 61, 65.
- [11] T. Hibino, K. Mizutani, T. Yajima, H. Iwahara, *Solid State Ionics* 1992, 57, 303.
- [12] Y. Yamazaki, R. Hernandez-Sanchez, S. M. Haile, *Chemistry of Materials* 2009, 21, 2755.
- [13] H. G. Bohn, T. Schober, *Journal of the American Ceramic Society* 2000, 83, 768.
- [14] T. Fukui, S. Ohara, S. Kawatsu, *Journal of Power Sources* 1998, 71, 164.
- [15] R. L. Cook, J. J. Osborne, J. H. White, R. C. Macduff, A. F. Sammells, *Journal of the Electrochemical Society* 1992, 139, L19.
- [16] Y. Larring, T. Norby, *Solid State Ionics* 1994, 70, 305.
- [17] H. Fujii, Y. Katayama, T. Shimura, H. Iwahara, *Journal of Electroceramics* 1998, 2, 119.
- [18] K. C. Liang, A. S. Nowick, *Solid State Ionics* 1993, 61, 77.
- [19] K. C. Liang, Y. Du, A. S. Nowick, *Solid State Ionics* 1994, 69, 117.
- [20] A. S. Nowick, Y. Du, *Solid State Ionics* 1995, 77, 137.
- [21] H. G. Bohn, T. Schober, T. Mono, W. Schilling, *Solid State Ionics* 1999, 117, 219.
- [22] S. Li, F. Schonberger, P. Slater, *Chemical Communications* 2003, 2694.
- [23] T. Shimura, Y. Tokiwa, H. Iwahara, *Solid State Ionics* 2002, 154, 653.
- [24] I. Animitsa, T. Norby, S. Marion, R. Glockner, A. Neiman, *Solid State Ionics* 2001, 145, 357.
- [25] P. Murugaraj, K. D. Kreuer, T. He, T. Schober, J. Maier, *Solid State Ionics* 1997, 98, 1.
- [26] G. B. Zhang, D. M. Smyth, *Solid State Ionics* 1995, 82, 153.
- [27] T. Schober, *Solid State Ionics* 1998, 109, 1.
- [28] T. Shimura, M. Komori, H. Iwahara, *Solid State Ionics* 1996, 86-8, 685.

-
- [29] T. Shimura, S. Fujimoto, H. Iwahara, *Solid State Ionics* 2001, 143, 117.
- [30] K. Amezawa, N. Takahashi, N. Kitamura, Y. Tomii, N. Yamamoto, *Solid State Ionics* 2004, 175, 575.
- [31] T. Norby, N. Christiansen, *Solid State Ionics* 1995, 77, 240.
- [32] K. Amezawa, Y. Tomii, N. Yamamoto, *Solid State Ionics* 2003, 162, 175.
- [33] K. Amezawa, Y. Kitajima, Y. Tomii, N. Yamamoto, M. Wideroe, T. Norby, *Solid State Ionics* 2005, 176, 2867.
- [34] K. Amezawa, Y. Kitajima, Y. Tomii, N. Yamamoto, *Electrochemical and Solid State Letters* 2004, 7, A511.
- [35] M. Nagao, T. Kamiya, P. Heo, A. Tomita, T. Hibino, M. Sano, *Journal of the Electrochemical Society* 2006, 153, A1604.
- [36] R. Haugrud, T. Norby, *Nature Materials* 2006, 5, 193.
- [37] R. Haugrud, T. Norby, *Journal of the American Ceramic Society* 2007, 90, 1116.
- [38] T. Norby, O. Dyrлие, P. Kofstad, *Journal of the American Ceramic Society* 1992, 75, 1176.
- [39] T. Norby, O. Dyrлие, P. Kofstad, *Solid State Ionics* 1992, 53, 446.
- [40] L. Leon-Reina, J. M. Porrás-Vázquez, E. R. Losilla, M. A. G. Aranda, *Journal of Solid State Chemistry* 2007, 180, 1250.
- [41] K. Amezawa, J. Yamada, N. Kitamura, Y. Tomii, T. Handa, N. Yamamoto, *Solid State Ionics* 2005, 176, 341.
- [42] T. Shimura, K. Suzuki, H. Iwahara, *Solid State Ionics* 1997, 104, 79.
- [43] F. A. Kröger, *Chemistry of imperfect crystals*, North-Holland, Amsterdam, 1964.
- [44] K. D. Kreuer, S. Adams, W. Munch, A. Fuchs, U. Klock, J. Maier, *Solid State Ionics* 2001, 145, 295.
- [45] N. Bonanos, F. W. Poulsen, *Journal of Materials Chemistry* 1999, 9, 431.
- [46] F. W. Poulsen, *Journal of Solid State Chemistry* 1999, 143, 115.
- [47] S. J. Song, E. D. Wachsman, S. E. Dorris, U. Balachandran, *Solid State Ionics* 2002, 149, 1.
- [48] N. V. Sharova, V. P. Gorelov, *Russian Journal of Electrochemistry* 2005, 41, 1130.
- [49] J. Wu, R. A. Davies, M. S. Islam, S. M. Haile, *Chemistry of Materials* 2005, 17, 846.
- [50] D. Shima, S. M. Haile, *Solid State Ionics* 1997, 97, 443.
- [51] S. M. Haile, G. Staneff, K. H. Ryu, *Journal of Materials Science* 2001, 36, 1149.
- [52] J. Maier, *Physical Chemistry of Ionic Materials: Ions and Electrons in Solids*, Wiley, West Sussex, England, 2004.
- [53] F. Shimojo, K. Hoshino, H. Okazaki, *Journal of Physics-Condensed Matter* 1998, 10, 285.
- [54] W. Munch, K. D. Kreuer, G. Seifertli, J. Majer, *Solid State Ionics* 1999, 125, 39.
- [55] K. D. Kreuer, *Annual Review of Materials Research* 2003, 33, 333.
- [56] M. S. Islam, P. R. Slater, J. R. Tolchard, T. Dinges, *Dalton Transactions*, 2004, 3061.
- [57] S. M. Haile, D. L. West, J. Campbell, *Journal of Materials Research* 1998, 13, 1576.
- [58] A. K. Azad, J. T. S. Irvine, *Solid State Ionics* 2007, 178, 635.
- [59] F. Iguchi, T. Yamada, N. Sata, T. Tsurui, H. Yugami, *Solid State Ionics* 2006, 177, 2381.
- [60] F. Iguchi, N. Sata, T. Tsurui, H. Yugami, *Solid State Ionics* 2007, 178, 691.
- [61] P. Babilo, S. M. Haile, *Journal of the American Ceramic Society* 2005, 88, 2362.
- [62] S. B. C. Duval, P. Holtappels, U. F. Vogt, E. Pomjakushina, K. Conder, U. Stimming, T. Graule, *Solid State Ionics* 2007, 178, 1437.

-
- [63] R. B. Cervera, Y. Oyama, S. Miyoshi, K. Kobayashi, T. Yagi, S. Yamaguchi, *Solid State Ionics* 2008, 179, 236.
- [64] B. C. H. Steele, *Journal of Materials Science* 2001, 36, 1053.
- [65] S. Duval, PhD thesis, Technische Universität München, 2008.
- [66] C. Kjolseth, H. Fjeld, O. Prytz, P. I. Dahl, C. Estournes, R. Haugrud, T. Norby, *Solid State Ionics* 2010, 181, 268.
- [67] P. Babilo, T. Uda, S. M. Haile, *Journal of Materials Research* 2007, 22, 1322.
- [68] S. B. C. Duval, P. Holtappels, U. Stimming, T. Graule, *Solid State Ionics* 2008, 179, 1112.
- [69] S. B. C. Duval, P. Holtappels, U. F. Vogt, U. Stimming, T. Graule, *Fuel Cells* 2009, 9, 613.
- [70] S. W. Tao, J. T. S. Irvine, *Journal of Solid State Chemistry* 2007, 180, 3493.
- [71] J. H. Tong, D. Clark, L. Bernau, M. Sanders, R. O'Hayre, *Journal of Materials Chemistry* 2010, 20, 6333.
- [72] J. S. Park, J. H. Lee, H. W. Lee, B. K. Kim, *Solid State Ionics*, 181, 163.
- [73] N. Ito, H. Matsumoto, Y. Kawasaki, S. Okada, T. Ishihara, *Solid State Ionics* 2008, 179, 324.
- [74] S. Imashuku, T. Uda, Y. Nose, K. Kishida, S. Harada, H. Inui, Y. Awakura, *Journal of the Electrochemical Society* 2008, 155, B581.
- [75] A. C. T. van Duin, B. V. Merinov, S. S. Han, C. O. Dorso, W. A. Goddard, *Journal of Physical Chemistry A* 2008, 112, 11414.
- [76] S. P. S. Badwal, *Solid State Ionics* 1995, 76, 67.
- [77] D. Y. Wang, A. S. Nowick, *Journal of the Electrochemical Society* 1980, 127, 113.
- [78] X. Guo, R. Waser, *Progress in Materials Science* 2006, 51, 151.
- [79] Z. Zhang, W. Sigle, R. A. De Souza, W. Kurtz, J. Maier, M. Ruhle, *Acta Materialia* 2005, vol.53, no.19, 5007.
- [80] W. D. Kingery, *Journal of the American Ceramic Society* 1974, 57, 1.
- [81] Y. M. Chiang, T. Takagi, *Journal of the American Ceramic Society* 1990, 73, 3278.
- [82] X. Guo, *Solid State Ionics* 1995, 81, 235.
- [83] A. Tschope, *Solid State Ionics* 2001, 139, 267.
- [84] J. A. S. Ikeda, Y. M. Chiang, *Journal of the American Ceramic Society* 1993, 76, 2437.
- [85] M. Vollman, R. Waser, *Journal of the American Ceramic Society* 1994, 77, 235.
- [86] X. Guo, W. Sigle, J. Maier, *Journal of the American Ceramic Society* 2003, 86, 77.
- [87] R. A. De Souza, *Physical Chemistry Chemical Physics* 2009, 11, 9939.
- [88] J. Frenkel, *Kinetic Theory of Liquids*, Oxford University Press, 1946.
- [89] J. Maier, *Ber. Bunsenges. Phys. Chem.* 88, 1057-1062 1984.
- [90] N. D. Browning, J. P. Buban, H. O. Moltaji, S. J. Pennycook, G. Duscher, K. D. Johnson, R. P. Rodrigues, V. P. Dravid, *Applied Physics Letters* 1999, 74, 2638.
- [91] C. L. Jia, K. Urban, *Science* 2004, 303, 2001.
- [92] R. A. De Souza, J. Fleig, J. Maier, O. Kienzle, Z. L. Zhang, W. Sigle, M. Ruhle, *Journal of the American Ceramic Society* 2003, 86, 922.
- [93] M. Vollmann, R. Waser, *Journal of Electroceramics* 1997, 1, 51.
- [94] X. Guo, S. B. Mi, R. Waser, *Electrochemical and Solid State Letters* 2005, 8, J1.
- [95] R. Meyer, X. Guo, R. Waser, *Electrochemical and Solid State Letters* 2005, 8, E67.
- [96] X. Guo, R. Waser, *Solid State Ionics* 2004, 173, 63.
- [97] S. Rodewald, J. Fleig, J. Maier, *Journal of the American Ceramic Society* 2001, 84, 521.
- [98] T. Holbling, R. Waser, *Journal of Applied Physics* 2002, 91, 3037.

-
- [99] X. Guo, Y. Ding, *Journal of the Electrochemical Society* 2004, 151, J1.
- [100] J. S. Lee, U. Anselmi-Tamburini, Z. A. Munir, S. Kim, *Electrochemical and Solid State Letters* 2006, 9, J34.
- [101] V. Ravikumar, R. P. Rodrigues, V. P. Dravid, *Journal of the American Ceramic Society* 1997, 80, 1131.
- [102] S. von Alfthan, N. A. Benedek, L. Chen, A. Chua, D. Cockayne, K. J. Dudeck, C. Elsasser, M. W. Finnis, C. T. Koch, B. Rahmati, M. Ruhle, S. J. Shih, A. P. Sutton, *Annual Review of Materials Research* 2010, 40, 557.
- [103] M. F. Yan, R. M. Cannon, H. K. Bowen, *Journal of Applied Physics* 1983, 54, 764.
- [104] W. D. Kingery, *Journal of the American Ceramic Society* 1974, 57, 74.
- [105] P. Wynblatt, G. S. Rohrer, F. Papillon, *Journal of the European Ceramic Society* 2003, 23, 2841.
- [106] S. B. Desu, D. A. Payne, *Journal of the American Ceramic Society* 1990, 73, 3391.
- [107] S. L. Hwang, I. W. Chen, *Journal of the American Ceramic Society* 1990, 73, 3269.
- [108] Q. L. Wang, G. Lian, E. C. Dickey, *Acta Materialia* 2004, 52, 809.
- [109] F. Boulc'h, E. Djurado, L. Dessemond, *Journal of the Electrochemical Society* 2004, 151, A1210.
- [110] G. Horvath, J. Gerblinger, H. Meixner, J. Giber, *Sensors and Actuators B-Chemical* 1996, 32, 93.
- [111] A. Tschöpe, E. Sommer, R. Birringer, *Solid State Ionics* 2001, 139, 255.
- [112] J. D. Powers, A. M. Glaeser, *Interface Science* 1998, 6, 23.
- [113] J. H. Han, D. Y. Kim, *Journal of the American Ceramic Society* 2001, 84, 539.
- [114] P. L. Chen, I. W. Chen, *Journal of the American Ceramic Society* 1996, 79, 1793.
- [115] P. L. Chen, I. W. Chen, *Journal of the American Ceramic Society* 1996, 79, 1801.
- [116] J. W. Cahn, *Acta Metallurgica* 1962, 10, 789.
- [117] K. Lucke, H. P. Stuwe, *Acta Metallurgica* 1971, 19, 1087.
- [118] M. P. Seah, *Journal of Physics F (Metal Physics)* 1980, vol.10, no.6, 10.1088/0305.
- [119] S. B. Desu, D. A. Payne, *Journal of the American Ceramic Society* 1990, 73, 3407.
- [120] Y. Yamazaki, R. Hernandez-Sanchez, S. M. Haile, *Journal of Materials Chemistry* 2010, 20, 8158.
- [121] K. D. Kreuer, *Solid State Ionics* 1999, 125, 285.
- [122] R. D. Leapman, C. E. Fiori, C. R. Swyt, *Journal of Microscopy-Oxford* 1984, 133, 239.
- [123] G. Cliff, G. W. Lorimer, *Journal of Microscopy-Oxford* 1975, 103, 203.
- [124] J. E. Bauerle, *Journal of Physics and Chemistry of Solids* 1969, 30, 2657.
- [125] J. Fleig, *Solid State Ionics* 2002, 150, PII S0167.
- [126] T. Vandijk, A. J. Burggraaf, *Physica Status Solidi A-Applied Research* 1981, 63, 229.
- [127] J. Fleig, J. Maier, *Journal of the European Ceramic Society* 1999, 19, 693.
- [128] T. Schober, H. G. Bohn, *Solid State Ionics* 2000, 127, 351.
- [129] E. Fabbri, D. Pergolesi, S. Licocchia, E. Traversa, *Solid State Ionics* 2010, 181, 1043.
- [130] R. D. Shannon, *Acta Crystallographica Section A* 1976, 32, 751.
- [131] N. Kurita, N. Fukatsu, K. Ito, T. Ohashi, *Journal of the Electrochemical Society* 1995, 142, 1552.
- [132] K. Nomura, H. Kageyama, *Solid State Ionics* 2007, 178, 661.
- [133] K. Gomann, G. Bochardt, M. Schulz, A. Gomann, W. Maus-Friedrichs, B. Lesage, O. Kaitasov, S. Hoffman-Eifert, T. Schneller, *Physical Chemistry Chemical Physics* 2005, 7, 2053.
- [134] S. Koerfer, R. A. De Souza, H. I. Yoo, M. Martin, *Solid State Sciences* 2008, 10, 725.
- [135] W. D. Kingery, *Pure and Applied Chemistry* 1984, 56, 1703.

-
- [136] J. Jamnik, J. Maier, S. Pejovnik, *Solid State Ionics* 1995, 75, 51.
- [137] K. L. Kliewer, *Journal of Physics and Chemistry of Solids* 1966, 27, 705.
- [138] R. B. Poeppel, J. M. Blakely, *Surface Science* 1969, 15, 507.
- [139] J. S. Lee, D. Y. Kim, *Journal of Materials Research* 2001, 16, 2739.
- [140] F. Iguchi, N. Sata, H. Yugami, *Journal of Materials Chemistry* 2010, 20, 6265.
- [141] T. Oyama, M. Yoshiya, H. Matsubara, K. Matsunaga, *Physical Review B* 2005, 71.
- [142] S. Kim, J. Maier, *Journal of the Electrochemical Society* 2002, 149, J73.
- [143] R. A. De Souza, J. Maier, *Physical Chemistry Chemical Physics* 2003, 5, 740.
- [144] R. A. De Souza, M. S. Islam, E. Ivers-Tiffée, *Journal of Materials Chemistry* 1999, 9, 1621.
- [145] D. G. Brandon, *Acta Metallurgica* 1966, 14, 1479.
- [146] F. Ernst, M. L. Mulvihill, O. Kienzle, M. Ruhle, *Journal of the American Ceramic Society* 2001, 84, 1885.
- [147] F. Iguchi, T. Tsurui, N. Sata, Y. Nagao, H. Yugami, *Solid State Ionics* 2009, 180, 563.
- [148] E. Fabbri, D. Pergolesi, S. Licocchia, E. Traversa, *Solid State Ionics*, 181, 1043.
- [149] R. A. Davies, M. S. Islam, J. D. Gale, *Solid State Ionics* 1999, 126, 323.
- [150] B. Bialobok, J. Trawczynski, T. Rządki, W. Mista, M. Zawadzki, *Catalysis Today* 2007, 119, 278.
- [151] K. H. Haas, U. Schindewolf, *Journal of Solid State Chemistry* 1984, 54, 342.
- [152] M. Spaeth, K. D. Kreuer, T. Dippel, J. Maier, *Solid State Ionics* 1997, 97, 291.
- [153] H. D. Lutz, J. Henning, H. Jacobs, B. Mach, *Journal of Molecular Structure* 1986, 145, 277.
- [154] M. H. Brooker, J. F. Wang, *Spectrochimica Acta Part A-Molecular and Biomolecular Spectroscopy* 1992, 48, 999.
- [155] A. Rizea, J. M. Raulot, C. Petot, G. Petot-Ervas, G. Baldinozzi, *Diffusion and Defect Data Part B (Solid State Phenomena)* 2005, vol.106, 83.
- [156] C. A. Leach, P. Tanev, B. C. H. Steele, *Journal of Materials Science Letters* 1986, 5, 893.
- [157] R. Wernicke, *Physica Status Solidi A-Applied Research* 1978, 47, 139.
- [158] I. Denk, J. Claus, J. Maier, *Journal of the Electrochemical Society* 1997, 144, 3526.
- [159] J. Fleig, S. Rodewald, J. Maier, *Journal of Applied Physics* 2000, 87, 2372.
- [160] J. Fleig, J. Maier, *Solid State Ionics* 1996, 85, 9.
- [161] G. E. Pike, C. H. Seager, *Journal of Applied Physics* 1979, 50, 3414.
- [162] W. G. Morris, *Journal of Vacuum Science & Technology* 1976, 13, 926.
- [163] P. R. Emtage, *Journal of Applied Physics* 1977, 48, 4372.
- [164] W. E. Taylor, N. H. Odell, H. Y. Fan, *Physical Review* 1952, 88, 867.
- [165] R. Herrmann, W. Kraak, G. Nachtwei, *Physica Status Solidi B-Basic Research* 1985, 128, 337.
- [166] G. Blatter, F. Greuter, *Physical Review B* 1986, 34, 8555.
- [167] S. Bengtsson, O. Engstrom, *Journal of Applied Physics* 1989, 66, 1231.
- [168] K. Mukae, K. Tsuda, I. Nagasawa, *Journal of Applied Physics* 1979, 50, 4475.
- [169] K. Wang, W. Z. Shen, H. F. Yang, *Applied Surface Science* 2003, 217, 100.
- [170] R. H. Fowler, L. Nordheim, *Proceedings of the Royal Society of London Series A-Containing Papers of a Mathematical and Physical Character* 1928, 119, 173.
- [171] R. Shao, J. Vavro, D. A. Bonnell, *Applied Physics Letters* 2004, 85, 561.
- [172] L. Sheng-Tao, Y. Yan, Z. Le, C. Peng-Fei, L. Jian-Ying, *Chinese Physics Letters*, 2009, 26, 077201.
- [173] I. Riess, J. Maier, *Physical Review Letters* 2008, 100.

-
- [174] X. X. Chen, L. Rieth, M. S. Miller, F. Solzbacher, *Sensors and Actuators B-Chemical* 2009, 142, 166.
- [175] N. Kuwata, N. Sata, S. Saito, T. Tsurui, H. Yugami, *Solid State Ionics* 2006, 177, 2347.
- [176] X. X. Chen, L. Rieth, M. S. Miller, F. Solzbacher, *Sensors and Actuators B-Chemical* 2009, 137, 578.
- [177] X. X. Chen, L. Rieth, M. S. Miller, F. Solzbacher, *Sensors and Actuators B-Chemical* 2010, 148, 173.
- [178] E. Fabbri, D. Pergolesi, A. D'Epifanio, E. Di Bartolomeo, G. Balestrino, S. Licocchia, E. Traversa, *Energy and Environmental Science* 2008, 1, 355.
- [179] W. P. Sun, L. T. Yan, Z. Shi, Z. W. Zhu, W. Liu, *Journal of Power Sources* 2010, 195, 4727.
- [180] J. H. Shim, T. M. Gur, F. B. Prinz, *Applied Physics Letters* 2008, 92, 253115.
- [181] D. Pergolesi, E. Fabbri, A. D'Epifanio, E. Di Bartolomeo, A. Tebano, S. Sanna, S. Licocchia, G. Balestrino, E. Traversa, *Nature Materials* 2010, 9, 846.
- [182] T. Schneller, T. Schober, *Solid State Ionics* 2003, 164, 131.
- [183] J. H. Shim, J. S. Park, J. An, T. M. Gur, S. Kang, F. B. Prinz, *Chemistry of Materials* 2009, 21, 3290.

Acknowledgements

I would like to express my deep and sincere gratitude to Prof. Dr. Joachim Maier. It has been an honor for me to be his student. His depth of knowledge, support and constructive comments have left a great memory in my mind throughout my PhD work.

I am grateful to Prof. Dr. Joachim Bill and Prof. Dr. Ir. Eric Jan Mittemeijer for reviewing my PhD thesis, making constructive comments and accepting to be in the examination committee. Special thanks to Prof. Dr. Hanns-Ulrich Habermeier, my external PhD advisor, for his helpful suggestions.

In particular, I would like to thank Dr. Rotraut Merkle. Her broad knowledge as well as her logical way of thinking have been a great value for me. Besides being a perfect advisor, she is a great teacher and a respectful friend.

My warm and sincere thanks to Dr. Giuliano Gregori for his enthusiasm in sharing new ideas, and for all his guidance, help and encouragement.

Warm thanks to Prof. Dr. Eugene Kotomin for his valuable advice and for sharing his office and being patient with me. My special thanks to Sofia Weiglein for her magnificent administrative support. I would like to thank Dr. Klaus-Dieter Kreuer for letting me use his unique home-made facilities.

I would like to thank Prof. Dr. Peter van Aken, head of Stuttgart Center for Electron Microscopy (StEM), for his supports on TEM investigations. I am grateful to Dr. Behnaz Rahmati for her patience and intensive TEM measurements. My sincere thanks to Dr. Wilfried Sigle for his useful help and comments. I warmly thank Ute Salzberger for excellent TEM specimen preparation, Kersten Hahn and Peter Kopold for TEM measurements and Dr. Christoph Koch for useful discussions.

I thank Annette Fuchs, Udo Klock, Ewald Schmitt and Peter Senk for technical support in the lab, Gabi Götz for XRD, Uwe Traub in solving the computer related problems, always quick and in the best way. I would like to thank Georg Cristiani, Benjamin Stuhlhofer and Yvonne Link in Technology Service Group for film deposition and lithography.

Many thanks to Dr. Chengtian Lin in Crystal Growth Group for preparing large grained samples, Viola Duppel and Bernhard Fenk for SEM measurements, Dr. Mitsuhara Konuma (Interface Analysis Service Group) for XPS, Dr. Udo Welzel and Gerd Maier (X-ray Diffraction Laboratory) for XRD on thin films, Dr. Ewald Bischoff for OIM, Albert Meyer for ICP-OES, and Armin Schultz for Raman spectroscopy.

My special thanks to Helmut Kammerlander (Glass Workshop Service Group) for fantastic work and Barbara Baum (Sample Preparation Service Group) for cutting and polishing an enormous amount of samples.

I would like to thank Dr. Hans-Georg Libuda, coordinator of International Max Planck Research School for Advanced Materials (IMPR-AM), for his supports and help from the very first days of my PhD.

I would like to extend my thanks to my colleagues Piero Lupetin, Dr. Dominik Samuelis, Marcus Göbel and Kiran Adepalli for their help and useful discussions.

Lastly, I would like to thank my parents (Javad and Pari) and my brother (Peyman) for all their love and encouragement. And most of all for my loving, supportive, encouraging, and patient spouse (Amir) whose faithful support during my Ph.D. is so appreciated. Thank you.

Curriculum Vitae

Name Mona Shirpour
Date of Birth 22.03.1980
Place of Birth Tehran / Iran

Since October 2007

PhD

Max Planck Institute for Solid State Research in the Department of Prof. Dr. J. Maier and University of Stuttgart, Germany

Title of thesis: Grain boundary characterization of electroceramics: Acceptor-doped BaZrO_3 , an intermediate temperature proton conductor

Sept. 2002 – May 2004

M.Sc. in Materials Science and Engineering / Ceramics

Sharif University of Technology, Tehran, Iran

Title of thesis: Synthesis and study of a new class of red pigments based on perovskite YAlO_3 structure

Sept. 1998 – Sept. 2002

B.Sc. in Materials Science and Engineering / Ceramics

Iran University of Science & Technology, Tehran, Iran

Title of thesis: Increasing translucency of porcelain bodies in ternary system of Silica, Leucite and Mullite.

Jul. 1998

Diploma of High School in Mathematical and Physical Sciences

Fayazbakhsh High School, Tehran, Iran